AFRL-AFOSR-VA-TR-2023-0369

Surface Roughness Effects in Reflection and Emission of Infrared Radiation for Aerospace Materials in Extreme Environments

Sendur, Kursat
SABANCI UNIVERSITESI
NO:27
ORTA MAHALLE
ISTANBUL (ANATOLIA), , 34956
TUR

06/15/2023
Final Technical Report

Air Force Research Laboratory
Air Force Office of Scientific Research
Arlington, Virginia 22203
Air Force Materiel Command

REPORT DOCUMENTATION PAGE

PLEASE DO NOT RETURN YOUR FORM TO THE ABOVE ORGANIZATION.

1. REPORT DATE	2. REPORT TYPE	3. DATES COVERED	
20230615	Final	START DATE 20180425	END DATE 20230424

4. TITLE AND SUBTITLE
Surface Roughness Effects in Reflection and Emission of Infrared Radiation for Aerospace Materials in Extreme Environments

5a. CONTRACT NUMBER	5b. GRANT NUMBER	5c. PROGRAM ELEMENT NUMBER
	FA9550-18-1-0240	61102F

5d. PROJECT NUMBER	5e. TASK NUMBER	5f. WORK UNIT NUMBER

6. AUTHOR(S)
Kursat Sendur

7. PERFORMING ORGANIZATION NAME(S) AND ADDRESS(ES)
SABANCI UNIVERSITESI
NO:27
ORTA MAHALLE
ISTANBUL (ANATOLIA) 34956
TUR

8. PERFORMING ORGANIZATION REPORT NUMBER

9. SPONSORING/MONITORING AGENCY NAME(S) AND ADDRESS(ES)	10. SPONSOR/MONITOR'S ACRONYM(S)	11. SPONSOR/MONITOR'S REPORT NUMBER(S)
Air Force Office of Scientific Research 875 N. Randolph St. Room 3112 Arlington, VA 22203	AFRL/AFOSR RTB1	AFRL-AFOSR-VA-TR-2023-0369

12. DISTRIBUTION/AVAILABILITY STATEMENT
A Distribution Unlimited: PB Public Release

13. SUPPLEMENTARY NOTES

14. ABSTRACT
The principal motivation of this proposal is to provide a better understanding of the interaction of infrared radiation with aerospace materials in extreme environments. In this context, the surface roughness of the materials surface has an important impact on the reflection and absorption of incident radiation from material surfaces. Here, we developed a computational model for surface roughness effects to understand the interaction of infrared radiation with rough surfaces of materials, including polar dielectric and refractory metals. A detailed theoretical formulation and a numerical implementation was achieved based on the small perturbation method/small slope approximation (SPM/SSA). The code is capable of various statistical descriptions for rough surfaces, including Gaussian power spectral density. Using the computational code, we investigated the effects of various rough surface parameters, such as correlation length and surface roughness height, on the reflection and absorption spectrum of different materials, including polar dielectric and refractory metals.

15. SUBJECT TERMS

16. SECURITY CLASSIFICATION OF:			17. LIMITATION OF ABSTRACT	18. NUMBER OF PAGES
a. REPORT U	b. ABSTRACT U	c. THIS PAGE U	UU	68

19a. NAME OF RESPONSIBLE PERSON	19b. PHONE NUMBER *(Include area code)*
ATTILA SZEP	314 235 6044

Standard Form 298 (Rev.5/2020)
Prescribed by ANSI Std. Z39.18

AFOSR Project Final Report

Agency: Department of Defense – Air Force Office of Scientific Research

Program Officer: Dr. Ali Sayir

Co-Program Officer: Dr. Attila Szep

Department: Physical Sciences (RTB1)

RTB1-1 – Aerospace Materials for Extreme Environments

IOE – European Office of Aerospace Research and Development (EOARD), London, United Kingdom

Award No: FA9550-18-1-0240

Title: Surface Roughness Effects in Reflection and Emission of Infrared Radiation for Aerospace Materials in Extreme Environments

Reporting Period: Final Report

Principle Investigator: Dr. Kursat Sendur, Professor

Institution: Faculty of Engineering and Natural Sciences,
Sabanci University, Istanbul

e-mail: sendur@sabanciuniv.edu
phone: +90-216-4839527

TABLE OF CONTENTS

List of Figures

Figure 14: 0th order weighting function magnitude with respect to dielectric constant for materials with n_r=3. The legend in the figure shows the corresponding k value for each curve. Inset plot corresponds to the boxed region.

Figure 15: Illustration of C_0 functions for Gaussian surfaces overlapped with the weighting function and corresponding surface profile. Top panels a(1),a(2) show two example surface height profiles. Panel (b) shows weighting function with four C_0 functions. Pan

Figure 16: Random roughness effects on Tungsten surface. Top panel: weighting function for wavelengths λ=500nm,1000nm,1500nm,2000nm. Middle panel: optical dielectric constants for W at the visible and near-infrared range. Bottom panel: Reflection spectrum change

Figure 17: Random roughness effects on SiC surface. Top panel: weighting function for wavelengths λ=410nm,1500nm,11700nm,24900nm. Middle panel: optical dielectric constants for SiC at the visible and near-infrared range. Bottom panel: Reflection spectrum change

Figure 18: a) An example random texture generated by setting l =0.1 μm, hrms =0.3 μm, p = 1 μm. b) An example random texture generated by setting l =1.1 μm, hrms =0.8 μm, p = 4 μm. c) An example random texture generated by setting l =0.6 μm, hrms =0.8 μm, p = 4 μ

Figure 19: a) Comparison of spectral absorption of untextured (film) and textures silicon with varying l and h_{rms}. b) $|E(\lambda)|^2$ distribution of untextured Si. c) $|E(\lambda)|^2$ distribution of textured silicon with l =0.1 μm and h_{rms} =0.3 μm. d) $|E(\lambda=0.5\ \mu m)|^2$ distribution of the texture with l =1.1 μm , h_{rms} =0.8 μm at λ =0.5 μm.

Figure 20: a) Spectral absorptions of random textures for N =10^{14} and 5x10^{15} cm^{-3}. b-c) Spatial absorption profiles for N =10^{14} and 5x10^{15} cm^{-3} at λ=0.5 μm. d) Absorption of a random texture and deterministic texture with varying p for N =5x10^{15} cm^{-3}. e) $|E(\lambda=0.5\ \mu m)|^2$ distribution for the deterministic texture with p =1 μm.

Figure 21: a-b-c) $|E(\lambda)|^2$ at wavelengths of 0.75, 1.5 and 3 μm for the pyramid dimensions of p =1 μm, h =3 μm and carrier concentration of 10^{14} cm^{-3}

Figure 22: a-b-c) $|E(\lambda)|^2 \times \sigma(\lambda)$ at wavelengths of 0.75, 1.5 and 3 μm for the pyramid dimensions of p =1 μm, h =3 μm and carrier concentration of 10^{14} cm^{-3}.

Figure 23: Scheme for analogy between silicon pyramid and stacked half-wave antennas

Figure 24: a) Representation of individual half-wave antenna with thickness 2R and length L, on the pyramid silicon. b) Calculated resonance condition for varying R values and corresponding L values. Lower and upper bounds of the error bars stand for R= λ/50 and λ/20. L = $\lambda_{Eff}/2$ values are obtained at R =$\lambda_1/45$, R =$\lambda_2/37$ and R =$\lambda_3/22$ which is equal to the width of the pyramid where first side mode occurs.

Figure 25: a-b-c) $|E(\lambda)|^2$ distributions at λ =3 μm wavelength for p =1 μm, 2 μm and 4 μm respectively. d-e-f) $|E(\lambda)|^2$ x $\sigma(\lambda)$ distributions at λ =3 μm wavelength for p =1 μm, 2 μm and 4 μm respectively.

Figure 26: a) Scheme for the black silicon as a waveguide problem composed of high index (core) and low index (cladding). b-c-d) Dispersion diagrams for d =0.06, 0.2 and 0.35 μm at which effective wavelength matching condition is satisfied for wavelengths of 0.5, 1.5 and 3 μm wavelengths.

Figure 27: a-b-c) Dispersion diagrams for d =0.7, 1 and 2 μm and supported TM modes with cut-off wavelengths labeled.

Figure 28: Comparing Absorption of Flat and rough (lx=100 nm, ly=100 nm and h=50 nm) Tungsten finite thickness film by FDTD solution

Figure 29: The effect of (a) Correlation length and (b) RMS height in the absorption spectra of random rough surface Tungsten

Figure 30: The RMS height effect on bandwidth of absorption

Figure 31: (a) The effect of correlation length for W anisotropic rough surface (b) Isotropic rough surface with l=200 nm and h=100 nm. (c) Anisotropic rough surface with l_x=100 nm, l_y= 400 nm, and h=100 nm. (d) Anisotropic rough surface with l_x=200 nm, l_y=400 nm, and h=100 nm

Figure 32: The RMS height effect on the absorption of the anisotropic rough surface of Tungsten with lx=100 nm, ly=400 nm

Figure 33: a) Reflectance of homogeneous multilayers for increasing number of layers. b) Spectral reflectance of a multilayer with 8 layers designed for α =0.7 with TiO_2 and air. c) Reflectance coefficients of the multilayer whose spectral reflectance is given in Fig. 4(b) on -S plane. d) Comparison of optical thickness of the multilayer structure on which even multiples are marked.

Figure 34: a) Analytical solution of the 8-layered structure obtained analytically by characteristic matrix method [60] vs. FDTD solution with number of mesh points of 14. b) Mesh accuracy vs. absorption percentage of the incident radiation.

Figure 35: a) Reflectance spectrum of the structure with 8 layers in which lift-off layers (n =1.58) of various sizes are added. b) Reflectance spectrum of the structure with 8 layers in which lift-off layers (100*100 nm) of different refractive indices are added.

Figure 36: a) Scheme for the periodically arranged morpho butterfly inspired multilayer features. b) Temperature change vs. linear length change for initial lengths of 0.5, 1 and 1.5 μm.

Figure 37: a) Average reflectance of structures for varying distance/periodicity. b-c-d-e) Spectral reflectance of the structures for varying distance/periodicity.

List of Tables

Abstract

This abstract is publicly releasable.

The principal motivation of this proposal is to provide a better understanding of the interaction of infrared radiation with aerospace materials in extreme environments. In this context, the surface roughness of the materials surface has an important impact on the reflection and absorption of incident radiation from material surfaces. Here, we developed a computational model for surface roughness effects to understand the interaction of infrared radiation with rough surfaces of materials, including polar dielectric and refractory metals. A detailed theoretical formulation and a numerical implementation was achieved based on the small perturbation method/small slope approximation (SPM/SSA). The code is capable of various statistical descriptions for rough surfaces, including Gaussian power spectral density. Using the developed computational code, we investigated the effects of various rough surface parameters, such as correlation length and surface roughness height, on the reflection and absorption spectrum of different materials, including polar dielectric and refractory metals.

1. Introduction

Research on broadband spectral reflection and absorption has attracted increasing attention recently due to the wide range of applications in both science and industry. Extensive literature in broadband radiative cooling systems [1–3] , solar absorbers [4–6], broadband anti-reflectors [7,8], space applications [9,10] points out the importance of this issue. Various techniques were proposed in the literature to increase the broadband spectral reflectance. Optical structures are known for their ability to control the spectral reflectivity and emissivity of surfaces [11,12]. With the recent advances in solar thermal and thermophotovoltaic systems and broadband reflection/emission applications, the engineering of surface structures, especially for materials that can sustain high temperature, has become essential. Deterministic surface structures, including 2D and 3D photonic crystals and meta-surfaces, have been widely explored to tailor the spectral response of the surfaces to the incident solar spectrum [13,14], increasing the important metrics such as emission efficiency [15].

Random surface roughness and surface distortions occur inevitably as a result of material processing and fabrication techniques [16,17]. For most situations, it is hard to get a completely smooth surface. In some cases, such as the surface roughness of metals, there are reports of improvement of the solar cell energy trapping [16], and the subsequent enhancement in subwavelength imaging [18,19]. As the impact of surface roughness on the system is crucial, it is important to quantify the impact of surface roughness.

Tailoring and smoothing the surface roughness can be challenging for thermomechanical stable materials, including refractory metals such as tungsten (W) and polar dielectrics, such as silicon carbide (SiC). These materials address problems like corrosion, adhesion, durability, and degraded reflectance performance due to damage, which are some issues that are encountered in various coatings [20,21]. Thermal solar [22–24], solar thermophotovoltaic [25], nuclear fusion [26–28], and aerospace applications [29] rely heavily on materials capable of operating at high temperatures. These materials must be able to operate at temperatures exceeding 1500 °C [16]. W is increasingly being used for different applications, such as solar devices, due to its outstanding chemical and thermal stability, high melting point, wear-resistance and the ability to store energy for over long periods of time [30–32]. Moreover, Tungsten is one of the refractory metals with intrinsic absorption in the VIS to NIR region that operates at high temperatures for the applications in which a high absorption is needed. Tungsten has high absorption in the visible range, but its large real part of the dielectric constant leads to a high reflection in the infrared regime. This causes flat films to have 60% or less absorption [33]. Tungsten can be textured in the shape of a pyramid micro/nanostructures to boost absorption [34].

Recently, employing dielectric multilayer thin-film coatings has been demonstrated as broadband reflectors that enhance reflectivity in shorter wavelengths [35,36]. Although these methods made significant contributions to the related literature, further research is required to achieve broadband reflectors with better thermomechanical stability and optimized topologies. Since the 1970s, the principle of using surface structures and surface patterns has been used as an alternative to thin-film coatings for controlling spectral reflection and absorption. Anti-reflective treatments are used extensively in the optic industry for applications ranging from lenses, lasers, cameras, solar cells, and visible and near-infrared light systems to windows, missile domes,

defense, and infrared laser systems [37,38]. In military, aerospace, and some industrial applications, which primarily utilizes infrared (IR) spectrum, reflection is a major issue. A common approach to improve optical reflection is to use several thin layers of dielectric materials that are mounted on the exterior surface of the window or optical component [39]. Enhancing photon absorption by increasing the active layer thickness is a relatively simple method, but the balance between charge and absorption also limits the thickness of the layer. One of many techniques for enhancing absorption without raising the actual layer thickness is to pursue a light attenuating structure, allowing the number of internal passes inside the functioning layer to improve the total length of the optical path [40]. At higher frequencies, the surface texture has a significant impact on the material's interaction with the electromagnetic wave [41]. Textured or porous layers can scatter light, and hence, intensify the duration of light travel through the absorber. Patterned surface structures, such as pyramidal structures [34], blazed gratings [16], and complex square gratings [42] of W, have been investigated by numerical approaches, such as finite difference time domain (FDTD), and experimentally demonstrated to get high absorption efficiencies. Periodic thin-film dielectric coatings deposited over refractory metals were also proposed to reduce absorption [35]. Extending such investigations of refractory metals of deterministic structures to refractory metal surfaces with random surface roughness is of interest.

There is also abundant literature for surfaces with deterministic textures for absorption/emission enhancement. In recent years, with the advancements in nanotechnology, periodically arranged surface textures are heavily utilized in the field of photonics due to the capability of resonance excitement. Frequency selective structures composed of silicon is reported for mid-infrared applications [43,44]. Issue with these structures suffer from low bandwidth of absorption due to resonant based nature. To overcome low bandwidth issue, different structures that combines multi-resonances together are studied in the literature [45,46]. However, those structures suffer from reduced absorption efficiency due to the destructive interference of different resonance modes. Besides the mid-infrared applications, periodically arranged surface textures are also developed for applications in visible and near-infrared spectrums [47,48]. In [47], structures are capable of strongly trapping the light in silicon for solar cell applications. Another study [48] proposed a hybrid structure, which sandwiches silicon structure between a polymer and a textured gold layer. Hybrid structure traps the light inside the silicon very effectively, thus resulting in high absorption in 0.3 -2 um interval reaching up to 90 % levels. However due to the hybrid nature, such structure requires several fabrication steps which makes it less feasible for fabrication. Black silicon devices composed of periodically arranged textures, for which some of the examples are given above, owe the absorptance enhancement to the field enhancement inside the silicon. High field enhancements in these devices are either attributed to resonance or light trapping effects due to sandwiched silicon. However, physics of the field enhancement in pure silicon structure, which neither support plasmonic resonances nor benefit from multiple reflections, is not clarified. Absorptance spectra of pyramid like textures composed of pure silicon is approximated by a multilayer structure with effective medium theory in [49]. Although computational results well agree with the experimental results, such approach does not able to explain the underlying physics. It shows that absorptance spectra of periodic surface textures can be mimicked with a multilayer structure which benefits from destructive interference of the reflected beams on the front surface.

In the literature, the effect of surface roughness on the interaction of electromagnetic waves with various surfaces has been investigated in detail for various other applications [50,51]. Both

experimental and theoretical studies of the interaction of rough surfaces with electromagnetic waves have led to significant improvements at various spectral regions [52,53]. Surface roughness effects in solar cells have attracted significant interest, as surface texturing in solar cells has been shown to improve the efficiency of solar cells [54,55]. Experimental studies related to surface roughness effects in solar cells have attracted significant interest, since surface texturing in solar cells have been shown to improve the efficiency of solar cells [55]. In addition to these studies, another area that the interaction of rough surfaces and electromagnetic waves have attracted significant interest is the study surface plasmon excitation with rough surfaces [45,56–58]. In the literature, however, there is a lack of studies on the surface roughness effects of refractory metals. As the topology of random surface roughness is quantified by the power spectral density (PSD), the modeling and simulation of random roughness with direct numerical approaches such as FDTD or finite element method (FEM) is challenging.

Despite the established literature on rough surface scattering from surfaces, surface roughness effects on thermomechanical stable materials have been largely ignored. With the increasing interest in thermomechanical stable materials, including refractory metals and polar dielectrics, an investigation of surface roughness effect on their broadband reflection spectrum is necessary. To address these issues, in this project, at first step we developed a model and investigated the impact of surface roughness on the spectral reflectivity under a broadband illumination [59]. We applied small perturbation method/small slope approximation (SPM/SSA) methods [60] to study reflectivity change in a broadband spectrum caused by Gaussian roughness for thermomechanical stable materials. The effects from the optical properties of materials and the surface roughness structures are studied and discussed.

Demand for high absorptivity attracts the attention of the researchers, and therefore lead to various type of silicon based photonic structures with high absorptivity, which are also known as black silicon [61,62]. In the literature, black silicon is achieved by introducing geometrical textures on the surface of silicon. Although high absorptivity over a broad spectral band is reported with surfaces with various textures, the underlying physical mechanisms that lead to high broadband absorptivity, is still an area that requires further research.

Black silicon has attracted attention of the researchers when it was fabricated by reactive ion etching (RIE) in which microstructures with high depth to width ratios were observed [62]. Later, black silicon with high absorptance in the 0.5 -2.5 μm spectrum band is demonstrated [61] by fabricating the surface textures using laser chemical etching. Enhanced absorption is attributed to the increased light trapping effect due to the spikes with high depth to width ratio. While abundant several studies exist in the literature regarding the experiments and fabrication techniques for micro-structured black silicon [63,64], fundamental physical mechanisms that yields this behavior have not been equally investigated. Scattering characteristics of electromagnetic waves from such random rough surfaces for various applications have been studied in the literature.

At the next step, in this project, we uncovered the mechanisms of the enhanced broadband absorption in micro-structured silicon with random and deterministic textures, especially at wavelengths above its bandgap [65]. We considered texture geometry and doping concentration as major influential parameters on the absorptivity of the black silicon and linked those parameters to electromagnetic phenomena, which induce high field intensities. Random texture geometries

are analyzed by expressing them by random Gaussian surfaces and spectral characteristics are obtained. Surface geometry is characterized by root-mean-square (RMS) of surface height, h_{rms} and transverse correlation length l_c. Electromagnetic responses of those structures are analyzed by finite difference time domain (FDTD) [66] simulations. Then, spectral characteristics of random textures are compared to periodicity controlled deterministic patterns, and the field distributions are calculated for analysis with FDTD [66]. In summary, geometry of randomly and deterministically textured black silicon structures are studied, results are analyzed based on field distributions. During the analysis, we considered the high field enhancement problem in black silicon as reciprocal of a waveguide problem in which multiple modes are supported throughout the geometry. In addition, high coupling in the transverse directions are observed in the analysis and coupling condition is estimated by adapting an effective wavelength method, which was originally proposed for optical antennas [67]. Our findings show that overall field enhancement in the pure-silicon structure stem from these two different phenomena depending on the width of the features of the textures. These findings reveal the underlying physics of the broadband absorptivity enhancement in black silicon, which can aid the future studies in the field.

As another application, rough surfaces can be used as selective absorbers which are commonly used in various fields due to their high absorptivity at specific wavelengths [68]. Spectrally selective filters can be used in various of applications involving solar absorbers [69], sensors [70], passive cooling [2,71], and thermophotovoltaic devices [72]. Optimization of energy use could be achieved by using the control of solar spectra. In addition to the consideration of cost, having the right transition wavelength can increase the efficiency of a solar absorber for specific applications significantly. Solar selective coatings are more common spectral selective absorbers studied in the literature [73]. Nanostructures can act as spectrally selective absorbers on the substrates [6]. While several studies exist in the literature regarding nanostructures' effect on the absorption spectra, the ability of random textures to use as spectrally selective absorbers has not been studied yet. The non-periodic structures can achieve high absorption rates, with structural sizes of one micron [74].

In this project, a random distribution of surface features with varying feature profiles and depth is used to obtain high absorption in Tungsten [4]. Scattering at rough interfaces between the absorber layers causes a change in the electromagnetic field angle of incidence within the absorber layers. This leads to a phenomenon known as internal coupling, which allows light to couple inside the absorber [75]. Using this concept, randomly textured surface substrates have been successfully used for the integration into solar cells of rough interfaces [75]. Here, we use this concept for Tungsten surfaces, a stable thermomechanical material, to increase the length of the optical path in a thin absorber layer significantly. Our approach goes one more step to demonstrate broadband spectrally selective absorber using Tungsten anisotropic rough surfaces. In this case, the formation of anisotropic surface can be achieved by stretching an isotropic surface in certain directions, resulting in different lateral correlation lengths. It represents random rough surface interface with varying correlation length in the x and y directions. We propose a technique to engineer the surface morphology based on anisotropic surface roughness for improving the surface optical characteristics. Isotropic and anisotropic random rough surfaces of Tungsten with various RMS height and correlation length are investigated. The random rough surface in this study is characterized by Gaussian power spectral density (PSD) with RMS height and correlation length. Surface properties of textured tungsten surface are modeled using the finite-difference time-domain (FDTD) technique, which enables analysis of textured Tungsten surface absorbance. Using

this method, a high absorption over a broad spectral band is obtained without adding any extra layers or coatings.

As mentioned earlier, optical nanostructures are another way of enhancing reflectivity of refractory metals. Researchers have been inspired by the optical nanostructure of insects to design and optimize multilayers. Among these insects, Morpho butterflies are known for their excellent multifunctional features of photonic structure wings [76]. These morphologies have been applied to the design and fabrication of bio-inspired sensors such as thermal infrared and pH sensors [77,78], chemical sensors [79,80] , gas sensors [81], robotic tactile sensors [82], and acoustic sensors [83] alongside with applications in microfluidics [84,85] and radiative cooling technology [86,87]. The multilayered thin-film nanostructure wings of morpho butterflies play an important role in controlling the reflectivity of light. In several studies, researchers optimized Morpho butterflies' wing structure to increase reflectivity in the narrowband spectrum. The literature results demonstrate that alternating the number of layers, the distance between the layers and, the shape and thickness of the layers not only impact reflectivity but also are responsible for the wide-angle reflectance [88,89]. As indicated in the literature, increasing the number of layers and reducing the distance between the ridges increase the reflectivity [90,91]. In addition to the structure morphology, coating materials can also affect the reflectivity. For instance, researchers have used the periodic arrangement of high/low index thin film layers to tune the spectral reflectivity of morpho butterfly-like structures [92].

Previous research also shows that the periodic structure of morpho butterfly wings helps them have lower wing temperature. This indicates that the ridge distances between periodic structures enhance convection from the wings to the ambient air, which decreases the thermal stress on the wing nanostructure. This thermal/heat transfer property of the morpho butterfly wing's nanostructure has been implemented to reduce the thermal load on the multilayered structures [93]. To date, developments in numerical methods have opened up numerous approaches to optimize the structure of multilayer thin-film coatings. Implementing the genetic algorithm [94], needle optimization technique [95], evolutionary algorithm [3], and deep learning algorithms [96,97] to design film structures are some of the well-known methods. By benefiting from those methods, multilayers that mimic the geometry of the observed patterns in nature can be designed. By doing so, the advantages of structures that already exist in nature can be coupled to artificial structures.

At the last stage of this project, we used a bio-inspired multilayer structure to increase the broadband reflectance of the thermomechanical superior materials [98]. Layer thicknesses of homogenous thin-film structures with predetermined layer numbers and materials are optimized such that impedance mismatch between the structure and incident medium is maximized to achieve broadband reflectivity. To benefit from thermal advantages of the morpho butterfly wings-like structures [99], spectral characteristics of such structures are studied by introducing periodicity, transforming homogenous multilayers to inhomogeneous structures. Final structures exhibit very high, reaching up to 90 % levels, broadband reflectance in 0.3-3 μm spectra, which prevents the absorption of incident radiation from high-temperature sources in these spectrums and leads to increased thermomechanical stability.

2. Methods, Assumptions & Procedures

In this research project to control optical properties, especially absorption, reflection and transmission, novel design techniques for the field of spectrally selective surfaces, using random rough surfaces and nanostructures to control the optical properties is proposed and explained for the resulting behaviors.

2.1. Surface Roughness Generation

To understand the random surface roughness effect, a rough surface configuration shown in Fig. 1 is considered. Light illuminates the surface from vacuum with an incident angle θ_i and azimuth angle ϕ_i. As the surface is not flat, different facet angle would cause reflection of light to different directions. The directions of scattered light are thus labeled with θ_s, ϕ_s. To study the broadband reflectivity and emissivity, we considered normal incidence of illumination, where $\theta_i = 0$. Surface roughness is quantified in terms of the root mean square (RMS) of surface height σ and the transverse correlation length l. The power spectral density (PSD) of the surface is mathematically the Fourier transformation of the surface height self-correlation function [100]. The integration of PSD function over k-space results in the room-mean-square (RMS) of surface height, thus s. Sinusoidal surface shapes will show as a delta function for the PSD. For a Gaussian surface, the roughness is randomly distributed with a PSD function, which follows a Gaussian distribution, the PSD of which is given as [100]

$$W(k_x, k_y) = \frac{l^2\sigma^2}{4\pi} e^{-\frac{(k_x^2+k_y^2)l^2}{4}} = \frac{l^2\sigma^2}{4\pi} e^{-\frac{k_\rho^2 l^2}{4}} \quad (1)$$

where l is transverse correlation length, σ^2 is the surface height variance, $k_\rho^2 = k_x^2 + k_y^2$, which is the wave-vector at radial direction. In Eq. 1 we assumed same correlation length along x and y direction, which is $l_x = l_y$, thus the random roughness is isotropic with no azimuthal angle dependence.

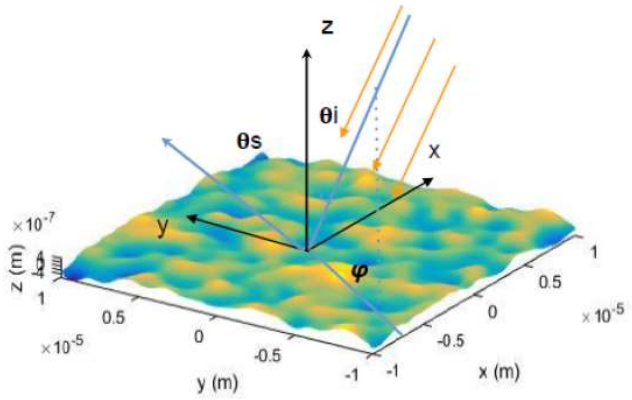

Figure 1: Schematic illustration of the surface roughness and the light scattering system.

These quantities are related to the auto correlation function by,

$$\rho(r) = h^2\, exp\left[-\left(\frac{x}{cl_x}\right)^2 - \left(\frac{y}{cl_y}\right)^2\right] \tag{2}$$

where cl_x and cl_y are the correlation length in x and y directions, h is the standard deviation of height and r shows the positions on the surface such that the rough surface structure can optionally generate textures as shown in Fig. 3(a). The integration of the power spectral density (PSD), which is the Fourier transformation of the surface height self-correlation function [101], over k-space results in the RMS of surface height. Three common spectral density functions are Gaussian, Power-Law and Exponential spectra.

Based on the previous experimental studies, wet-chemical etching, which produces isotropic textures, is the most effective way for obtaining damage-free Si texture among various surface treatments including annealing and oxidation [102]. Isotropic distribution assumption is used in previously reported analysis of black silicon [103,104]. In line with those studies, random roughness surface profile is considered to be homogeneous and isotropic. In this study, isotropic gaussian rough surface approximation was utilized and cl_x=cl_y=cl. A statistically homogeneous surface means the distribution of height is equally possible at any position within the surface. An isotropic surface is that the correlation function of surface heights is independent of the direction between two corresponding surface points' locations.

The roughness is generated by creating a matrix of uniform random numbers in *k* space (wave vector). For this purpose, the random number generator is considered in the script of simulations enable us to generate the Gaussian random number. The high frequency components (short wavelengths) which came from conversion of time functions into waves of different frequencies and are rapidly changing in space, are removed, and the resulting values are transformed back to real space. In this case, a single import object (surface option) is used to define the entire object. The upper surface of this object is defined by a 2D matrix containing the surface height as a function of x and y. Then the surface matrix in k-space fills with uniform random numbers. It is then filtered according to the real roughness data extracted from atomic force microscopy (AFM) images to remove all high frequency components [53] and the actual surface is realized by applying the Fourier transform (FT) on the filtered k-space. The matrix is transformed back into real space, where the amplitude is corrected. Due to the way the Fourier transform is setup, the roughness will be periodic with period x, y span. This is convenient when using periodic boundary conditions. The import object is then added to the simulation. For other PSDs such as second order Power-Law and exponential spectrum the spectrum density function is given by Eq. (3) and (5) respectively. For Power-Law PSD is given by

$$w = \left(\frac{cl_x cl_y h^2}{4\pi}\right)\left\{1 + \frac{\Gamma^2(N_p - 1/2)}{\Gamma^2(N_p)}\left[-\left(\frac{K_x cl_x}{2}\right)^2 - \left(\frac{K_y cl_y}{2}\right)^2\right]\right\}^{-N_p} \tag{3}$$

where Γ is the Gamma function, N_p is the order and the auto-correlation function for Power-Law spectrum comes from:

$$\rho(r) = h^2 \left\{1 + \frac{1}{N_p}\left[-\left(\frac{x}{cl_x}\right)^2 - \left(\frac{y}{cl_y}\right)^2\right]\right\}^{-N_p} \tag{4}$$

and for Exponential spectrum:

$$w = \left(\frac{cl_x cl_y h^2}{\pi^2}\right)\left\{1 + (K_x cl_x)^2 + \left(K_y cl_y\right)^2\right\}^{-1} \tag{5}$$

The auto correlation length for Exponential spectrum is as follow:

$$\rho(r) = h^2\, exp\left[-\frac{|x|}{cl_x} - \frac{|y|}{cl_y}\right] \tag{6}$$

Random textures for mentioned PSDs (Gaussian, Power-Law and exponential) are shown in Fig. 2. For this project the Gaussian type of distribution is commonly used since it is commonly observed in nature structures with random textures [105].

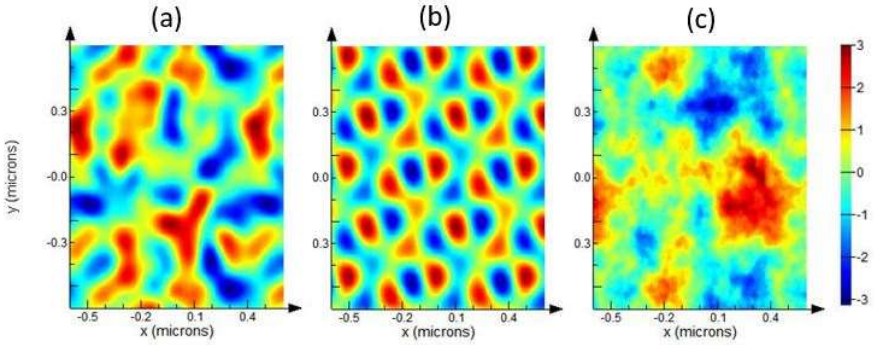

Figure 2:Random roughness texture generated by different PSD functions (a) Gaussian spectrum (b) Power-Law spectrum (c) Exponential spectrum.

2.2. Surface Roughness Effects on the Broadband Reflection Design Formulation

Theoretical methods in studying the surface roughness effect includes Lippmann–Schwinger equation [106], small perturbation method [50], and small slope approximation (SSA) [60]. The numerical methods used herein include moments of momentum (MoM) and Monte Carlo [107]. Among these techniques, the SPM/SSA method, up to second order, has been proven to be valid for studying the surface roughness with small variance or small slopes. It has been widely used in the remote sensing of thermal temperature of sea surfaces. In the literature, numerical techniques have been used for studying scattering from rough surfaces, including finite difference time domain (FDTD), finite element method (FEM) [108], method of moments and T-Matrix methods [18,109], and Monte Carlo approaches [110]. The SPM/SSA technique used in this study offers advantages for the problems that we address. Numerical approaches, such as FDTD- or FEM-based methods, provide solutions for deterministically described rough surfaces, whereas the SPM/SSA technique provides solutions for stocastically described rough surfaces. Compared to

SPM/SSA, typical MoM or Monte Carlo approaches are more time-consuming. The SPM/SSA method, up to the second order, contains the scattered beam contribution from both coherent and incoherent terms, thus resumes energy conservation [111].

In this study, we present a theoretical investigation on rough surface scattering. A simplified description of the method is discussed here. The reflection from the rough surface is given as [60]

$$R = \begin{pmatrix} |R_{hh}^0|^2 \\ |R_{hv}^0|^2 \\ 0 \\ 0 \end{pmatrix} + \int_0^\infty d\beta \int_0^{2\pi} d\varphi' C(k_0\beta, \varphi') \begin{pmatrix} g_h(\beta, \theta_i, \varphi_i, \epsilon, \varphi) \\ g_v(\beta, \theta_i, \varphi_i, \epsilon, \varphi) \\ g_U(\beta, \theta_i, \varphi_i, \epsilon, \varphi) \\ g_V(\beta, \theta_i, \varphi_i, \epsilon, \varphi) \end{pmatrix} \tag{7}$$

where $|R_{hh}^0|^2$ and $|R_{hv}^0|^2$ corresponds to the Fresnel reflection coefficients for horizontally and vertically polarized light incidence respectively. In Eq. 7, the contributions from the $|R_{hh}^0|^2$ and $|R_{hv}^0|^2$ terms account for the reflectivity of a flat surface. Reflectivity change due to the surface roughness are accounted in the second term in Eq. 7, where $\beta = k_\rho/k_0$ and [60].

$$C(k_\rho, \varphi) = k_\rho^4 W(k_\rho, \varphi) \tag{8}$$

By substituting Eq. 8 into Eq. 1, we obtain

$$C(k_\rho, \varphi) = \frac{k_\rho^4 l^2 \sigma^2}{4\pi} e^{-\frac{k_\rho^2 l^2}{4}} \tag{9}$$

Since weighting function g are functions of $\varphi_i - \varphi$ alone, integral over φ makes the dependent on φ_i to be vanished. In our calculations, we choose $\varphi_i = 0$. The g function in Eq. 7 can be expanded into its Fourier series as:

$$g_{\gamma,n}(\theta_i, \epsilon, \beta) = \frac{1}{2\pi} \int_0^{2\pi} d\varphi' e^{in\varphi} g_{\gamma'}(\theta_i, \epsilon, \beta, \varphi') \tag{10}$$

Meanwhile, function C given in Eq. 9 can be expanded into its Fourier series as:

$$C_n(k\beta) = \int_0^{2\pi} d\varphi' e^{-in\varphi'} C(k\beta, \varphi') \tag{11}$$

Therefore, the roughness caused reflection change can be written as:

$$\Delta R = \int_0^\infty d\beta g_{\gamma,0}'(\beta) C_0(k_0\beta) + 2\sum_{n=1}^\infty \int_0^\infty d\beta Re\{g_{\gamma,n}'\} C_n(k_0\beta) \tag{12}$$

Considering the large range of wavevectors that are going to be analyzed, each azimuth harmonic term in Eq. 12 is rewritten to be an linear integration over $\log_{10}\beta$, which is:

$$\int_0^\infty d\beta \mathrm{Re}\{g_{\gamma,n}'(\beta)\} C_n(k_0\beta) = (\ln 10) \int_{-\infty}^\infty d(\log_{10}\beta) \beta \mathrm{Re}\{g_{\gamma,n}'(\beta)\} C_n(k_0\beta) \tag{13}$$

Here, the weighing function g is determined by the material optical properties, and C depends only on the surface profiles. The magnitude of g values are derived from scattering coefficients with the full description illustrated in [112].

2.3. Broadband Absorption in Black Silicon

In this section, doped optical properties calculations is explained. Generated structures' electromagnetic response is computationally obtained in 0.3 – 3 μm spectrum interval. The random rough surface generation methodology is similar to the methods expressed in section 2.1. In this section, 2.3, procedure for obtaining optical properties with doping is summarized.

A rough surface configuration shown in Fig. 3(c) is considered for explaining the random surface roughness effect. The homogeneous random rough surfaces can be generated using spectral density function and discretization of it. In this case, the roughness is characterized by a specified sigma RMS (σ) which is describing the height profile and is identical to standard deviation of a random variable and correlation length (L_c) which is defining frequencies of spatial variations allowed over the surface. Large correlation length corresponds to small spatial frequencies and vice versa.

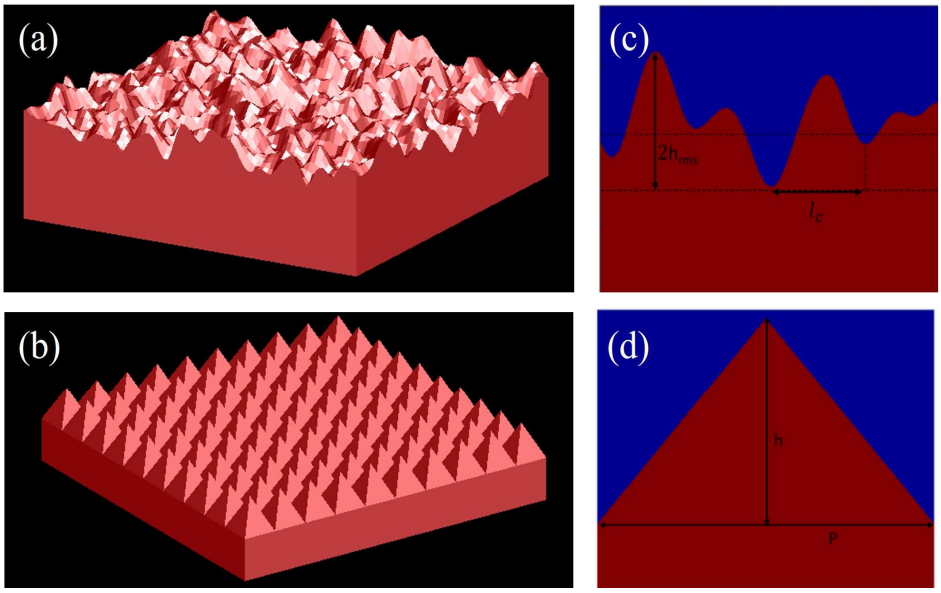

Figure 3: a) Example 3D visual of random texture formed by random Gaussians. b) Example 3D visual of periodicity controlled deterministic texture. c) 2D scheme for random texture with geometric parameters. d) 2D scheme for deterministic texture with geometric p

Reflection and absorption spectra have been determined in FDTD [105]. Periodic boundary conditions were used in the -x and -y directions, while perfectly matching layers (PML) were used in the lateral directions (-z direction). A broadband plane wave source was employed under normal incidence propagating. Reflection and transmission spectrum are evaluated with defining two monitors above and below the structure respectively. The absorption, A, is then calculated from

reflection, R, and transmission, T, as $A = 1-R-T$, in broadband spectrum. Field distributions over the geometry are also recorded in x-z plane to study the absorption spectra.

2.3.1. Optical Properties

Optical properties of the semiconductors can be modeled by Drude-Lorentz formalism, which is shown in Eq. (14),

$$\varepsilon(w) = \varepsilon_\infty - \frac{w_p^2}{w^2+iwv} + \sum_{j=1}^{m} \frac{f_j}{w_j^2-w^2-i\Gamma_j w} \tag{14}$$

and can be used to characterize dielectric function from spectral measurements [113]. First term in Eq. (14), ε_∞, is the high frequency permittivity which stands for the contributions from high-frequency electronic transitions. Second term (Drude formalism) is the expression for free electron contribution to the frequency dependent permittivity where W_p is the plasma frequency and v is the relaxation frequency. Expressions for W_p and v are given in Eq. (15) and (16) respectively as,

$$w_p = \sqrt{\frac{4\pi N e^2}{m^*}} \tag{15}$$

$$v = \frac{e}{\mu_c m^*} \tag{16}$$

where N is the carrier concentration, e is the electron mass and m^* is the effective mass in Eq. (15) and μ_c is the mobility in Eq. (16). Last term in Eq. (14), Lorentz formalism, stands for the contributions to permittivity coming from lattice vibrations and interband transitions of bond electrons. In Lorentz formalism, f_j stands for oscillator strength, w_j for resonance frequency and Γ_j for damping factor.

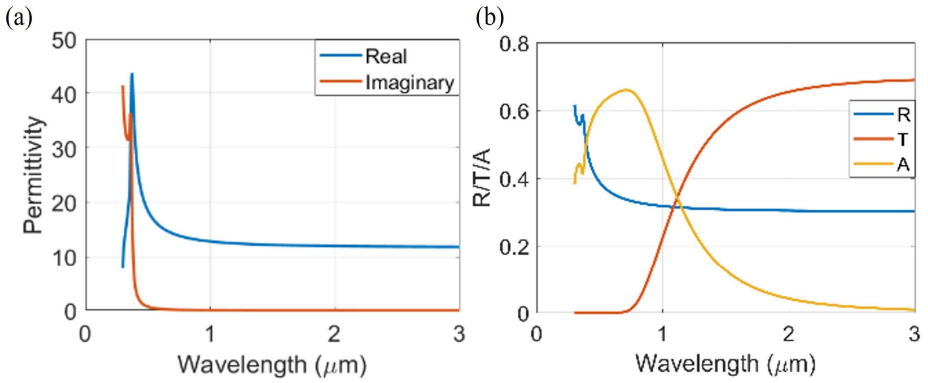

Figure 4: a) Real and imaginary part of the permittivity of the undoped silicon retrieved from [56]. b) Reflectance, transmittance and absorptance of Si film of finite thickness.

Drude formalism is sufficient to model the optical properties of Si for wavelengths longer than 3 μm, where optical properties are dominated by electron plasma of the material. However, to model the properties in wavelengths which are below bandgap energy of the Si, especially in visible spectrum, Lorentz term should be included to address the interband transitions. In Fig. 4(a) permittivity of the Si, retrieved from [100] is demonstrated and reflectance, transmittance and

absorptance of Si film of finite thickness is shown in Fig. 4(b). As seen from Fig. 4(a), real part of the permittivity of the Si is almost constant after 1 um. However, it has distinct peak around 0.5 um with finite imaginary part, due to effects of bounded electrons, which give rise to below bandgap absorption as shown in Fig. 4(b). Therefore, Drude-Lorentz formalism is required to model the optical properties in 0.3 – 3 um spectrum interval.

To obtain a Drude-Lorentz model for optical properties of Si, we fit Eq. (14) to permittivity data given in Fig. 4(a) and obtained the $\varepsilon_{\infty,}$ W_p, ν in Drude term and other Lorentz parameters. We set the number of Lorentz oscillators to 6. Fitting parameters are given in Table 1 and reference and fitted permittivity, as well as the spectral reflectance values are compared in Fig. 3. Reflectance is obtained by Fresnel equation given in Eq. (17).

$$R(w) = \left|\frac{\sqrt{\varepsilon(w)}-1}{\sqrt{\varepsilon(w)}+1}\right|^2 \tag{17}$$

Table 1: List of parameters and their values for fitting Drude-Lorentz formalism given in Eq. (3) to optical properties of Si given in [109].

Parameter	**Value**
ε_∞	5 [F/m]
W_p	0.5006 [eV]
ν	$7.33*10^{-7}$ [eV]
$f = [f_1:f_6]$	[1.33, 0.18, 1.61,1.49,1.53] [eV^2]
$w = [W_1:W_6]$	[4.50, 3.40,3.53,3.82,4.50,4.1] [eV]
$\Gamma = [\Gamma_1:\Gamma_6]$	[$2.73*10^{-5}$, 0.0025, 0.0874, $2.36*10^{-5}$, 0.064] [eV]

As shown in Fig. 5, reference optical properties and obtained properties by fitting agrees well and similar reflectance is obtained over the spectrum of interest. From the Drude-Lorentz equation obtained for pure Si, optical properties of doped silicon for various doping concentrations is obtained. Doping may significantly alter the optical properties depending on the doping concentration. Optical properties are linked to doping level by carrier concentration in the material. As shown in Eq. (15), carrier concentration has proportional relationship with the plasma frequency. In addition, it is also linked to mobility. Both plasma frequency and mobility are in the Drude part of the model, therefore, by modifying the Drude term in Eq. (16), permittivity for doped Si is obtained. During the calculations, we assumed constant effective mass for various doping levels. Although we considered n-type doping in analysis, given equations are valid and can be used with corresponding mobility values experimentally reported in [59] and effective mass for -p type doping.

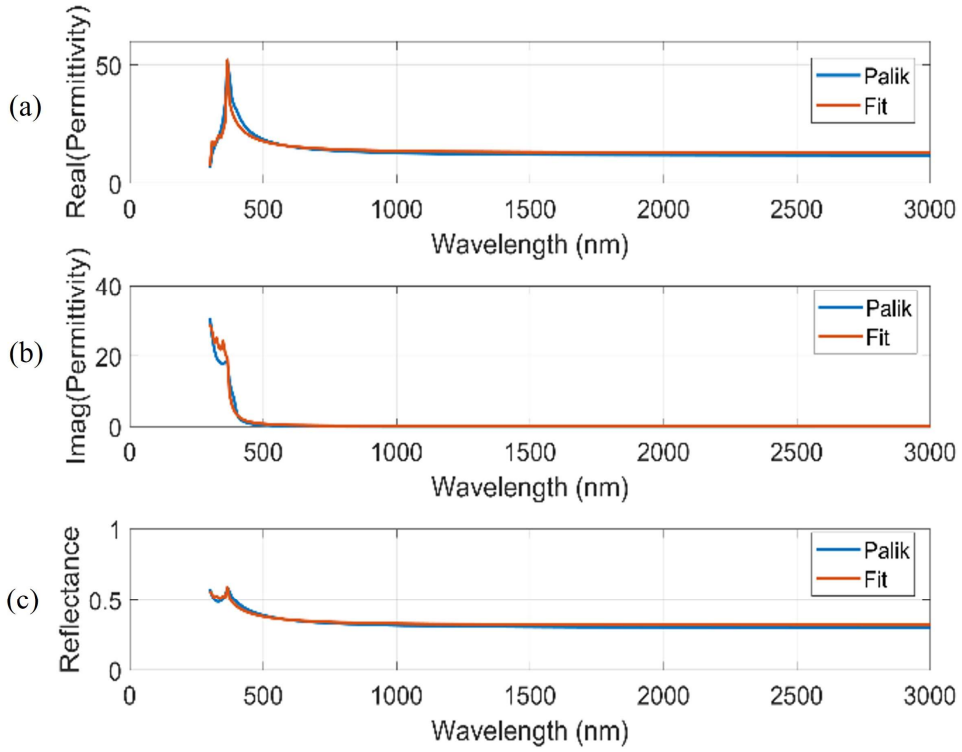

Figure 5: a-b-c) Comparison of real and imaginary part of the permittivity given in [96] and fit values for undoped silicon, and reflectance obtained from it and the fit.

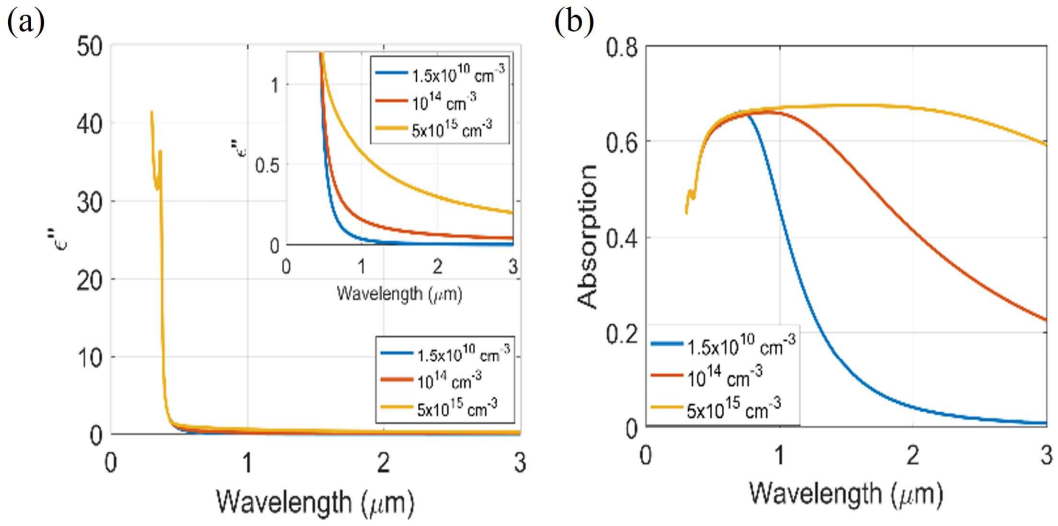

Figure 6: a-b) Imaginary part of the permittivity of Si with doping concentrations of $1.5x10^{10}$, 10^{14}, $5x10^{15}$ cm^{-3}. c) Absorptivity of silicon with carrier concentrations of $1.5x10^{10}$,10^{14}, $5x10^{15}$ cm^{-3}.

Effect of carrier concentration on plasma frequency is evaluated as given in Eq. (16). To include the effect of carrier concentration on mobility, experimental values reported in [59], for mobility

with respect to carrier concentration, are used in the calculations. We assumed the initial carrier concentration of Si is approximately 1.5 x 10^{10} $cm^{-3}$and obtained optical properties for n-type doping with different carrier concentrations. In Fig. 5, imaginary part of the permittivity of Si with n-type doping concentrations of 10^{14}, 5x10^{15} cm^{-3}.

With the increasing carrier concentration, considerable increase in imaginary part occurs, as shown in Fig. 6(a), therefore loss in the material increases. Increased loss in the material results in elevated absorptance/emittance even in the bulk form. As shown, imaginary part of the permittivity is not changed significantly around 3 μm and shorter wavelengths with carrier concentration of 10^{14} cm^{-3}. In Fig. 6(b), spectral absorptance of Si with the selected doping concentration is demonstrated. As seen, absorptance in broadband spectrum is significantly improved when carrier concentration is increased from 10^{14} to 5x10^{15} cm^{-3}. These findings show that even low doping concentrations, give rise to elevated absorptance/emittance in silicon. When combined with surface roughness/patterns, absorption is further improved by increased coupling with the incident waves and the structure. Absorption of textured structures, $A(\lambda)$, are obtained by

$$A(\lambda) = \oiint_S (|E(\lambda)|^2 \times \sigma(\lambda)) \cdot ds \tag{18}$$

where $|E(\lambda)|^2$ is the electric field intensity in the geometry and $\sigma(\lambda)$ is the optical conductivity and dependent on the complex part of the dielectric permittivity, $\varepsilon = \varepsilon' + i\,\varepsilon''$, as

$$\sigma(\lambda) = 2 \times \pi \times f \times \varepsilon''(\lambda) \tag{19}$$

2.4. Tungsten Based Spectrally Selective Absorbers design formulation

In this section, a numerical approach is applied to obtain the optical properties and spectral absorption of random rough surfaces of Tungsten in the range of 300-3000 nm. The procedure for obtaining optical properties from random rough surfaces is summarized. In the next step, the anisotropic random rough surface of Tungsten is examined, and the effect of this random texture on the optical properties of surface and Absorption bandwidth is reported. The schematic of the proposed system is shown in Figure 7. As can be seen from this figure, the isotropic and anisotropic random rough surface could increase the absorption in the VIS and NIF regions. Moreover, as Figure 7 (a) indicates, anisotropic random rough surface causes absorptivity of more than 95%, which can be used as spectral selective system. A schematic of isotropic and anisotropic random rough surfaces and their working principle in the scattering of light is displayed in Figure 7 (b). It is observed that all the UV and VIS light and some part of IF light are absorbed using anisotropic rough surfaces. Moreover, the top view of both isotropic and anisotropic random rough texture can be seen in Figure 7 (c).

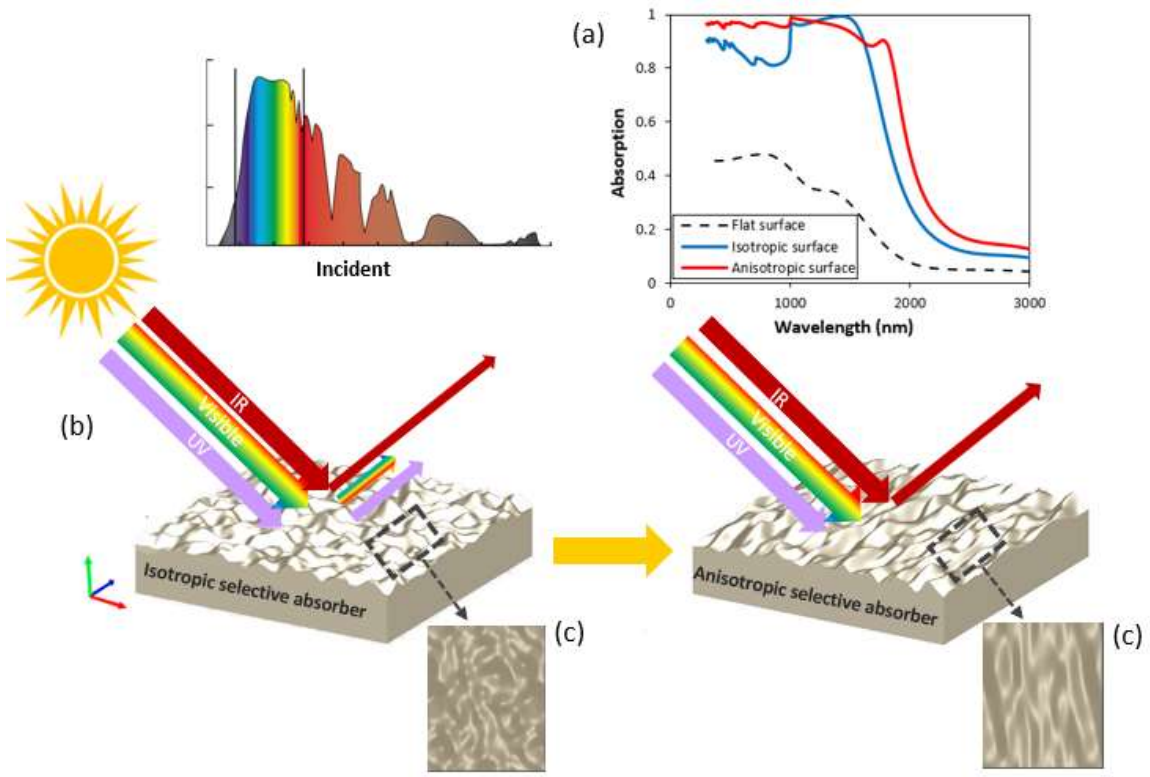

Figure 7: Schematic of proposed selective absorber (a) comparison of absorption spectrum (b) scattering performance of isotropic and anisotropic rough surfaces (c) top view of isotropic and anisotropic rough surface

Rough surfaces exhibit less reflectance or more excellent absorption than flat surfaces [114,115]. Surface roughness is one of the important factors affecting the reflectivity/emissivity due to the incident angle change on different facets [59]. In this study, random texture geometries similar to previous studies are characterized by their statical properties, include the height distribution specified as sigma RMS, which determines the spread of heights away from some smooth plane and represent the standard deviation of the distribution of surface heights and correlation length (L_c), which is defining the uniformity of the height over finite distances along the surface. In other words, the correlation length shows the distance between two statically independent points.

To get a better understanding of the light absorption characteristics of W refractory metal, the finite difference time domain (FDTD) simulations were carried out to obtain the full-wave solution of Maxwell's equations. The FDTD approach is one of the most appealing techniques for studying light dispersion and absorption from randomly formed small particles in computational electromagnetics. It produces a frequency-domain electric field and magnetic field distributions for all frequencies of interest. Our simulation is set in 3-D, and the upper and bottom surfaces in the z-direction are subjected to the perfectly matched layer (PML) boundary condition, and the periodic boundary condition is applied on the side surfaces in the FDTD simulation region. A broad frequency plane wave is irradiated from the top of the surface with the linear polarization along the x-axis. The transmittance and reflectance monitor are set on the bottom and top sides of the surface, respectively, to collect the propagated light. The light absorption spectrum is then visualized at different absorption resonance wavelengths. In the back-stretching plane, the

reflection spectrum is detected. Also, the magnetic (H) and electric (E) components of the electromagnetic radiation are parallel to the surface, while the wavevector k (direction of oscillation) is perpendicular to the structure. The permittivity of Tungsten is taken from Palik's book [116] and is illustrated in Figure 8. Under these conditions, the light reflection, transmission, absorption properties of random rough surfaces are evaluated. Tungsten's transmission in the entire spectral range is nearly zero, indicating an almost total absence of transmission. The power flow across a surface on an averaged time basis is defined by [117]:

$$P = \int Sds = \int \frac{1}{2} Re[E \times H^*] ds \tag{20}$$

in above formula E and H are the electric and magnetic field intensities, respectively. Here, H* denotes the magnetic field vector's complex conjugate, and s denotes the surface area. The reflectivity is given as:

$$R = \frac{P_r}{P_i} \tag{21}$$

where P_r represents the reflected light's power and P_i represents the incident light's power. Then to calculate the absorption coefficient of a solar absorber below formulated is used: [118]

$$A(w) = 1 - T(w) - R(w) \tag{22}$$

where T(w) and R(w) are the frequency-dependent transmission and reflection parameters, respectively. Maximum optical and thermal absorption is attained when the reflection and transmission coefficients are minimized. Since the optical properties of the material can be affected by both the intrinsic properties and the surface morphology, the study of surface engineering could be an excellent approach to change the optical properties.

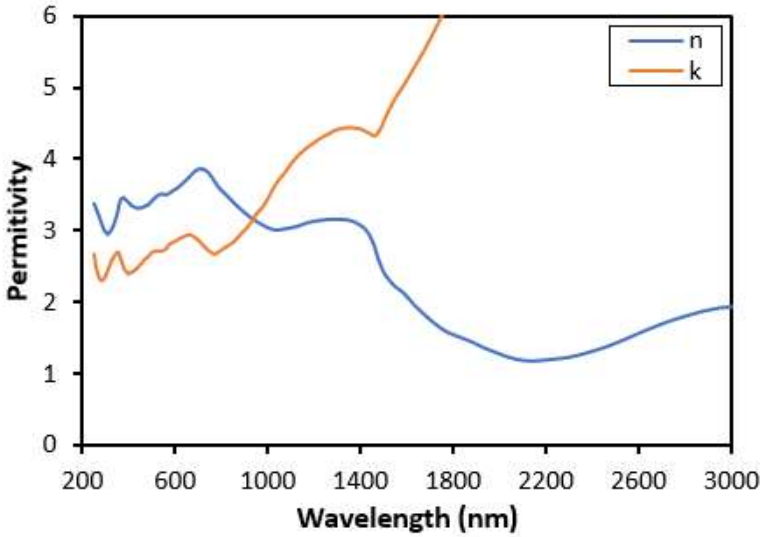

Figure 8: The real and imaginary part of the permittivity of the Tungsten

Numerous studies have been conducted on the control of absorption using surface microstructures such as shallow grating [119–121]. One advantage of optical control via surface gratings is the high thermal stability of optical devices, which are typically fabricated on bulk materials and thus do not contain thermal discontinuities, in contrast to multiple antireflection or filtering coatings. This indicates that spectral control via surface gratings is an appealing prospect for high-temperature applications.

Inspiring from the grating coupler, anisotropic random rough surfaces by taking advantage of increasing absorption by light trapping structure and benefits of optical control of grating microstructures could be a good prototype of passive spectrally selective absorber which is investigated in the current research. The anisotropic rough surfaces can be generated when a randomly rough surface has two different correlation lengths along x, y, marked as l_x, l_y respectively, and the reflection and absorption of the surface could be affected. Tungsten is chosen as the refractory metal which can use in high temperature and in compared to noble metals such as Ag and Au, has high thermal stability. The main principle behind this approach is to use less material and omitting the extra coatings and layers, which can be used as filters and absorbers. The top view of various correlation lengths for an anisotropic random rough surface can be seen in Figure 9.

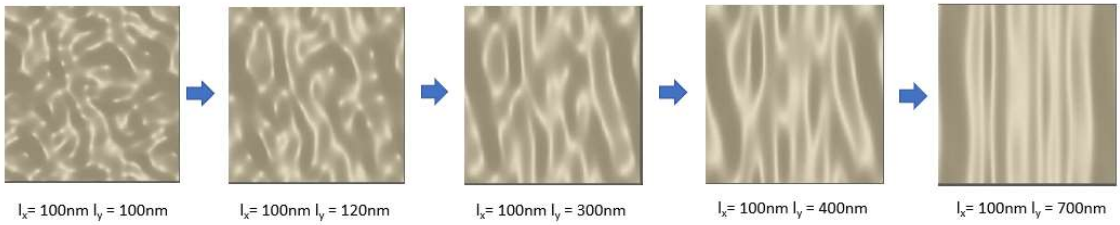

Figure 9:Anisotropic random roughness texture formed by random Gaussians

2.5. Broadband Reflectance of Tungsten with Bio-Inspired Multi-layers

Elevated temperatures in the systems lead to a reduction in both device performance and lifetime. Refractory metals like W, Ta, Mo, and Nb are widely utilized in such high-temperature applications not only for their higher melting points but also for their superior mechanical characteristics, which make them less vulnerable to corrosion and mechanical damage [122]. However, those metals suffer from low reflectivity in visible and near-infrared spectrums, 0.3 – 1 μm wavelength interval, at which thermal radiation from high-temperature sources is strong, as depicted in Fig. 10 (a).

In Fig. 10 (a), thermal radiation from the sun (obtained by thermal blackbody radiation from a surface at 5850 K and with a solid angle of 6.84×10^{-5} at a perpendicular angle of incidence. The reflectivity of the W is also plotted with respect to wavelength in Fig. 10 (a). The spectral distribution of absorbed power is also depicted in Fig. 10 (b) together with the incident thermal radiation. The red-shaded region corresponds to absorbed radiation power with respect to wavelength, and the blue-shaded region represents the reflected power. Incident and absorbed powers are obtained by calculating the areas under these curves. In the interval of 0.3 – 1 μm

interval (the red-shaded region in Fig. 10 (a)), more than 1100 W/m^2 power reaches the atmosphere, and this power increases with reducing distance to the sun. As seen from Fig. 10 (a), the reflectivity of W is around 50 % levels which leads to absorption of nearly 600 W/m^2 of the incident power. At wavelengths longer than 1 μm (the green-shaded region in Fig. 10 (a)), W has higher reflectivity reaching up to 90 % levels, preventing the absorption of incident thermal radiation at these wavelengths. Because of these spectral characteristics, spectral reflectivity of refractory metals should be enhanced in the broadband spectrum for more efficient use in high-temperature applications such as aerospace [9,10].

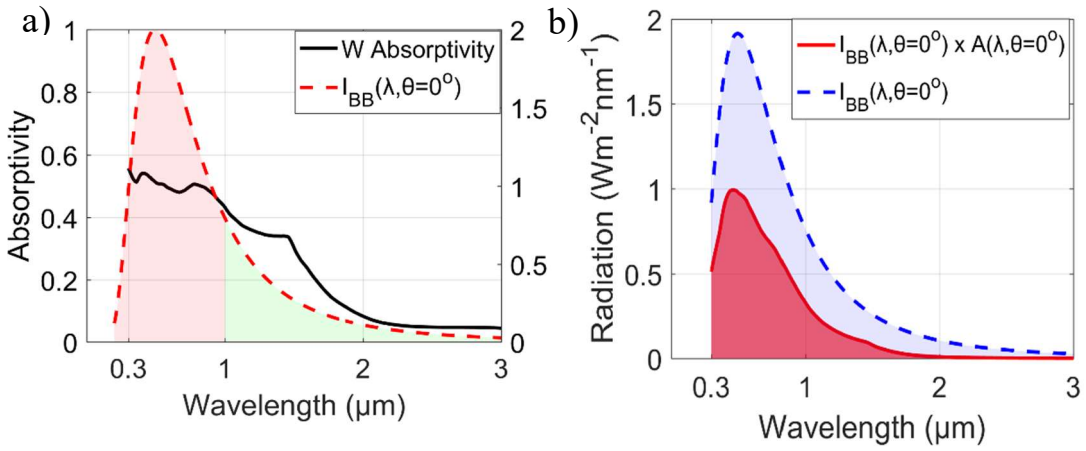

Figure 10: a) Spectral distribution of thermal radiation from the sun at perpendicular angle of incidence and spectral reflectivity of W. b) Spectral distribution of thermal radiation from the sun at perpendicular angle of incidence and absorbed power by -500 nm

Among many other coating types, homogeneous multilayer structures were previously reported to enhance the reflectivity of refractory metals [9,35,36]. Despite their high reflectivity in the broadband spectrum, implementing a high number of layers causes fabrication difficulties in these types of coatings. In addition to homogeneous multilayers, the spectral characteristics of the patterns observed on the wings of the Morpho butterflies, which are composed of multilayer features separated from each other, are extensively studied [123]. However, such features were not utilized to enhance the spectral reflectance of refractory metals.

Besides, although the spectral reflectance of the periodic multilayer coatings inspired by Morpho butterfly wing's nanostructures is explored in a relatively narrowband spectrum so far, the effect of periodicity of the multilayers on the broadband reflectivity of refractory metals is not studied. Schematic representation of the structures in which inhomogeneities are introduced in transverse directions is visualized in Fig. 11. Based on the previous findings, which state that periodic arrangement of multilayers, inspired by the features on the wings of Morpho butterflies, would enhance the thermal management capability of the coatings [86,93]. For this purpose, understanding the effect of periodicity on spectral characteristics is essential.

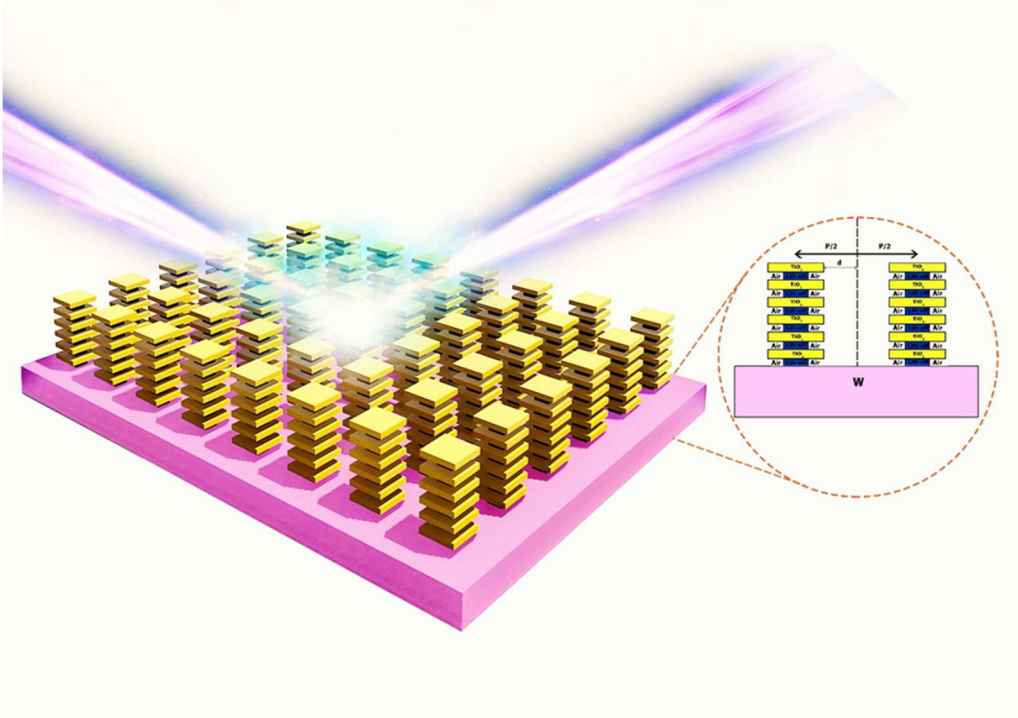

Figure 11: Schematic representation of multilayer structures inspired from wings of morpho butterflies.

The design of multilayer structures with predetermined layer numbers and layer materials is studied in this work to address these issues and fill the gap in the related literature. First, spectral reflectance in 0.3 – 3 μm of the multilayers composed of high-low index layers with a varying number of layers is optimized by tuning layer thicknesses. TiO_2 is chosen as high-index, and the air is selected as low index material. When excited with a plane wave, the incident wave encounters TiO_2 layers separated by air gaps of varying thicknesses. Spectral reflectance of the structures is formulated based on wave impedance approach, similar to the one used in [2], and optimization is conducted based on that formulation. When executed, the developed algorithm seeks a structure that maximizes the impedance mismatch between the substrate and the incident medium. Spectral characteristics of the resulting structures are both analyzed by wave impedance analysis and evaluating the total optical path that wave travels throughout the structure by summing individual optical thicknesses of the layers obtained by,

$$\delta_i = \frac{(2\pi n_i d_i)}{\lambda} \tag{23}$$

where δ_i is the optical thickness of the i^{th} layer, n_i is the refractive index of the medium/layer, d_i is the geometrical thickness, and λ is the wavelength.

As a next step, the effect of lift-off materials on the spectral reflectance of the multilayers is studied. Lift-off materials are needed to realize the air gaps between TiO_2 layers. Finally, to study the effect of periodicity, multilayers that do not have any inhomogeneities in transverse directions are transformed to structures depicted in Fig. 11, and their spectral reflectance is studied by FDTD.

In this case, the resulting reflectance spectrum characteristics are studied by obtaining the reflection coefficients/ *S* parameters of the studied multilayers with different periodicities by an *S* parameters retrieval method for electromagnetic metamaterials [124].

2.5.1. Design of homogeneous multilayers based on impedance mismatch

Starting from the intrinsic impedance of individual layers, which are solely dependent on material properties,

$$Z = \sqrt{\frac{\mu}{\varepsilon}} \tag{24}$$

and including the thicknesses of the layers and their interaction with each other, surface impedance of a multilayer composed of *N* number of layers can be expressed as,

$$\mathcal{Z}_i = Z_i \frac{\mathcal{Z}_{i+1} + Z_i \tan(\delta_i)}{Z_i + j\mathcal{Z}_{i+1} \tan(\delta_i)} \tag{25}$$

From the surface impedance of a multilayer structure, the amplitude of its reflectance coefficients and reflectance percentage is given as,

$$\Gamma = \frac{\mathcal{Z}_1/Z_0 - 1}{\mathcal{Z}_1/Z_0 + 1} \tag{26}$$

The reflectance coefficient values obtained by Eq. (25) at different wavelengths are schematized on a complex plane in Fig. 12(a). In Eq. (26), Z_0 is the intrinsic impedance of the air and is equal to 377 Ω and $\mathcal{Z}_1$is the surface impedance of the multilayer. By using Eqs. (24)-(26), reflection coefficients of a multilayer structure and its reflectance, $R(\lambda) = |\Gamma(\lambda)|^2$ can be calculated. Since reflection coefficients are complex quantities, they are visualized on a complex plane, called complex impedance plane/-S plane. An example distribution of complex reflection coefficients on the -S plane is represented in Fig. 12(a). It is observed that the reflection coefficients are distributed (green dots) inside a unit circle centered at the origin (blue circle). In Fig. 12(a), green dots correspond to reflection coefficients at different wavelengths, which always remain in the unit circle represented by blue color. This representation is very similar to the Smith chart [125] used in microwave and RF regimes for the purpose of impedance matching. From this representation, it is clear that zero reflectance at a wavelength is achieved only if the amplitude of the reflectance coefficient is zero, appears at the origin (red star). Since this condition is only satisfied if $Z_{Surf} = Z_0$, the origin of the unit circle is called a perfect impedance matching point. On the other hand, the magnitude of the reflectance coefficients on any point on the unit circle is always 1 ($|\Gamma| = \left|re^{i\theta}\right|, if\ r = 1$).

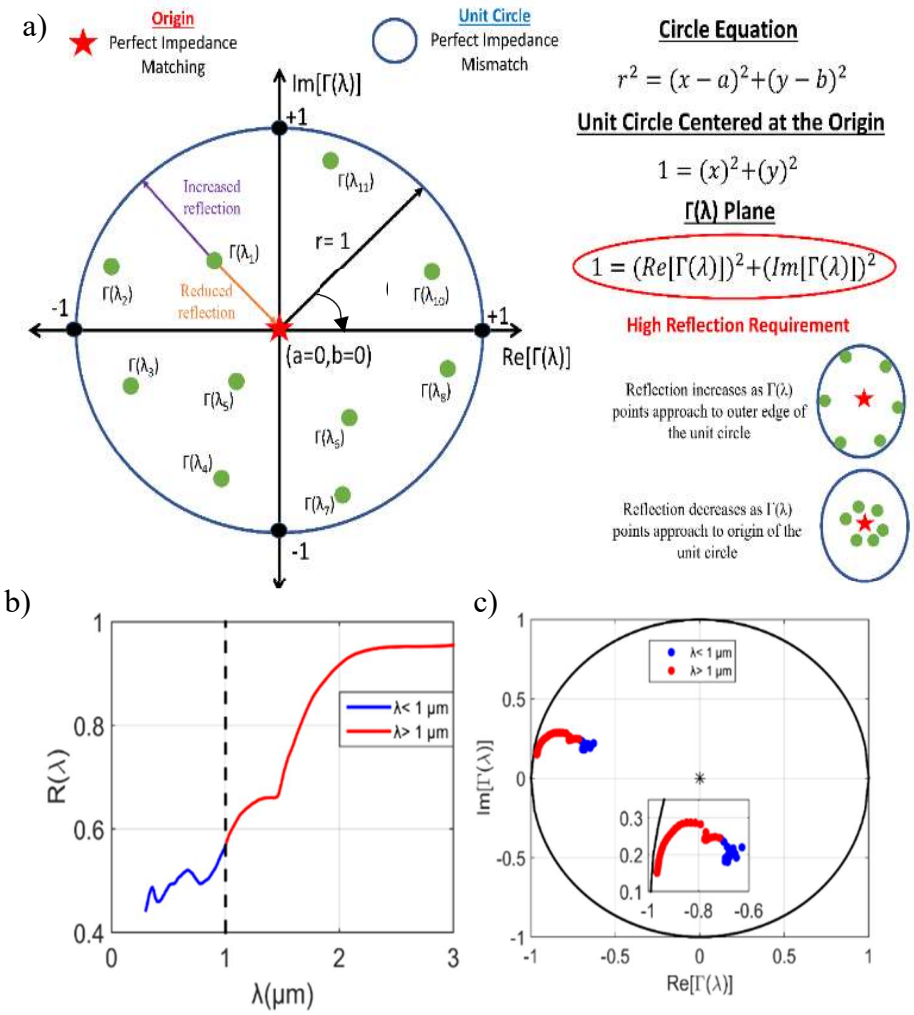

Figure 12: a) Representation of impedance mismatch method in -S plane. b) Reflectivity of W in 0.3 – 3 μm spectrum intervals. c) Reflection coefficients of W in -S plane.

Therefore, any point on the unit circle is called a perfect impedance mismatch point. Based on these, the following can be deduced: Reflectance is reduced as the reflectance coefficient approaches the origin, and it increases as the reflection coefficient moves away from the origin. Such characteristics of the reflectance coefficients on the unit circle (S-plane) can be utilized to engineer the reflectance spectrum of the multilayers. In Fig. 12(b), spectral reflectance of the tungsten substrate is shown, and corresponding reflectance coefficients are shown in Fig. 12(c). As seen from Fig. 12(c), W's reflectance is below 50 % at wavelengths shorter than 1 μm and starts to increase at longer wavelengths and reaches up to 95% levels. Reflection coefficients of low reflectance spectrum (blue points) are closer to the origin and start to approach the left side of the unit circle for longer wavelengths (red points). Here the aim is to preserve high reflectance at longer wavelengths while enhancing it in shorter wavelengths. Based on this, the design spectrum separated as low and high reflectance spectrum, and a weighting is introduced in the mathematical expression of the problem and defined as,

$$max\ \alpha \int_{\lambda_1}^{\lambda_2} \left| r(\lambda) e^{i\theta(\lambda)} \right| d\lambda + (1-\alpha) \int_{\lambda_2}^{\lambda_3} \left| r(\lambda) e^{i\theta(\lambda)} \right| d\lambda \quad (27)$$

where α is the weighting parameter, λ_1, λ_2, and λ_3 are 0.3, 1, and 3 μm respectively. α is chosen as 0.7 to keep the reflection reduction rate low at longer wavelengths while enhancing it at shorter wavelengths. Both homogenous and inhomogeneous structures' spectral characteristics are analyzed on the S-plane.

2.5.2. Analysis of introduced inhomogeneities in transverse directions

Effect of applied inhomogeneities in -x and -y directions on the spectral reflectance is obtained by FDTD simulations. Periodic boundary conditions were used in -x and -y directions, PML boundary conditions were used in the -z direction. Studied multilayer structures were excited with a -x polarized plane wave propagating in -z direction. Realistic optical properties for TiO_2, obtained from [116], are used in all the calculations. Lift-off materials were used in FDTD simulations to analyse realizable multilayers with a refractive index of 1.41, similar to one reported in [126], as well as for varying refractive indices and dimensions. Then a -S parameters retrieval method for metamaterials was used to obtain the -S parameters of the inhomogeneous multilayers [124]. Calculated -S parameters were used to analyse the spectral reflectance of the inhomogeneous multilayers.

3. Results & Discussions

In this section, results obtained by following the methods described in section 2, are reported. They are categorized under the sub-sections based on the problem definitions and applied methodologies. In subsection 3.1, results related to surface roughness effects on the broadband reflection for refractory metals and polar dielectrics are given. In the next subsection, surface roughness are used to design black silicon and the origins of the enhanced broadband absorption in black silicon is studied. In addition, effects of geometrical perturbations, which yield inhomogeneous structures to provide enhanced thermomechanical stability, on the absorption spectrum is analyzed. In subsection 3.3 similar methods are adapted to study tungsten based spectrally selective absorbers with anisotropic rough surface texture. In subsection 3.3 results related to broadband absorption are presented. In the final subsection, results of a impedance mismatch-based enhancement of broadband reflectance of tungsten with bio-inspired multi-layers are demonstrated. In this section, it is shown that surface engineering can be used to evaluate the resulting spectrum characteristics in broadband spectrum.

3.1. Surface Roughness Effects on the Broadband Reflection for Refractory Metals and Polar Dielectrics

As the PSD of sinusoidal surfaces are delta functions at the corresponding wave-vector k, each value of the weighting function g at a given k determines the reflection change caused by the corresponding sinusoidal surface. For the Gaussian surface in this study, we take the $0th$ harmonic of the weighting function into account. As a result, weighting functions depend only on the optical permittivity of materials for a chosen beam incident angle. To illustrate the different scattering properties of different materials in this study, weighting functions for materials with artificial dielectric constants are presented. Refractive index of material is represented as $n + ik$, where n and k correspond to the real and imaginary parts of the dielectric constant, respectively.

Fig. 13 shows the normal incidence weighting functions for dielectrics with $k = 0$, where the materials are transparent with no absorption. As can be seen, there is one strong resonance peak at $\beta = 1$ and one secondary resonance peak happens around the $\beta = n$. At $\beta = 1$, the corresponding space periodicity of the surface has the same periodicity of incident wavelength λ, where perfect phasing matching is provided for the reflected waved, therefore, causing less reflection. For the secondary resonance peak, the corresponding periodicity is λ/n, which is the wavelength of beam inside the material. As there is no absorption from the material, reflection change are purely brought by the roughness periodicity caused momentum change. When the surface roughness gets larger than the incident wavelength, it behaves like smooth surface and weighting function magnitude gets close to 0. Similarly, when the surface roughness gets very small, the weighting function also decreases. Surface roughness with the periodicity between incident wavelength and the wavelength in the material have strong effect of the surface reflection and the effect slowly decreases as roughness gets smaller.

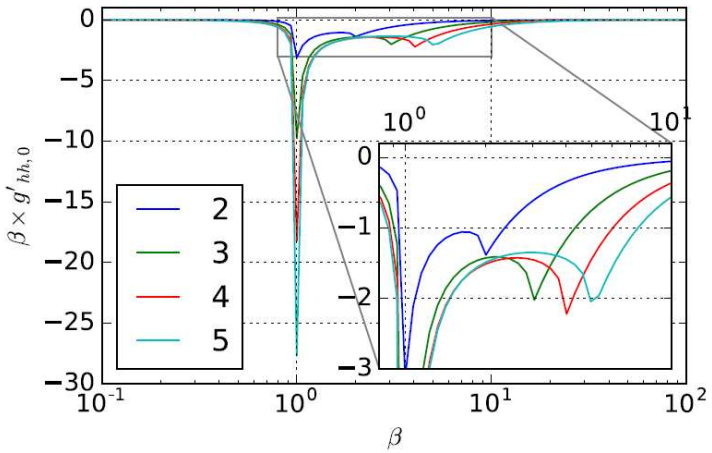

Figure 13: 0th order weighting function magnitude with respect to optical constant for materials with k=0. The legend in the figure shows the corresponding n value for each curve. Inset plot corresponds to the region in the grey box.

The materials experience absorption of penetrated beam, which can be quantified by the imaginary part of permittivity, $\epsilon = n^2 = n^2 - k^2 + 2nki$. At $n = k, \epsilon = 0$. For metals, this is caused by the electron oscillations and the corresponding frequency is called plasma frequency ω_p. For polar dielectrics, phonon resonances can also cause epsion-near-zero region, which corresponds to the so-called Reststrahlen band [127]. Here, artificial material with fixed $n_r = 3$ is chosen, the corresponding weighting functions for varying k values are calculated and plotted in Figure 14. Blue curve corresponds to $k = 0$, where two resonance peaks at the location of λ and λ/n exist in the curve as discussed above. As k increases, penetrated beams to the material experience energy absorption, providing extra phase and momentum change of optical beams, therefore, the second resonance peak which corresponds to the light wavelength inside the material decreases and disappears. Due to the absorption and reemission, reflected beams experience more complicated phase change compared to pure dielectrics with $k = 0$. As k increases and gets larger than n_r, ϵ becomes negative. Surface behaves like perfect electrical conductor with high reflectivity, the influence from surface roughness under this condition is also relatively small. Weighting function shows as one sharp peak at the incident λ.

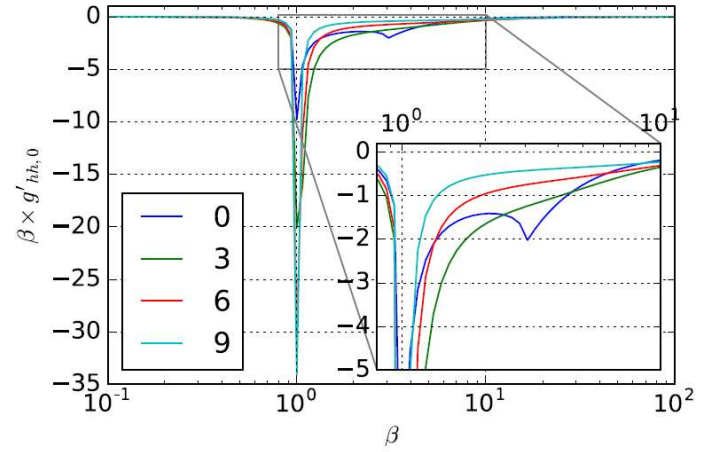

Figure 14: 0th order weighting function magnitude with respect to dielectric constant for materials with n_r=3. The legend in the figure shows the corresponding k value for each curve. Inset plot corresponds to the boxed region.

Considering function $C(\beta)$, the maximum magnitude happens at $\frac{\partial C}{\partial \beta} = 0$, where $\frac{2\sqrt{2}}{k_0 l} = \frac{\sqrt{2}}{\pi}\frac{\lambda_0}{l}$, and the maximum value

$$C_{max} = \frac{16}{\pi e^2}(\frac{\sigma}{l})^2 \tag{28}$$

Thus, the maximum value of C for Gaussian surfaces is proportional to $(\frac{\sigma}{l})^2$. In Figure 15, we plotted four C functions with the transverse correlation lengths chosen to be $\lambda/10, \lambda/5, \lambda/2.5, \lambda$ respectively. For all these curves, $\sigma = l/5$. σ/l are kept to be the same thus the C curves have the same maximum values according to equation 28. σ/l shows the general slope of the surface roughness, for SPM/SSA method to be valid, σ/l to be smaller than 4 are necessary. As illustrated in Fig. 15 the peak positions of function C moves to the smaller length scales section as l gets smaller. At the location $\beta = 1$, which is the resonance position for weighting functions, maximum C happens at $l/\lambda_0 = \pi/\sqrt{2} \approx 2.22$. Due to the fast fall off of weighting functions, when $l = \lambda_0$(Cyan curve in fig. 15), panel (b), overlap between the function C and weighing function becomes too small, the reflection change caused by the roughness can be neglected. In other words, the roughness length scale is too big for the incident light to detect and the reflection value is close to smooth flat surface.

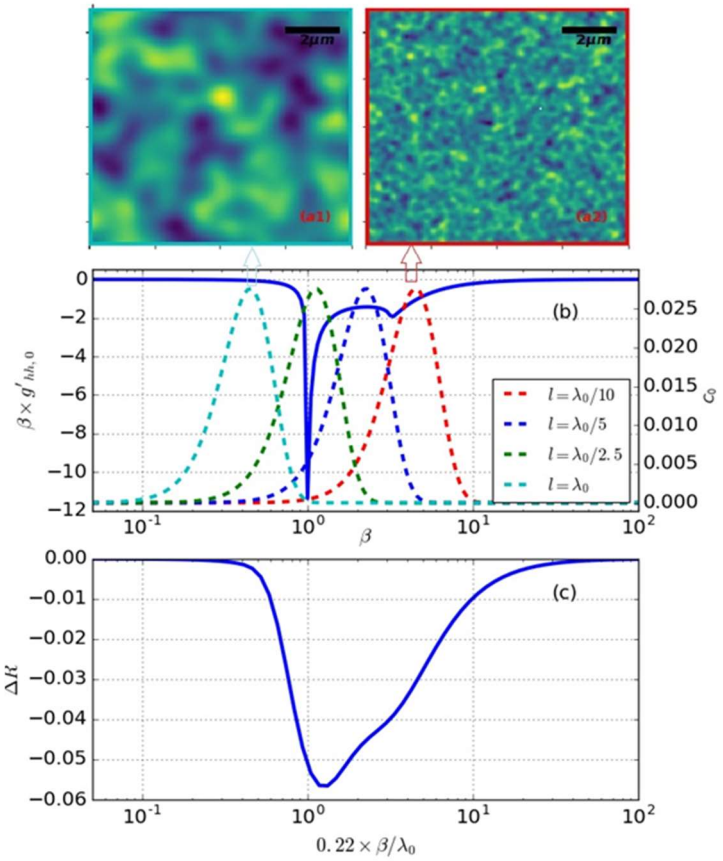

Figure 15: Illustration of C_0 functions for Gaussian surfaces overlapped with the weighting function and corresponding surface profile. Top panels a(1),a(2) show two example surface height profiles. Panel (b) shows weighting function with four C_0 functions. Pan

When l gets smaller than λ_0, weighting functions doesn't fall as fast, maximum overlap between these two function happens when l is in between λ/n and $\lambda/2.22$. Panel (c) in Fig. 15 plotted the reflection change for Gaussian surfaces with different correlation lengths. The x-axis is the correlation length l in the unit of $\lambda/2.22$, in other words, the location of C_{max} for surface curves. As illustrated, the maximum ΔR happens with the maximum overlap between the surface C function and the weighting function, which is in between λ/n and $\lambda/2.22$. Two example surface height profiles are shown in Fig. 15, panel (a). At the left profile, panel $a(1)$, $l = \lambda/2.5 = 600nm$, and for the right profile $l = \lambda/10 = 150nm$. The C function for these two surface profiles are the dotted green and dotted red curve respectively. As stated previously, σ/l are kept the same for these illustrations, therefore, smaller l corresponds to smaller defects.

After a brief discussion on the weighting function and the correlation functions, we will next discuss the surface roughness effects for refractory metals and polar dielectrics, which are popular materials for high temperature applications. Here, we chose Tungsten and SiC as two examples and analyzed the surface reflection change caused by random surface roughness.

Similar to other refractory metals, W shows a high reflection at far-infrared range, while it experiences a considerable absorption in the visible and near-infrared. We pick four wavelengths, $500nm, 1000nm, 1500nm, 2000nm$, respectively. We calculated the corresponding weighting functions, which are plotted in the top panel of Fig. 16. With reference to the middle panel of Fig. 16, at $\lambda = 500nm$, $n > k$, $\epsilon > 0$; at $\lambda = 1000nm$, n gets smaller compared to 500nm, k is bigger and ϵ gets close to 0. As can be seen from the second panel, the weighting function for $\lambda = 500nm, 1000nm$ is very close in magnitude. At $\lambda = 1500nm$, the magnitude of the weighting function starts to get smaller especially when β gets away from the incident wavelength resonance location. At $\lambda = 2000nm$, ϵ gets far negative, where weighting function gets a lot smaller in magnitude compared to the previous 3 wavelengths. Since the maximum reflection change point is closely correlated with the incident λ, if we look at the problem from the broadband spectrum point, for a fixed topology of surface roughness, its influence on the spectrum will mainly be around the $l/2.22$ location. Keeping this idea in mind, the broadband spectrum for W Gaussian surfaces are calculated and plotted in the bottom panel. Legend in the panel shows the maximum location of the chosen C function, in other words, $l/2.22$. For the first three curves, $l/2.22 = 500nm, 1000nm, 1500nm$, The maximum ΔR value location is around the corresponding wavelengths. For all these curves, σ/l are kept the same for each surface profile, therefore, σ will be larger for bigger l curves. It shows in the curve that the ΔR values smooth out at longer wavelengths. This confirms that when the surface roughness size is very small compared to λ, ΔR depends only on the value of σ [60]. For the red curve, where C_{max} location at $2000nm$, it is expected that one resonance peak would show around $\lambda = 2000nm$, however, the resonance peak actually appears at around $\lambda = 1500nm$, which is a big resonance shift. Going back to the first three curves, we could see that there are also shoulder peaks at around $\lambda = 1500nm$. Refer to the top panel in this figure, for Tungsten, epsilon becomes negative at around $\lambda > 1000nm$, where surface plasmons resonances(SPR) can be excited. The localized surface plasmons resonance will increase the absorption of the material thus shows as a higher reflection reduction. Gaussian surfaces with one certain transverse correlation length can be decomposed into sinusoidal surfaces with the corresponding periodicity. As the corresponded periodicities for Gaussian surface covers one certain range centered around l, shown as the C function in Fig. 16, if l is around ω_p, LSPR gets excited and increases absorption. At C_{max} location at $2000nm$, the weighting function for

$\lambda = 2000nm$ is relatively small due to the high negative number of ϵ, the resonance peak matching the periodicity doesn't gets as high as LSPR peak, thus showing as resonance shift on the reflection spectrum. As l gets larger and further away from the ω_p frequency, corresponded LSPR resonance also gets lower due to the magnitude of C function at this resonance frequency gets lower. The LSPR resonance peak can still be seen at $C_{max} = 2500nm$, but disappears at $C_{max} = 3000nm$. At these larger ls, the primary resonance peak is also not as sharp and it falls very fast to one smooth value.

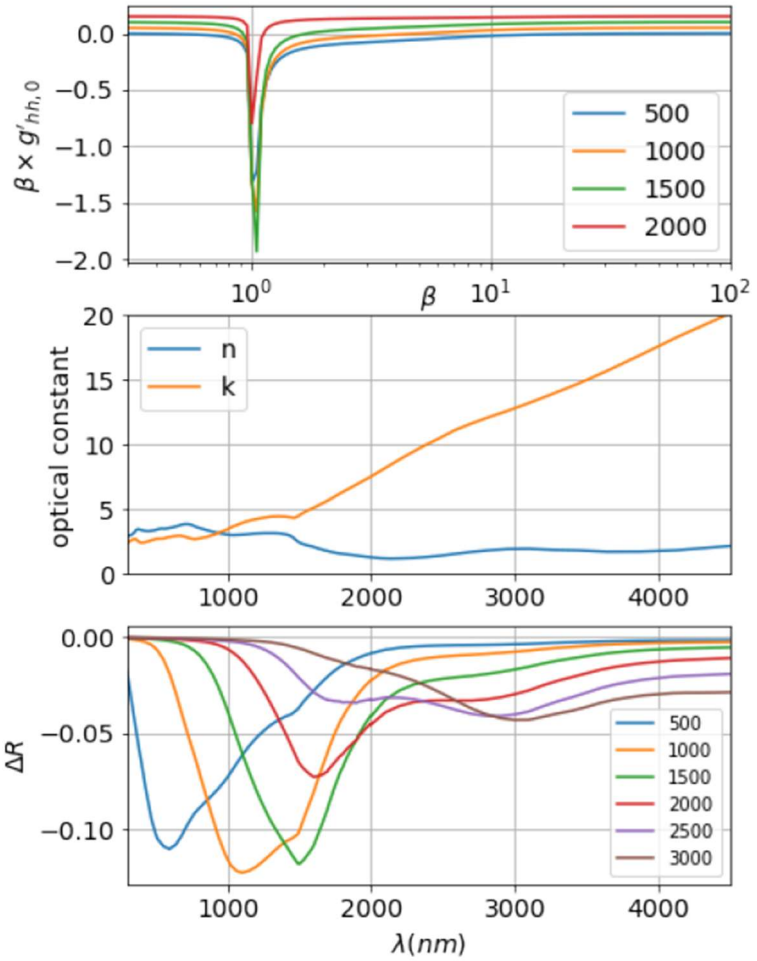

Figure 16: Random roughness effects on Tungsten surface. Top panel: weighting function for wavelengths λ=500nm,1000nm,1500nm,2000nm. Middle panel: optical dielectric constants for W at the visible and near-infrared range. Bottom panel: Reflection spectrum change

Similar analysis is performed for SiC. Fig. 17 illustrates the optical constant, weighting function for selected wavelengths, as well as the broadband reflection change for fixed Gaussian surface topologies. SiC is a lossy dielectric in infrared range. Incident beams penetrates dielectrics thus resulting low reflection. Four wavelengths $\lambda = 410$ nm, 1500 nm, 11700 nm, 24900 nm were chosen to illustrate the weighting functions respectively, shown in top panel of Fig. 17. Compared to W, the magnitude of weighing functions are smaller. As the magnitude of weighting function of W gets up to -20, the magnitude for SiC goes only to -1. Even n values for W and SiC

are comparable, there is significant difference in k values. Lower k values for SiC means lower absorption for penetrated beams propagating inside the material. As seen in the top panel, the secondary resonance peak shows for the chosen wavelengths. As the differences among the weighting functions are relatively small, roughness caused reflection change are also highly depended on the ration of l/λ, with σ/l fixed. The results are shown in panel 3. As expected, at the long wavelength range, surface reflection change goes up as σ goes up. The maximum reflection change occurs when maximum overlap of Gaussian surface C function and weighting function, which is when the C_{max} locates at $\lambda/2.22$. Further than that, it can be seen that there is one secondary resonance peak around the location of λ in between 10000 nm and 15000 nm, where the lattice oscillations cause extra absorption. These lattice polar resonances behaves like Lorentz oscillators for polar dielectric crystals, and the dispersion relation are similar to those of metals. Referring to middle panel, which illustrates the optical constant of SiC, we can clearly see that there is one resonance peak at $\lambda \approx 10\mu$m - 15μm. For some polar dielectrics, such as 4H-SiC, surface phonon resonance (SPhR) modes can be excited during the Reststrahlen band, where results epsilon near to zero and negative $Re(\epsilon)$. According to our previous discussion, the surface roughness for these materials will be expected to experience some higher reflection change at the resonant frequency location.

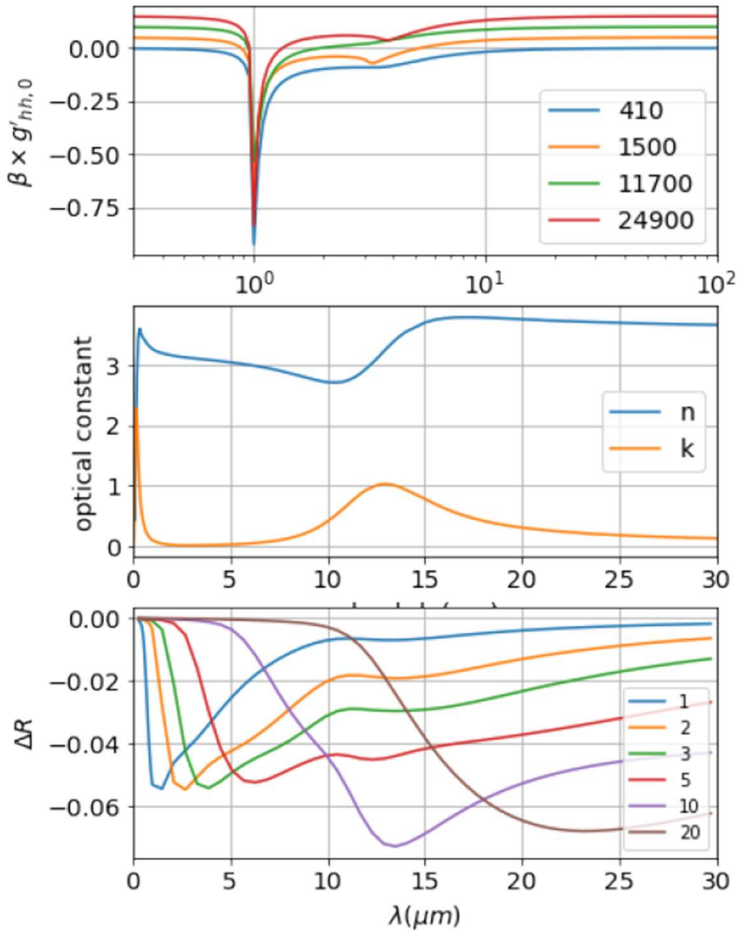

Figure 17: Random roughness effects on SiC surface. Top panel: weighting function for wavelengths λ=410nm,1500nm,11700nm,24900nm. Middle panel: optical dielectric constants for SiC at the visible and near-infrared range. Bottom panel: Reflection spectrum change

After this detailed discussion on various materials, the main findings and differences of each case can be summarized as follows: For lossless case, weighting function has two resonance peaks, corresponding to the incident wavelength and wavelength of beam inside the material, however the magnitude of weighting functions are limited compared to lossy materials. For the lossy materials that we studied, a comparison of W and SiC suggests that SiC is more dielectric as n>k for interested spectrum range for SiC(400nm-2um), thus for the same σ, which is height variance, roughness causes bigger reflection change for W, especially at the near-infrared range, where epsilon of W is close to 0. For SiC, roughness caused spectrum change can show the magnification in the 10 um to 15um range, which corresponds to the phonon resonance in SiC, however, due to SiC is still dielectric at this range, the magnification is limited.

3.2. Origins of the Enhanced Broadband Absorption in Black Silicon

First, random textures with varying *l* and *h* are formed with p = 4 μm for which geometries are depicted in Fig. 18 and spectral absorption of those geometries are shown in Fig. 19(a). Doping concentration of silicon is fixed to 10^{14} cm^{-3}, for which calculation of the corresponding optical properties are described in previous sections. As seen in Fig. 19(a), for doping concentration of 10^{14} cm^{-3} near unity absorption is observed in 0.3 – 1 μm spectrum interval for varying correlation lengths and RMS heights when p =4 μm. However, high absorptance is decreased to 30 % at longer wavelengths and approach to absorption of smooth film. Such difference over the spectra is attributed to dispersion in optical conductivity where $\sigma(\lambda=1\ \mu m) \approx 10^{14}$ and $\sigma(\lambda=2\ \mu m) \approx 10^{13}$. $|E(\lambda=0.5\ \mu m)|^2$ distributions over the film and texture with $l = 0.2\ \mu m$, $h = 0.6\ \mu m$, geometry depicted in Fig. 18(a), are shown in Fig. 19(b) and 19(c) respectively. As shown in Fig. 19(b), uniform distribution of the fields inside the Si is observed when the surface is smooth. Unreflected fields penetrate to the silicon and physical phenomena at the interface can be explained by Fresnel reflections. However, in the case of textured surface, high field enhancements localized near the edges of the individual pyramid-like textures, are observed as shown in Fig. 19(c), which are called as side modes throughout the manuscript. As seen, those side modes give rise to higher fields inside the Si spikes, thus lead to elevated absorption. Similar side modes are also observed at different wavelengths in 0.3-3 μm interval. It indicates that such side modes occur in broadband spectrum when the Si surface is textured and responsible from broadband absorption enhancement. To explore the effect of roughness dimensions on the absorption, field distributions are also analyzed for the geometry depicted in Fig. 18(b), which has less peaks and dips in the geometry due to the increased correlation length. In other words, texture in Fig. 18(a) has more spikes with small widths, whereas texture in Fig. 18(b) has less spikes with wider widths.

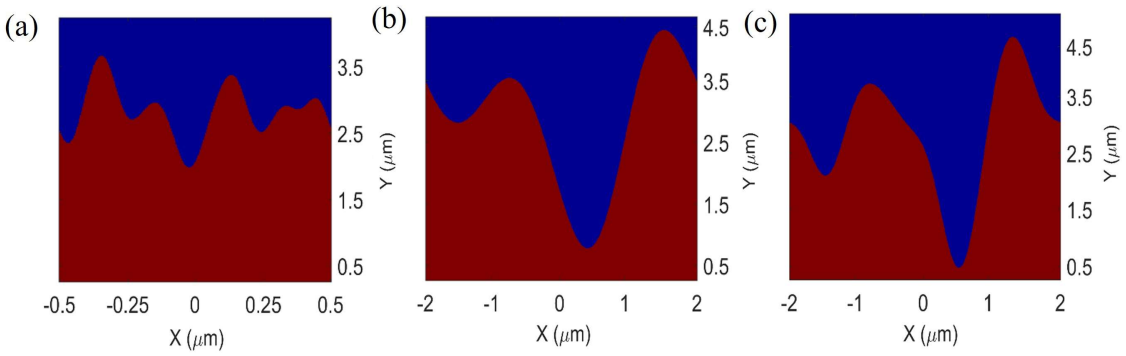

Figure 18: a) An example random texture generated by setting l =0.1 μm, hrms =0.3 μm, p = 1 μm. b) An example random texture generated by setting l =1.1 μm, hrms =0.8 μm, p = 4 μm. c) An example random texture generated by setting l =0.6 μm, hrms =0.8 μm, p = 4 μ

Although no significant difference between textures with varying *l* and *h* are observed at longer wavelengths, slight decrease in absorption in visible spectrum is observed for increased *l*. To analyze, $|E(\lambda=0.5\ \mu m)|^2$ distribution for the texture with $l = 1.1\ \mu m$, $h = 0.8\ \mu m$ is shown in Fig. 19(d). As seen in Fig. 19(d), side modes also occur in this texture with slightly reduced field intensities inside the spikes. It shows that field enhancement by the side modes are dependent on the width of the individual pyramids. Increased widths lead to reduced intensity, thus resulting in decreased absorption. Effect of doping concentration on the spectral distribution and corresponding spatial absorption profiles for doping concentrations of 10^{14} and $5x10^{15}$ cm^{-3} are also shown in Fig. 20. As shown in Fig. 20(a), spectral absorption is significantly enhanced with increased doping concentration especially at longer wavelengths. $|E(\lambda)|^2 x\sigma(\lambda)$ distributions given in Fig. 20(b) and 20(c) for N =10^{14} and $5x10^{15}$ cm^{-3} also shows that spatial distribution profile inside the texture is not significantly altered by *N*.

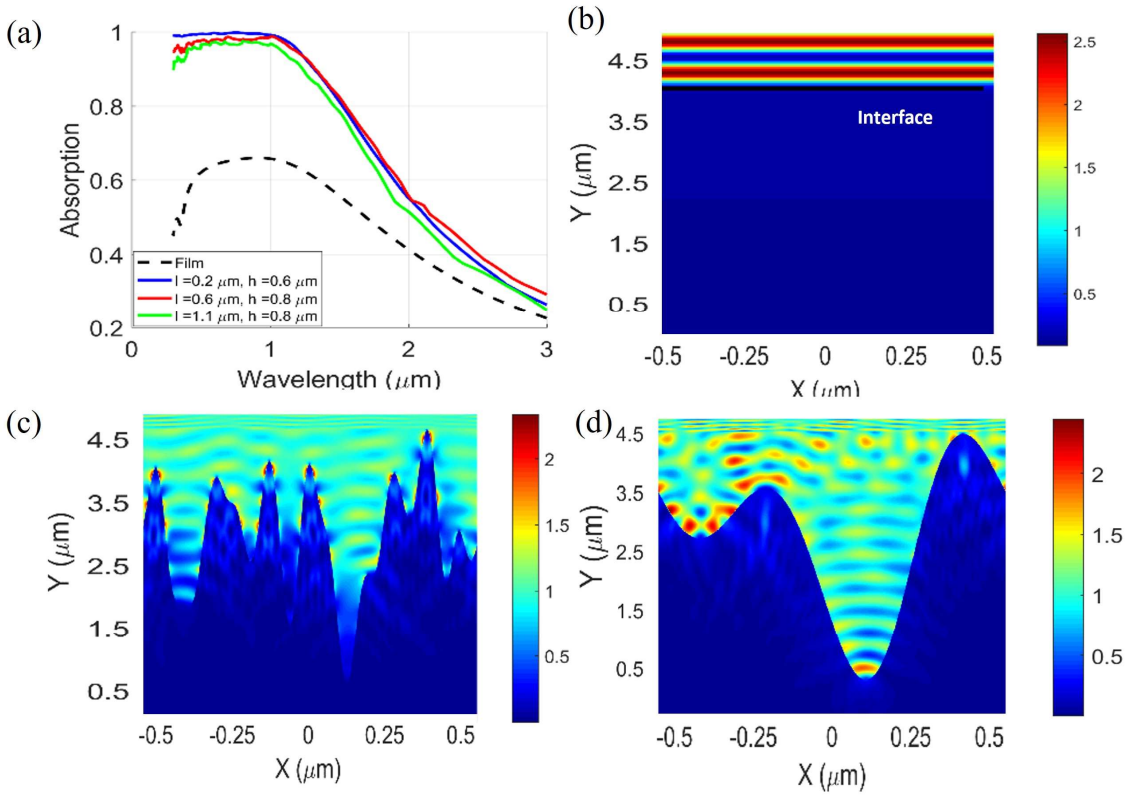

Figure 19: a) Comparison of spectral absorption of untextured (film) and textures silicon with varying l and h_{rms}. b) $|E(\lambda)|^2$ distribution of untextured Si. c) $|E(\lambda)|^2$ distribution of textured silicon with l =0.1 μm and h_{rms} =0.3 μm. d) $|E(\lambda=0.5\ \mu m)|^2$ distribution of the texture with l =1.1 μm , h_{rms} =0.8 μm at λ =0.5 μm.

However, differently from N =10^{14} cm^{-3} case, fields absorbed more on the upper segment of the texture due to increased ε''(λ), therefore σ(λ), when N is set to 5x10^{15} cm^{-3}. Finally, spectral absorption of a random texture is compared to deterministic textures with varying periodicities in Fig. 20(d). $|E(\lambda=0.5\ \mu m)|^2$ is also depicted in Fig. 20(e).

Results depicted in Fig. 20(a) shows that spectral absorption of the random textures are very similar to previously reported experimental results [13,15]. Also, absorption of deterministic textures is similar to random textures' and are not very sensitive to periodicity in 0.3-3 μm spectrum, except the visible spectrum. Similar change in the visible spectra is also reported for random textures and attributed to reduced field intensity when texture widths are increased. In addition, field distribution for the deterministic texture with p =1 μm shown in Fig. 20(e) shows that side modes are also supported in deterministic textures. such similarity in absorption spectrum and field distributions allow us to use deterministic textures to understand underlying mechanisms in textured silicon. For analysis, deterministic textures with varying dimensions in broadband spectrum are analyzed.

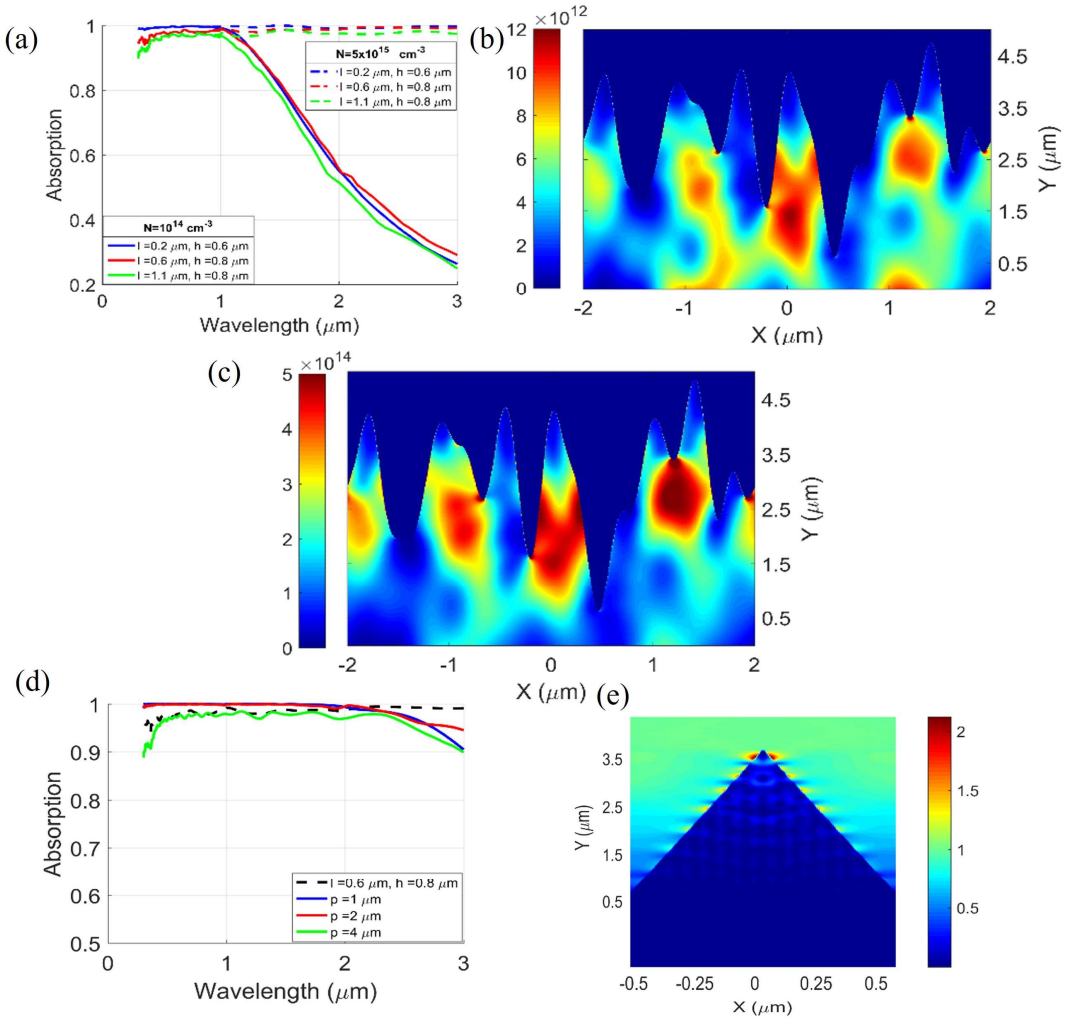

Figure 20: a) Spectral absorptions of random textures for N =10^{14} and 5x10^{15} cm^{-3}. b-c) Spatial absorption profiles for N =10^{14} and 5x10^{15} cm^{-3} at λ=0.5 μm. d) Absorption of a random texture and deterministic texture with varying p for N =5x10^{15} cm^{-3}. e) $|E(\lambda=0.5\ \mu m)|^2$ distribution for the deterministic texture with p =1 μm.

In the light of reported results until this point, it is found out that high absorption in broadband spectrum stem from local field enhancements which occur near the edges of the features. Both in random and periodic textures, such side modes are observed. Analysis reveals that field intensity of the side modes are dependent on the width of the individual spikes and are reduced with increased width. This led to reduction in the absorptance percentage of the periodic textures compared to random textures due to the presence of a single structure with larger width. Source of the observed variations is discussed in the following parts together with the driving mechanisms for the fields. Spatial absorption profiles inside the silicon are found to be insensitive to doping concentration. Finally, it is shown that deterministic textures exhibit similar absorption characteristics compared to random textures.

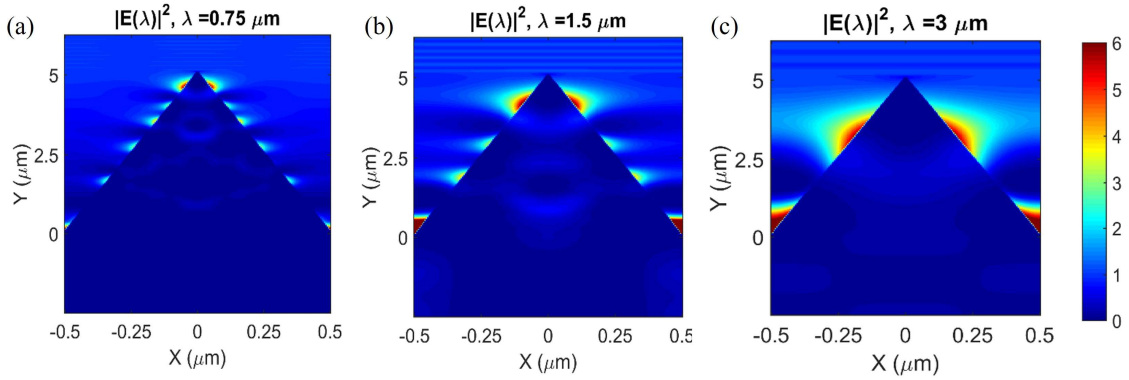

Figure 21: a-b-c) $|E(\lambda)|^2$ at wavelengths of 0.75, 1.5 and 3 μm for the pyramid dimensions of p =1 μm, h =3 μm and carrier concentration of 10^{14} cm^{-3}

To study the underlying mechanism that give rise to side modes, further analysis is carried out with deterministic textures. Deterministic textures are chosen to avoid interference effects in random textures therefore, to be able to characterize the side modes occurring in individual features. $|E(\lambda)|^2$ and $|E(\lambda)|^2 \times \sigma(\lambda)$ distributions over the deterministic textures are considered for the analysis. In Fig. 21, $|E(\lambda)|^2$ for $\lambda = 0.75$ μm, $\lambda = 1.5$ μm and $\lambda = 3$ μm is demonstrated. *p* and *h* of the pyramid are set to 1 μm and 3 μm respectively and *N* is set to 10^{14} cm^{-3}. As seen, distinct local field enhancements on the edges of the pyramid are observed. At each wavelength, highest field intensities are obtained near the top of the pyramid. However, number of local field enhancements on the edges of pyramid differ for each wavelength. Those distinctive regions also exist inside the pyramid, as shown in $|E(\lambda)|^2 \times \sigma(\lambda)$distributions depicted in Fig. 10 for selected wavelengths.

As shown in Fig. 22, highest absorption inside the pyramid occurs at the region where side mode with highest intensity penetrates the structure. Field distribution due to this mode, thus the absorption, inside the pyramid is similar for the selected wavelengths. Results depicted in Fig. 21 and 22 shows that these textures support resonance modes at different wavelength and resonance conditions are satisfied throughout the geometry multiple times. To analyze, previously reported study regarding to resonance mechanisms in a trapezoid geometry is considered.

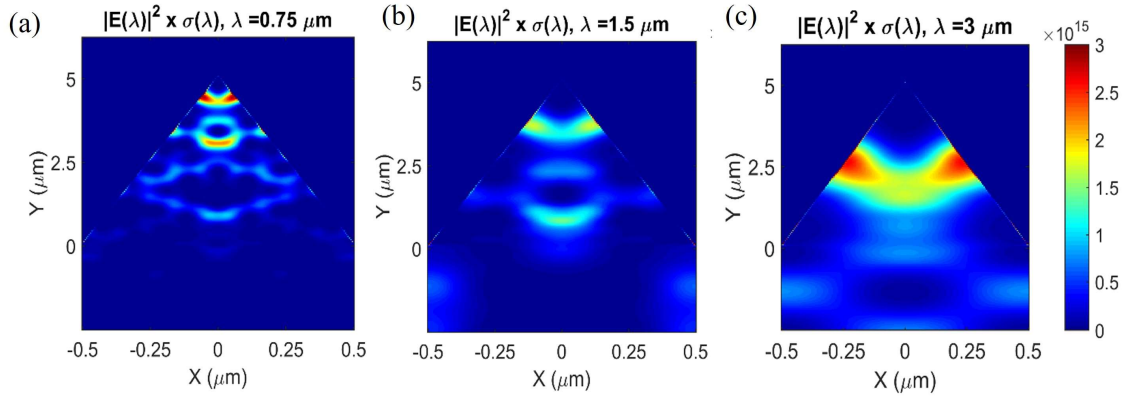

Figure 22: a-b-c) $|E(\lambda)|^2 \times \sigma(\lambda)$ at wavelengths of 0.75, 1.5 and 3 μm for the pyramid dimensions of p =1 μm, h =3 μm and carrier concentration of 10^{14} cm^{-3}.

In the literature, such position dependent local field enhancements are reported for trapezoidal metal-insulator-metal (MIM) ultra-thin broadband resonators [128]. In [128], it is shown that strong and broadband field enhancement is achieved by exciting multiple resonance modes in different regions of the trapezoidal structure. Similarly, silicon pyramid can support multiple resonance modes due to its trapezoidal geometry and give rise to high field enhancements inside which are absorbed due to the broadband loss introduced in the silicon with doping. Those resonance modes also give rise to strong fields in the silicon air interface on the sides of the pyramid. Resonance condition for different wavelengths is dependent on -Z direction. Position of the resonance mode with the highest intensity shifts towards to the bottom of the pyramid for increasing wavelength. It indicates that higher pyramid width is required to achieve increased coupling with the structure for longer wavelengths. It is also observed that those modes are repeated throughout the pyramid in -Z direction. To estimate the resonance condition in the pyramid, an effective wavelength method derived for optical antennas is used here.

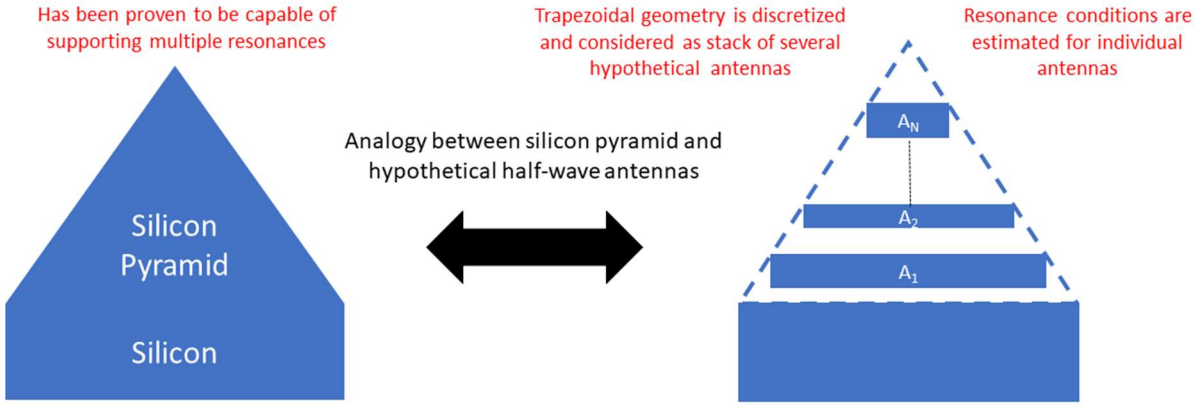

Figure 23:Scheme for analogy between silicon pyramid and stacked half-wave antennas

It is known that coupling condition for RF and microwave antennas are strongly correlated with the length of the antenna, e.g. it is $L = (1/2)\lambda$ [129] for half-wave antennas. Such relationship fails in optical frequencies due to the penetration of the incident wave into the structure and interaction of it with the electron oscillations, whereas structures are nearly perfect conductors in microwave and RF applications, thus penetration does not occur. By considering this difference, an effective wavelength, λ_{eff}, calculation formula is derived in [67] which yields an λ_{eff} inside the antenna that can be used to tune the L. By utilizing this theory, required width for the resonance at a specific wavelength inside the silicon pyramid is estimated. To apply such analysis, pyramidal geometry is treated as a combination of several half-wave antennas which resonate at different wavelengths. Scheme for such representation is depicted in Fig 23. λ_{eff} calculation is described in detail in [130] and final formula for λ_{eff} is given in Eq. (29),

$$\lambda_{Eff} = \frac{\lambda}{\sqrt{\varepsilon_s}} \sqrt{\frac{4\pi^2 \varepsilon_s (\frac{R^2}{\lambda^2}) \tilde{z}(\lambda)^2}{1+4\pi^2 \varepsilon_s (\frac{R^2}{\lambda^2}) \tilde{z}(\lambda)^2}} \tag{29}$$

where λ is the incident wavelength, ε_s is the permittivity of the incident medium, R is the thickness of the antenna and $\tilde{z}$ is an intermediate variable. Based on this formula, L for the

resonance to occur is obtained as $\lambda_{eff}/2$ for a half-wave antenna. To create an analogy between half-wave antennas and silicon pyramids, L is treated as width of the pyramid where a side mode occurs. Therefore, side modes are attributed to half-wave antennas and when stacked together in trapezoidal fashion, multiple resonance modes at different wavelengths are supported.

Effective wavelength calculation with Eq. (29) is carried out for the selected wavelengths, $\lambda_1 = 0.5$ µm, $\lambda_2 = 1.5$ µm and $\lambda_3 = 3$ µm. Hypothetical half-wave antenna with dimensions is schematized on the pyramid and field distribution at λ_3 is shown in Fig. 24(a). In this case, effective wavelength of 0.7 µm is obtained, with R =0.13 µm, from Eq. (29), thus L = 0.35 µm, which is equal to the width of the pyramid at the location where resonance mode is occurred as shown in Fig. 21(c). Smaller effective wavelengths are achieved for wavelengths of λ_1 and λ_2, for which field distributions are also shown in Fig. 21. To analyze the dependency of L on R, L values are calculated for varying R values. To satisfy the $R << \lambda$ requirement for Eq. (29) to be valid, R values between $\lambda/20$ and $\lambda/50$ are considered and maximum errors are demonstrated in Fig. 24(b) for wavelengths of λ_1, λ_2 and λ_3.

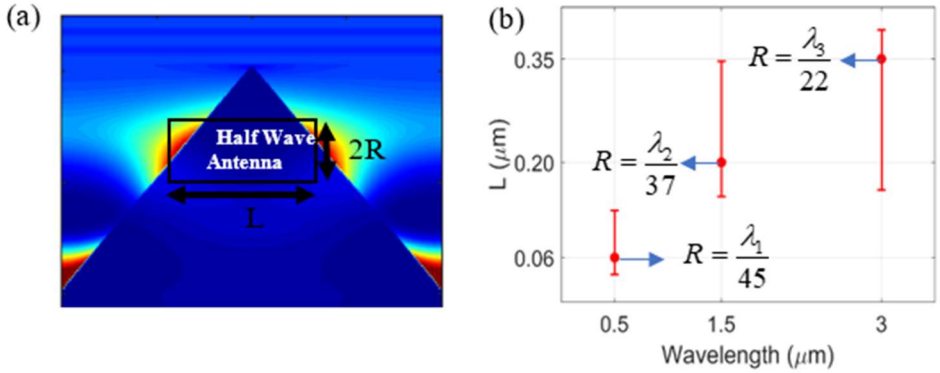

Figure 24: a) Representation of individual half-wave antenna with thickness 2R and length L, on the pyramid silicon. b) Calculated resonance condition for varying R values and corresponding L values. Lower and upper bounds of the error bars stand for R= λ/50 and λ/20. L = $\lambda_{Eff}/2$ values are obtained at R =$\lambda_1/45$, R =$\lambda_2/37$ and R =$\lambda_3/22$ which is equal to the width of the pyramid where first side mode occurs.

As seen from Fig. 24(b), maximum errors are 0.07, 0.15 and 0.18 µm which corresponds to $\lambda_1/7$, $\lambda_2/10$ and $\lambda_3/15$ for wavelengths of λ_1, λ_2 and λ_3. Estimation accuracy is increased with higher *'R'* at longer wavelengths which indicates that fields are less confined in the geometry for longer wavelengths. Such variations in confinement also shown in Fig. 21. Calculated effective wavelengths for the given dimensions of *'L'* and *'R'* shows that absorption occurs in very small dimensions compared to overall size. This also explains the high absorption at different periodicities which controls the width of the pyramids. Since sufficient width for effective wavelength matching condition is satisfied for p =1, 2 and 4 µm, high fields, thus absorption, inside the pyramids are achieved. As shown in the field distribution results, these absorptance modes are repeated throughout the geometry. This repetition is attributed to similar resonance condition, which occurs due to the scaling of effective wavelength obtained from Eq. (29). In other words, effective wavelength matching conditions are satisfied when the width of the pyramid is extended. Similar behavior is also observed for increased pyramid heights. Higher heights only lead to increased number of side modes, which do not alter the absorptance in broadband. This also

indicates that, matching condition is highly dependent on width of the pyramid. As a next step, effects of periodicity of the pyramids, therefore the texture widths, on the field distributions and absorption are investigated.

$|E(\lambda)|^2$ distributions depicted in Fig. 25(a), (b) and (c) shows that number of side modes at 3 μm is increased with increasing periodicity. These results indicate that coupling condition inside the pyramid is repeated and it is linked to the periodicity, thus the width of the pyramid. However, different trends are observed in the fields inside the pyramid. In Fig. 25(d), a single distinctive high absorption zone is observed inside the pyramid which is linked to side mode shown in Fig. 25(a). The highest absorptance zone is shifted towards to the bottom of the pyramid and exhibits a different kind of $|E(\lambda)|^2 \, x \, \sigma(\lambda)$ distribution when p is increased to 2 μm.

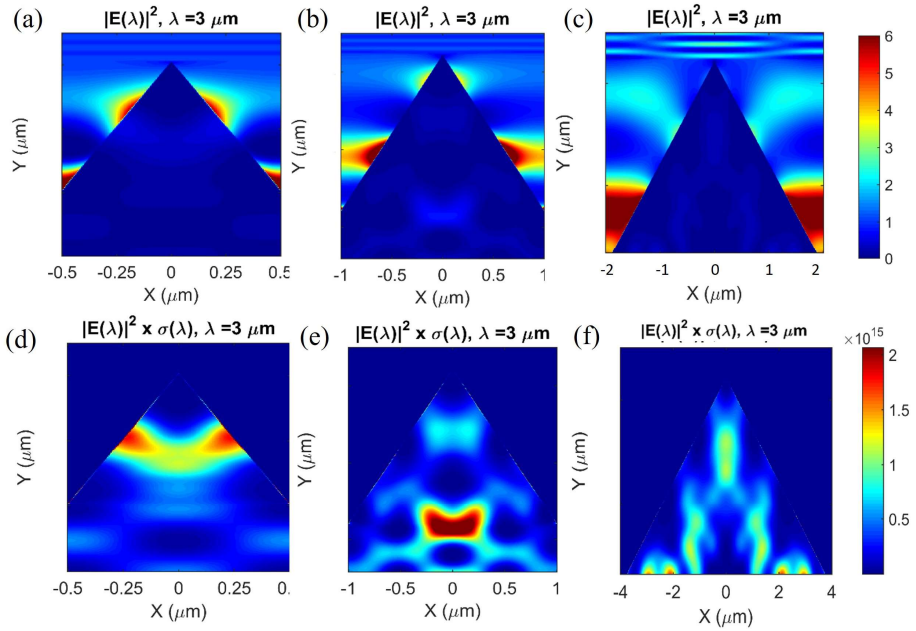

Figure 25: a-b-c) $|E(\lambda)|^2$ distributions at λ =3 μm wavelength for p =1 μm, 2 μm and 4 μm respectively. d-e-f) $|E(\lambda)|^2$ x σ(λ) distributions at λ =3 μm wavelength for p =1 μm, 2 μm and 4 μm respectively.

The highest absorptance zone in Fig. 25(d) is occurred due to the side modes and a continuous trend between the fields inside and outside of the pyramid is observed. However, a continuous trend is not observed between the highest $|E(\lambda)|^2 \, x \, \sigma(\lambda)$ region inside the pyramid and side modes shown in Fig. 25(e) and 25(b) respectively.

A different behavior from these is observed when p =4 μm. As seen in Fig. 25(f), multiple high $|E(\lambda)|^2 \, x \, \sigma(\lambda)$ zones are occurred, and they are extended in -Z direction like propagating modes. $|E(\lambda)|^2 \, x \, \sigma(\lambda)$ in Fig. 25(e) and 25(f) indicates that absorptance enhancement inside the pyramids in these geometries does not only stem from effective wavelength matching condition. Although resonance conditions in the pyramid is satisfied as shown in Fig. 25(b) and 25(c), another phenomenon occurs in these geometries which induces fields that interfere with the resonances. Therefore, distinctive $|E(\lambda)|^2 \, x \, \sigma(\lambda)$ region in Fig. 25(e) is attributed to the interference of the fields induced by multiple electromagnetic phenomena occurring in the geometry. Finally, results depicted in Fig. 25(f) shows that field enhancement in the geometry is dominated by this second

electromagnetic phenomenon which give rise to field enhancements extended in -Z direction and suppresses the fields induced by effective wavelength matching.

It is observed that these pyramids resemble the waveguide geometries that are composed of a high index core surrounded by a low index cladding which supports certain TM modes. In this configuration, silicon acts as high index core and air is the low index cladding material as depicted in Fig. 26(a). Due to the tapered geometry, broadband spectrum of wavelengths is supported throughout the geometry and response is analogous to tapered fibers [131]. In tapered fibers, modes with longer wavelengths start to cut-off as the width of the fiber shrinks. In the textured silicon geometries, modes with longer wavelengths start to occur as width of the pyramid increases.

Therefore, two problems are analogous and similar analysis is adapted based on the reciprocity of the Maxwell's equations. Assuming tapered geometry is composed of rectangular segments for which supported TM modes' cut-off wavelengths are estimated by,

$$k_{cut} = \frac{m\pi}{d\sqrt{1-\frac{\mu_1\varepsilon_1}{\mu_0\varepsilon_0}}} \tag{30}$$

and dispersion diagrams are obtained by the following expressions:

$$\begin{Bmatrix} tan(k_x d) \\ -cot(k_x d) \end{Bmatrix} = \sqrt{\frac{w^2\mu_0(\varepsilon_1-\varepsilon_0)d^2}{(k_x d)^2} - 1} \tag{31}$$

$$k_z = \sqrt{w^2\mu_0\varepsilon_1 - k_x^2} \tag{32}$$

With the aid of dispersion diagrams, which modes are supported at certain parts of the tapered geometry is estimated. Based on these formulas, dispersion diagrams for different core widths, which corresponds to width of the silicon pyramid. Diagrams for *d=0.06* μm, *d=0.2* μm and *d=0.35* μm, at which effective wavelength matching is achieved, are obtained and shown in Fig. 26.

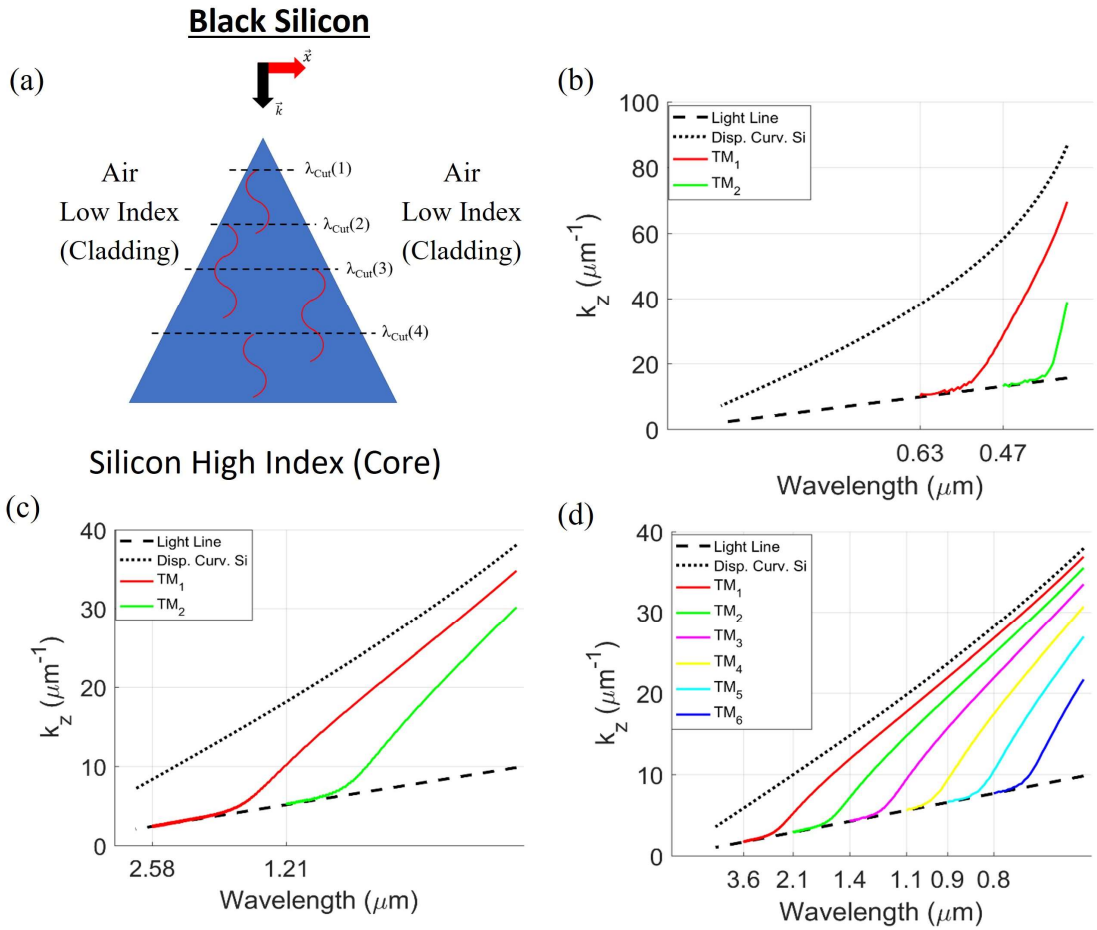

Figure 26: a) Scheme for the black silicon as a waveguide problem composed of high index (core) and low index (cladding). b-c-d) Dispersion diagrams for d =0.06, 0.2 and 0.35 μm at which effective wavelength matching condition is satisfied for wavelengths of 0.5, 1.5 and 3 μm wavelengths.

As seen in Fig. 26(b), 26(c) and 26(d) respectively, only TM_1 modes exist with a very small wavevector (near cut-off wavelength), for wavelengths of 0.5 μm, 1.5 μm and 3 μm when *d* is set to 0.06 μm, 0.2 μm and 0.35 μm. This indicates that fields formed due to the effective wavelength matching in these segments do not strongly interfere with TM modes. Therefore, *E* fields smoothly travels throughout the pyramid in -X direction and continuous trends are observed. However, this is only valid for the top side mode.

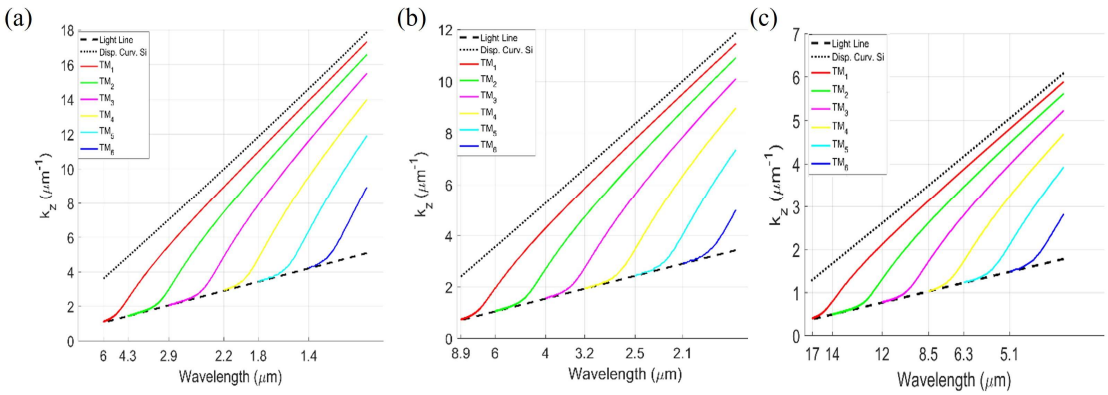

Figure 27: a-b-c) Dispersion diagrams for d =0.7, 1 and 2 μm and supported TM modes with cut-off wavelengths labeled.

Although modes that exist when *d =0.2* μm or *d=0.35* μm do not have high wavevectors at longer wavelengths, it is not the case for shorter wavelengths. As seen in Fig. 26(c) and 26(d), number of modes and magnitude of the existing modes' wavevectors are increased at shorter wavelengths. This indicates that TM modes at shorter wavelengths start to interfere with fields induced by effective wavelength matching when width is around 0.2 μm. Such interference lead to reduction in absorption in the visible spectrum for the rough surfaces with increased correlation lengths. Since width of the individual spikes are increased with increasing correlation lengths, TM modes start to form in the textures and reduction in absorption in shorter wavelengths are observed. To further analyze the effect of texture width, *d*, modes in the structures with higher periodicities are analyzed.

As periodicity increased, maximum width of the silicon pyramid is also increased, and multiple effective wavelength matching conditions occur throughout the geometry as shown in Fig. 25(b). Increase in maximum possible width also allows the pyramid support other TM modes which have longer cut-off wavelengths. To show this, dispersion diagrams with *d = 0.7* μm, *1* μm and 2 μm is demonstrated in Fig. 27. As shown in Fig. 27, with increasing *d,* number of TM modes increase and wavevector of the existing modes, e.g. TM_1, is increased. Therefore, at wider widths, contributions from TM modes to electric fields are increased. This leads to significant changes in field distributions and reduction in absorption which becomes more dominant at shorter wavelengths. This finding also explains the reduction in absorptance at longer wavelengths in periodic textures compared to deterministic textures, which was attributed to presence of a single texture with higher width. Due to the stronger interference of the waveguide modes with the fields induced by effective wavelength matching at higher widths, reductions in absorptance spectra of random textures compared to deterministic ones are observed.

Demonstrated dispersion diagrams indicate that waveguide modes are started to be supported at widths larger than 50 nm and their contributions become more distinguishable at larger widths. Their contributions are observed in spatial absorptance profiles depicted in Fig. 22 and 25(d-f), which shows that these two separate phenomena coexist in broadband spectrum at these geometries. In summary, our analysis regarding to supported TM modes reveal that these modes have significant effect on the field distribution inside the pyramid. It is shown that TM modes becomes dominant in broadband with increased periodicity of the pyramids and compensates the

effect fields induced due to the effective wavelength matching throughout the geometry. In other words, TM modes starts to dominate field profile in the geometry at widths around 0.3 μm in broadband and effective wavelength matching is dominant at smaller widths.

3.3. Tungsten Based Spectrally Selective Absorbers with Anisotropic Rough Surface Texture

We first studied the effect of surface roughness on Tungsten surfaces. To analyze the influence of surface morphology on spectral absorption of Tungsten surfaces in the VIS and NIF spectral regions, the absorption spectra of the flat and roughened Tungsten surface are compared in Figure 28. As can be seen in this figure, the spectral absorption Tungsten increases significantly by using surface roughness in comparison to a flat Tungsten surface, especially for wavelength below 1500 nm. This phenomenon comes from the mode interactions and the corresponding effects on absorption. It is worth noting that in the spectral region of interest, 0.4-1.5 μm, Tungsten does not support surface plasmons. Tungsten has shown a nonzero value of 2.5–4 for the real and imaginary parts of its permittivity. Within this wavelength range, n decreased gradually while k increased monotonically. Also, in Figure 28, the absorption reduces in the longer wavelengths, and there is not a notable difference between flat and rough surfaces. Our results indicate a strong relationship between the absorption spectra of rough Tungsten surfaces Tungsten and the correlation length and RMS height of the rough surface.

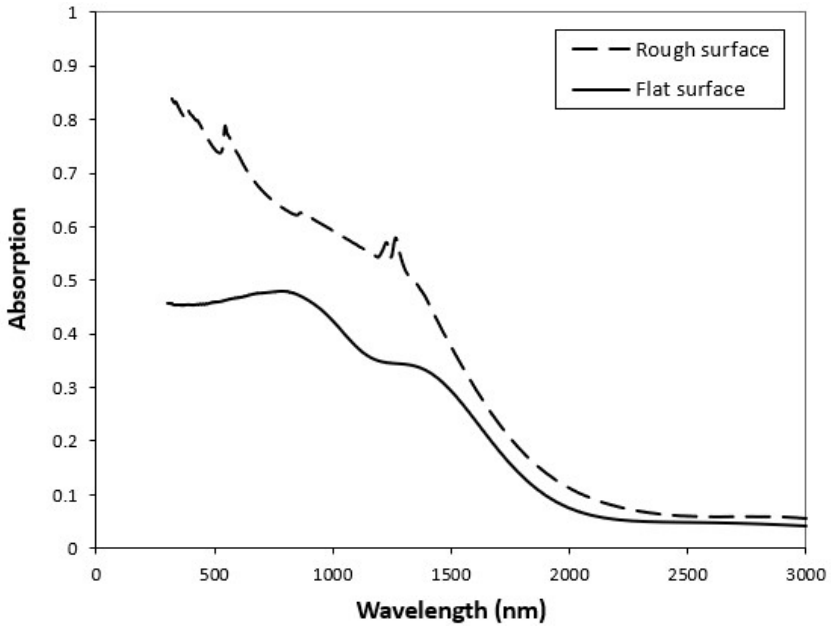

Figure 28: Comparing Absorption of Flat and rough (lx=100 nm, ly=100 nm and h=50 nm) Tungsten finite thickness film by FDTD solution

In Figure 29(a), the absorption spectra of various surfaces with different correlation lengths at fixed RMS height of h= 50 nm are given. As can be seen, increasing the roughness by reducing the correlation length, which increases the slope of the surface facets at a fixed RMS height, increases the absorption of the surface. A similar effect can be observed in Figure 29(b), where the

absorption spectra is given for various heights at a fixed correlation length of l= 100 nm. Both Figure 29(a) and Figure 29(b) shows no significant difference between textures with varying *l* and *h* are observed at longer wavelengths, with decreasing the correlation length in the isotropic case, the absorption increases in the VIS region, as shown in Figure 29(a). As we increase the correlation length to values larger than 200 nm, a peak in the absorption spectra is observed. It could be noted that when the correlation length becomes larger than λ/5, a peak resonance is observed in the absorption spectra. This effect intensifies by increasing the RMS height of rough texture, and the dip point in the absorption spectra reaches unity. Based on the optimized values obtained in Figures 29(a) and 29(b), a correlation length of 200 nm and a minimum height of 100 nm is selected to have an absorption dip in a specified wavelength region.

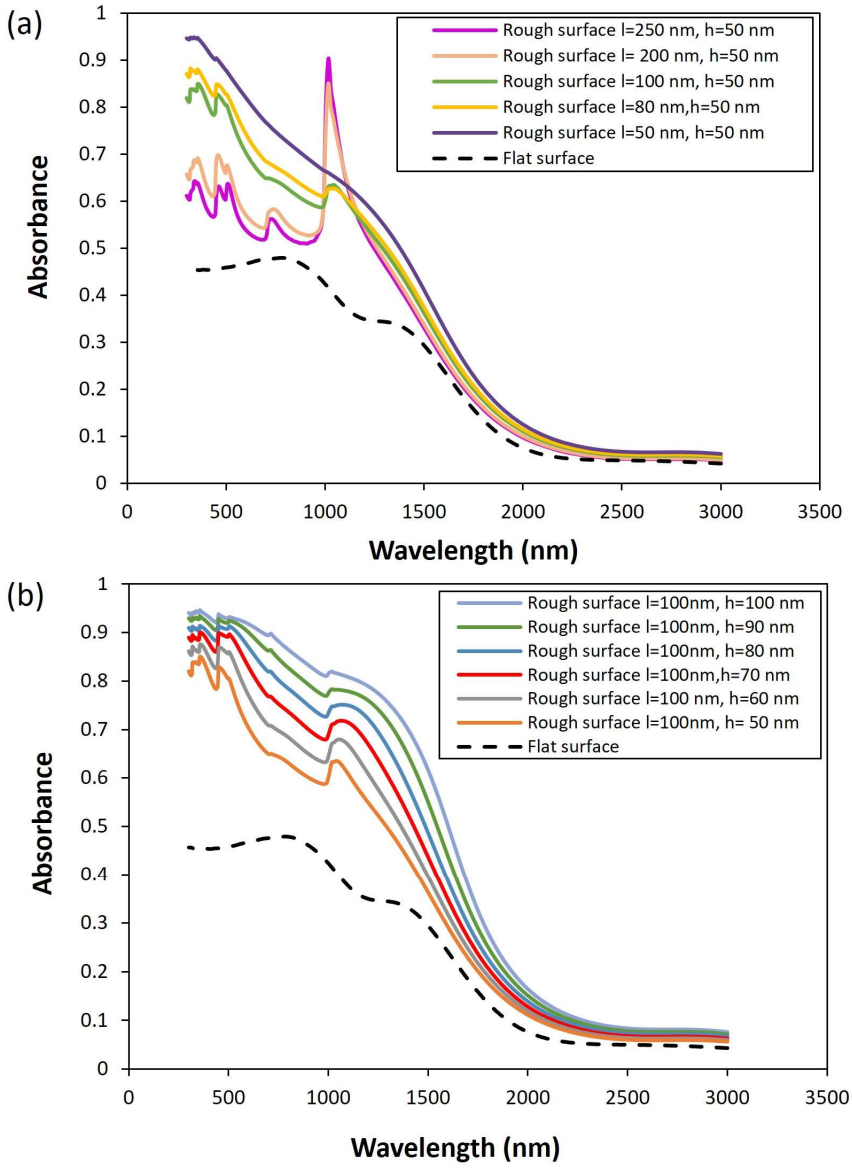

Figure 29: The effect of (a) Correlation length and (b) RMS height in the absorption spectra of random rough surface Tungsten

The spectral distribution of the Absorption of Tungsten surfaces can be influenced by the surface roughness by selectively changing the correlation length and RMS height of the random rough surface as shown in Figure 30. In particular, the bandwidth of the spectral distribution can be greatly enhanced. This phenomenon can be used in the spectral selective absorbers, in which high absorption is needed at a specific wavelength. Based on the results in Figure 30, a surface with a correlation length of 200 nm and a RMS height of more than 100 nm shows absorption of nearly 100% absorption at the wavelength in range of 1000-1500 nm. A relatively narrowband absorption is detected for systems with a lower RMS height. Additionally, the VIS region has a lower spectral absorption. These characteristics are primarily due to the decreased optical coupling efficiency and narrow bandwidth of the resonances supported by the small surface peaks. Increasing the height of rough texture increases not only the absorptions in the VIS region but also the broad bandwidth of absorption. Furthermore, the near-unity absorption is accessible over a larger bandwidth. The reason is that rough surface height increases the degree of interaction between resonance and trapping light. Note that the higher the surface height, the more trapping of long-wavelength waves. It should be noted that the absorption curve at low wavelengths (approximately up to 1000 nm) is flatter with a higher RMS height value. Correlation length and RMS height could be used as controlling factors for a spectrally selective absorber. It is shown that for the wavelength in the range of 1000- 1600 nm, a very high absorption around 0.95 could be obtained just by the roughness of the surface without any additional coatings. In addition, an average of 47% improvement in the absorption is observed in the wavelength in the range of 300-1000 nm for the case of l=200 nm and h=180 nm in comparison to the flat surface, which is beneficial for high-temperature applications. Simulation results show that increasing the RMS height with a proper correlation length increases the bandwidth of the absorption. This increase in absorption is caused by the coupling between the surface peaks' resonant modes. For an RMS height of 180 nm, the absorption curve is over 85% in a wide wavelength range of 300–1600 nm. At the same time, for the wavelengths of 1000–1600 nm, the absorption value is more than 95%. For higher heights, the coupling between the surface peak's resonance mode occurs in a wider range of wavelength, which cause a broader bandwidth of absorption.

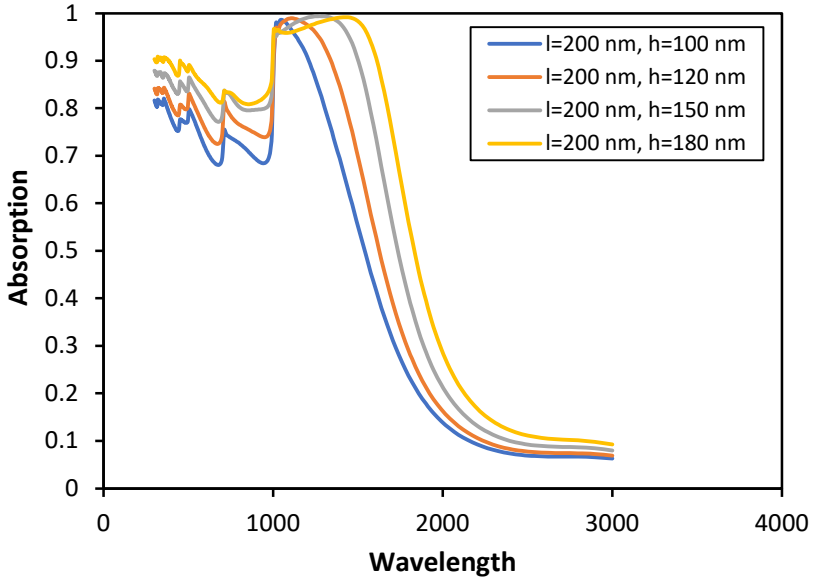

Figure 30: The RMS height effect on bandwidth of absorption

In the next step, inspired by grating couplers to control the light-matter interaction at material surfaces, we investigated the effect of anisotropic rough surfaces. Anisotropic surface roughness can be obtained by a Gaussian surface with two different correlation lengths along x, y, marked as l_x, l_y respectively. As can be seen in Figure 31, anisotropic surfaces also show the spectrally selective characteristic, which means that at a specific wavelength, the absorption increase dramatically. Figure 31 illustrates the absorption spectra for various anisotropic surfaces. The results in Figure 31 indicate that the absorption of the anisotropic rough surface can be lower than the isotropic rough surface with the same correlation length (l_x=200 nm, Figure 31 (b)) in the x-direction, which is shown with a black dash line in Figure 31 (a). It means that with the same correlation length in the x-direction, decreasing the correlation length in y-direction which causes a drop in absorption values. However, lower correlation length in x-direction (l_x=100 nm) in the anisotropic case leads to more Absorption in VIS spectrum and, at the same time, spectrally selective characteristics (red dash line in Figure 31 (a) and 31 (c)). Moreover, higher absorption can be obtained in the infrared region for the anisotropic case of l_x=100 nm, l_y=400 nm, and h=100 nm. The absorption results of W anisotropic rough surface with lx=200 nm and l_y= 800 nm, which is shown in Figure 31 (d), shows two clear resonance peaks in its spectrum the first one is in 533 nm with 85% absorption, and the second one is 1082 nm with 87% absorption. In addition, the above results show that anisotropic rough surfaces with lower correlation length in the x-direction can be used to obtain higher absorption in comparison to the isotropic rough surfaces with higher RMS height. In other words, at the same RMS height, anisotropic rough surfaces with lower correlation length could be used instead of isotropic rough surfaces to have more Absorption in VIS and near-infrared region.

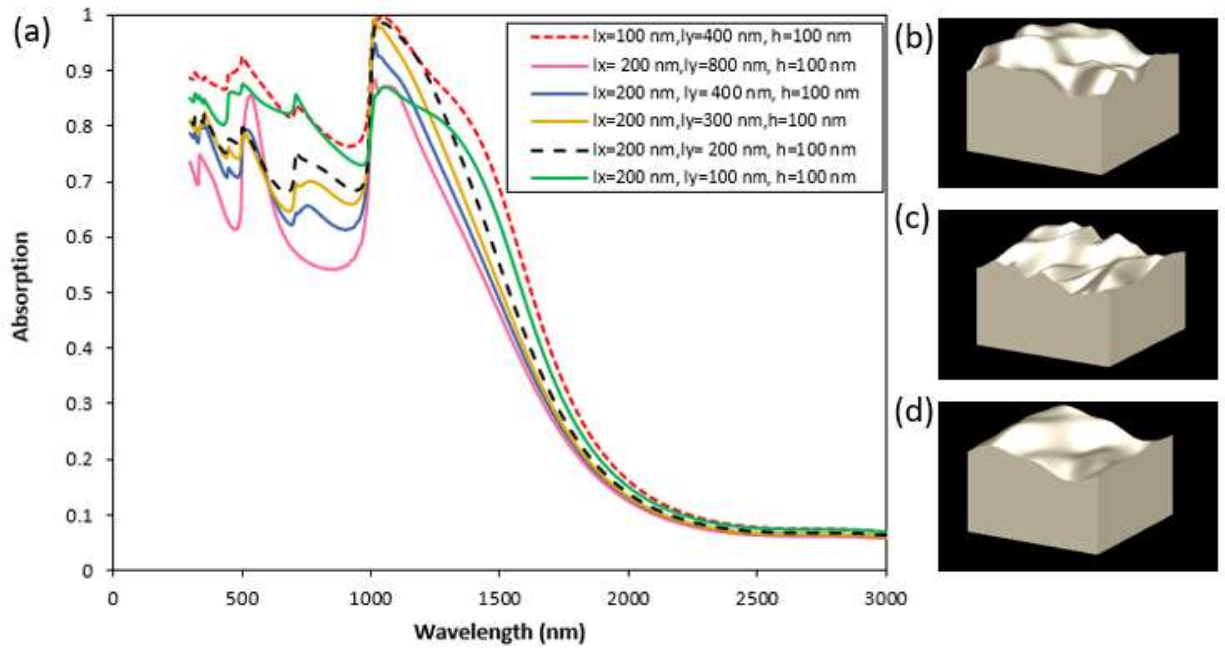

Figure 31: (a) The effect of correlation length for W anisotropic rough surface (b) Isotropic rough surface with l=200 nm and h=100 nm. (c) Anisotropic rough surface with l_x=100 nm, l_y= 400 nm, and h=100 nm. (d) Anisotropic rough surface with l_x=200 nm, l_y=400 nm, and h=100 nm

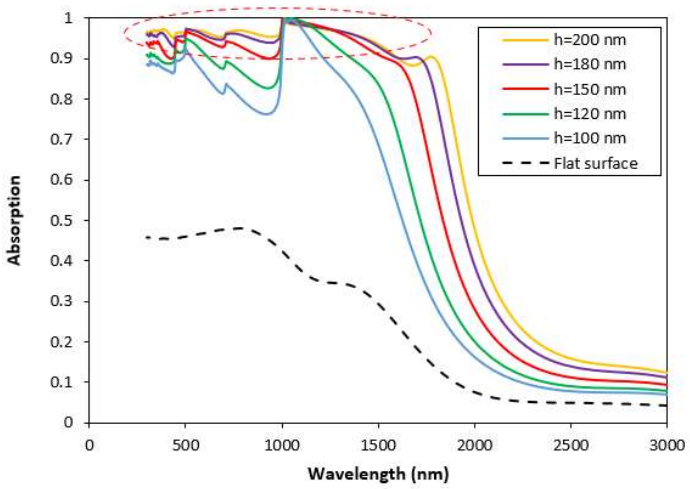

Figure 32: The RMS height effect on the absorption of the anisotropic rough surface of Tungsten with lx=100 nm, ly=400 nm

In Figure 32, the effect of RMS height on the absorption band is investigated. As mentioned above, for the isotropic random rough surfaces with increasing the RMS height, the bandwidth of absorption increases. It is observed that started from λ=1000 nm; the perfect absorption spectrum is continuously broadened. For anisotropic random rough surfaces, as can be seen from Figure 32, with increasing the RMS height of the surface, a vast bandwidth is obtained, which started from λ=300 nm and continued to λ=1500 nm. It is shown that for the case of the anisotropic surface with lx=100 nm and ly=400 nm, for RMS height of 150 nm with taking the absorption>90% into account, the spectral range is varied from 300 nm to 1700 nm, suggesting a perfect absorption bandwidth up to 1700 nm in the ultraviolet- visible-near infrared region and for the RMS height of 180 nm the absorption reaches to more than 95% which is a very great improvement in comparison to the flat Tungsten surface and have a lot of application in high-temperature situations. This wide broadband is also obtained previously in the literature, but in all cases, another material coating was added to Tungsten for reaching these high absorptions [22,132]. However, in our results, this broad bandwidth is just obtained by modifying the surface structure. Moreover, in comparison to the flat Tungsten surface, the absorption enhanced around 52% in the VIS region and approximately 80% for larger wavelengths from 1500-2000 nm.

3.4. Impedance Mismatch-Based Enhancement of Broadband Reflectance of Tungsten with Bio-Inspired Multi-layers

The average reflectance of the multilayer with the increasing number of layers is shown in Fig. 33(a), for which the corresponding layer materials and thicknesses are given in Table 1, and the spectral reflectance of the multilayer composed of eight layers is shown in Fig. 33(b). The average reflectance of the multilayer in both spectrum intervals reaches 95% levels from 50% and 80% levels for eight layers. Change of average also indicates that when layer number is higher than 4, there are enough design parameters to increase the average in both spectrum intervals. Amplitudes of the reflectance coefficients are also demonstrated in S-plane in Fig. 33(c). Illustrated amplitudes of the reflection coefficients of W with and without multilayer agrees with the spectral characteristics. As seen, all amplitude values shift towards the outer edge of the unit circle. Besides the broadband reflectance enhancement, a multilayer structure yields sharp drops over the

spectrum. To analyze the nature of the peaks and the broadband reflectance characteristics, the total optical path, δ_{Total}, that light travels throughout the homogeneous multilayer structure, is plotted in Fig. 33(d).

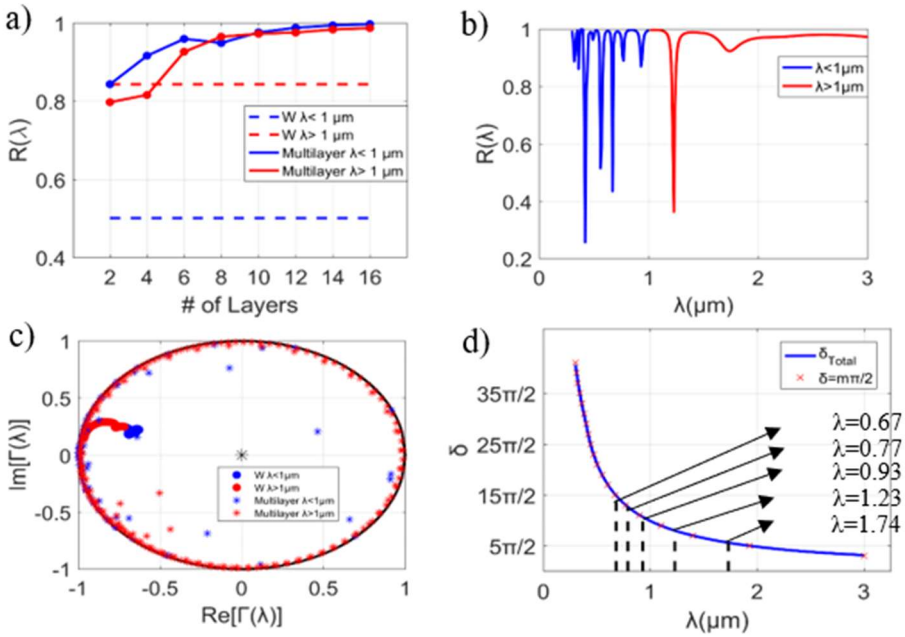

Figure 33: a) Reflectance of homogeneous multilayers for increasing number of layers. b) Spectral reflectance of a multilayer with 8 layers designed for α =0.7 with TiO_2 and air. c) Reflectance coefficients of the multilayer whose spectral reflectance is given in Fig. 4(b) on -S plane. d) Comparison of optical thickness of the multilayer structure on which even multiples are marked.

Table 2: Thicknesses of the layers used in the multilayers with layer numbers of 2, 4, 6, 8, 10, 12, 14 and 16 on top of 500 nm W.

Layer Material	# of Layers							
	2	4	6	8	10	12	14	16
W (500 nm)	Thickness [nm]							
Air	119.15	106.2	279.04	268.94	62.43	88.35	185.98	59.1
TiO_2	67.04	68.28	93.08	256.86	126.53	220.75	680.19	181.23
Air		145.02	126.96	136.88	178	703.4	245.15	229.43
TiO_2		108.12	58	125.96	132.21	132.48	121.29	259.87
Air			130	136.36	93.58	754.92	177.59	698.30
TiO_2			59.56	187.64	169.5	235.62	122.6	149.04
Air				181.74	414.79	480.91	273.93	650.99
TiO_2				65.06	208.07	630.17	324.03	156.19
Air					196.16	125.36	231.37	669.27
TiO_2					309.87	544.92	417.35	239.12
Air						428.56	37.48	951.18
TiO_2						131.24	233.66	154.34
Air							203.49	756.69
TiO_2							151.68	396.4
Air								751.85
TiO_2								504.2

For verification purposes, we compared the reflectance spectrum of the 8-layered structure, for which layer materials and thicknesses are depicted in Table 1, obtained by the described impedance formulation, characteristic matrix method [60] and the FDTD [55]. As seen in Fig. 34(a), there is very good agreement between the analytical solution (both impedance formulation and characteristic matrix method belongs to this category) and the FDTD solution. Also, to quantify the dependence of the broadband reflectance spectrum on meshing, we compared the total absorption percentage, which is expressed as $\mathrm{I_{BB}}(\lambda, \mathrm{T} = 5850\ \mathrm{K})\mathrm{x}\big(1 - \mathrm{R}(\lambda)\big)\mathrm{x}100/\mathrm{I_{BB}}(\lambda, \mathrm{T} = 5850\ \mathrm{K})$. As seen in Fig. 34(b), absorption percentage remains around %8 and does not significantly change as the number of mesh points is increased beyond 14. Therefore, we proceeded with FDTD simulations with mesh points of 14.

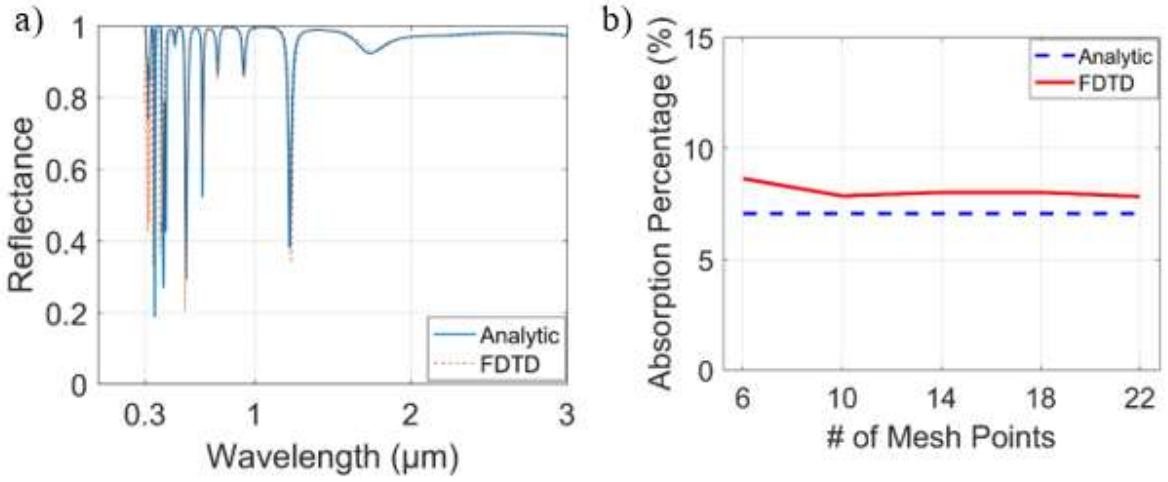

Figure 34: a) Analytical solution of the 8-layered structure obtained analytically by characteristic matrix method [60] vs. FDTD solution with number of mesh points of 14. b) Mesh accuracy vs. absorption percentage of the incident radiation.

It is well known that a medium highly reflects incident wave if the optical path at that wavelength is an odd multiple of $\pi/2$. By relying on this, odd multiples, m, of $\pi/2$, is also marked on the plot depicted in Fig. 33(d). It is observed that there is a perfect fit between $m\pi/2$ and δ_{Total}, which clarifies the broadband reflectance behavior. Wavelengths of the sharp drops over the spectrum are also marked, which correspond to λ = 0.67, 0.77, 0.93, 1.23, and 1.74 μm wavelengths. Here, sharp dips appear in the regions between the wavelengths where odd multiples are crossing with δ_{Total}.

High reflectance zones over the spectrum are generated when δ_{Total} becomes close to an odd multiple of $\pi/2$, and in between two odd multiples, δ_{Total} approaches to even multiples of $\pi/2$, which is associated with high transmission. Due to the increased number of odd multiple modes at shorter wavelengths, the even multiples, rate of appearance of sharp dips increase, and more oscillatory reflectance spectrum are observed. As a next step, the effects of lift-off material properties and their dimensions on the reflectance spectrum are studied, and corresponding results are depicted in Fig. 35(a) and 35(b). In Fig. 35(a), n_{Lift} is set to 1.41, and the reflectance spectrum for the updated multilayer with eight layers is obtained.

A decrease in reflectance, especially at the shorter wavelengths, is observed with increasing lift-off dimensions. This stems from the perturbation introduced in the air medium, which changes the medium's refractive index in the design stage. With increasing volume fraction of the lift-off material, the effective index of the medium starts to deviate more from the presumed value of $n_{Air} = 1$ and alter the interference effects between the mediums. Similarly, in Fig. 35(b), in which the reflectance spectrum for varying n_{Lift} is depicted for 50*50 nm lift-off material dimensions, reflectance intensities start to decrease slightly. Similar reasoning is also valid here.

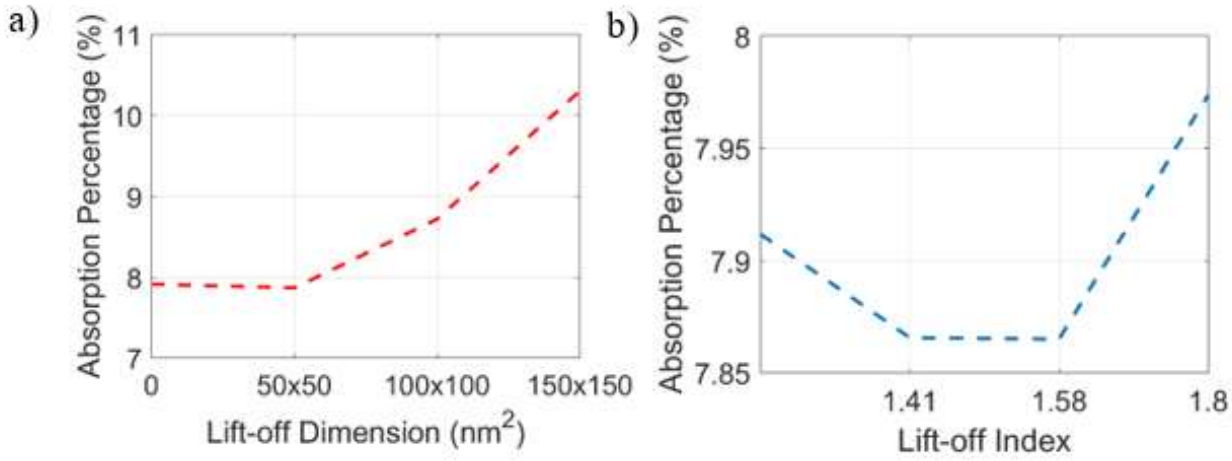

Figure 35: a) Reflectance spectrum of the structure with 8 layers in which lift-off layers (n =1.58) of various sizes are added. b) Reflectance spectrum of the structure with 8 layers in which lift-off layers (100*100 nm) of different refractive indices are added.

There are two possible advantages of the inhomogeneous multilayers over the homogenous ones, in which layers are separated with air gaps, from a thermomechanical point of view. Due to the increased ratio of the refractive indices between the layer materials, higher reflection percentages can be achieved with fewer layers [133]. In addition, air gaps provide space for the layers for thermal expansion under excessive thermal load. In the absence of air gaps, due to the difference between thermal expansion coefficients of the layers, high thermal stresses can occur under excessive thermal load, which lead to mechanical failure of the coating. By introducing air gaps, layers are allowed to expand with less resistance. In addition, separated features are also more advantageous compared to a single large feature. The thermal expansion of a single large feature, in transverse directions is much larger than the thermal expansion of the smaller features, as seen from the mathematical expression for linear expansion under uniform temperature variation $\Delta L = Li \times \alpha \times \Delta T$ where L_i is the initial length, α is the thermal expansion coefficient, (given as 9.5×10^{-6} K^{-1} for TiO_2), ΔT is the temperature change $(T_{Final} - T_{Initial})$, and ΔL is the length change $(L_F - L_i)$. Under constant temperature change over the layer, ΔL can be calculated. In Fig. 36(b), ΔL is plotted with respect to temperature change, ranging from 100 K to 1000 K, for varying L_i, is demonstrated. As seen, with increasing L_i, ΔL also increases. By introducing inhomogeneities in transverse directions, features will be separated from each other, and they are allowed to expand in those directions, which will be less than the expansion of a single large layer. For this purpose, understanding the effect of periodicity on spectral characteristics is essential.

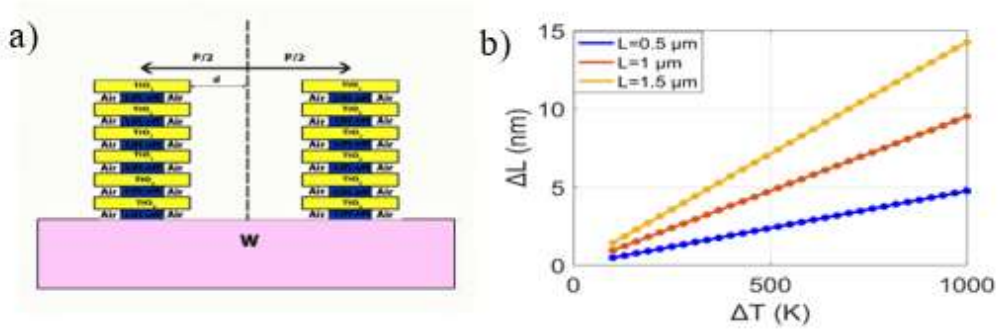

Figure 36: a) Scheme for the periodically arranged morpho butterfly inspired multilayer features. b) Temperature change vs. linear length change for initial lengths of 0.5, 1 and 1.5 μm.

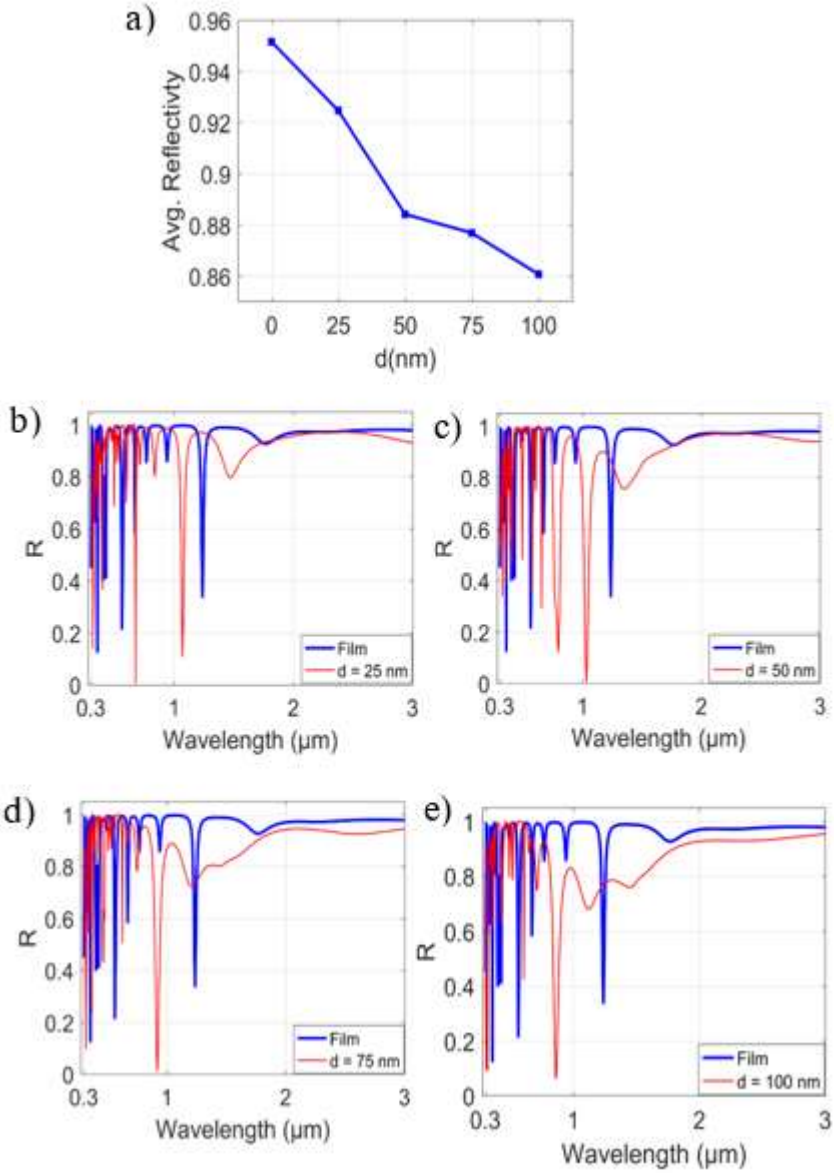

Figure 37: a) Average reflectance of structures for varying distance/periodicity. b-c-d-e) Spectral reflectance of the structures for varying distance/periodicity.

According to Fig. 36, the distance between two neighboring ridges, (*d*) parameter, is one of the most important variables that affects the structure's reflectivity. In this regard, the average reflectivity for distances of 25, 50, 75, 100 nm has been calculated, and the results can be seen in Fig. 37(a). It can be understood from this figure that increasing the distance between two adjacent ridges decreases the amount of reflectivity from 95% to less than 86%. Furthermore, to compare the effect of the shape of inhomogeneous structures on spectral characteristics, the reflectance of the proposed model for the morpho butterfly wing's nanostructure is depicted in Fig. 37(b-d). Periodicity, *P*, in the calculations is set to 0.5 μm.

However, increasing the gap between two adjacent ridges causes frequent oscillations, especially in shorter wavelengths, which lead to reduced average reflectance. Such oscillations stem from the additional interference effects induced by the air gaps between the periodic structures introduced by non-zero *d*. Contribution from such additional interference effects alters the total optical path that waves travel through the structure. However, the total optical path cannot be calculated by the theory developed for homogeneous layers, which is only applicable for zero *d*. Therefore, a -*S* parameters retrieval method [124] is applied to calculate the -*S* parameters of the studied multilayer structures. -*S* parameters can be treated as the transfer function of the multilayer structure, therefore provides an understanding of the optical response of the structures in consideration. Since the reflectance spectrums of the structures are of interest, only S_{11} parameters are analyzed.

S_{11} parameters are identical to reflectance coefficients given in Eq. (26) and can be represented with magnitude and phase terms. Since phase term determines the optical path that wave travels, phase of S_{11} terms, $<S_{11}$, are studied in the entire spectrum interval. The distinct reflection dips occurring in the 1-1.6 μm spectrum are analyzed to make a detailed evaluation. Then the analysis is extended to a broader spectrum.

In Fig. 38(a), reflectance dips occurring in 1-1.75 μm wavelength interval for the structures with *d = 25, 50, 75,* and *100 nm* are illustrated. As seen, all these dips are shifted to shorter wavelengths compared to homogenous film. A single dip is observed for the structures with *d = 25*, *50*, *75 nm*, and two dips for *d = 100 nm*. In Fig. 38(b), $<S_{11}$ are plotted concerning wavelength, and even multiples of π are marked with black dashed lines. As seen, the $<S_{11}$ curve of the structure with *d = 25 nm* crosses *0* at 1.45 μm. When considered with the reflectance spectrum depicted in Fig. 38(a), it can be seen that crossing points are very close to reflection dips. Similar trends are observed for the structure with *d =50 nm* whose $<S_{11}$ crosses *0* at 1.3 μm wavelength, which corresponds to the reflectance location dip. Again, single crossing at *0* occurs for the structure with *d =75 nm* and resulting in a single dip in the reflectance spectrum. Finally, the structure with *d = 100 nm* has two crossing points, around 1.18 and 1.57 μm, which result in a distinct and relatively smooth dip in the reflectance spectrum, respectively. To analyze the characteristics at shorter wavelengths that exhibit more frequent oscillations, $<S_{11}$ curves in 0.3 – 3 μm spectrum are plotted with even multiples of π are marked and demonstrated in Fig. 38(c). As seen, the slope of the $<S_{11}$ curves is nearly similar for $\lambda>1$ μm. Therefore, the number of $m\pi/2$ crossings *(m =0,2,4,...N)* are observed in the spectrum are less. With the increasing slope of $<S_{11}$

curves at $\lambda<1$ µm, the number of $m\pi/2$ crossings increases, therefore the number of oscillations increases.

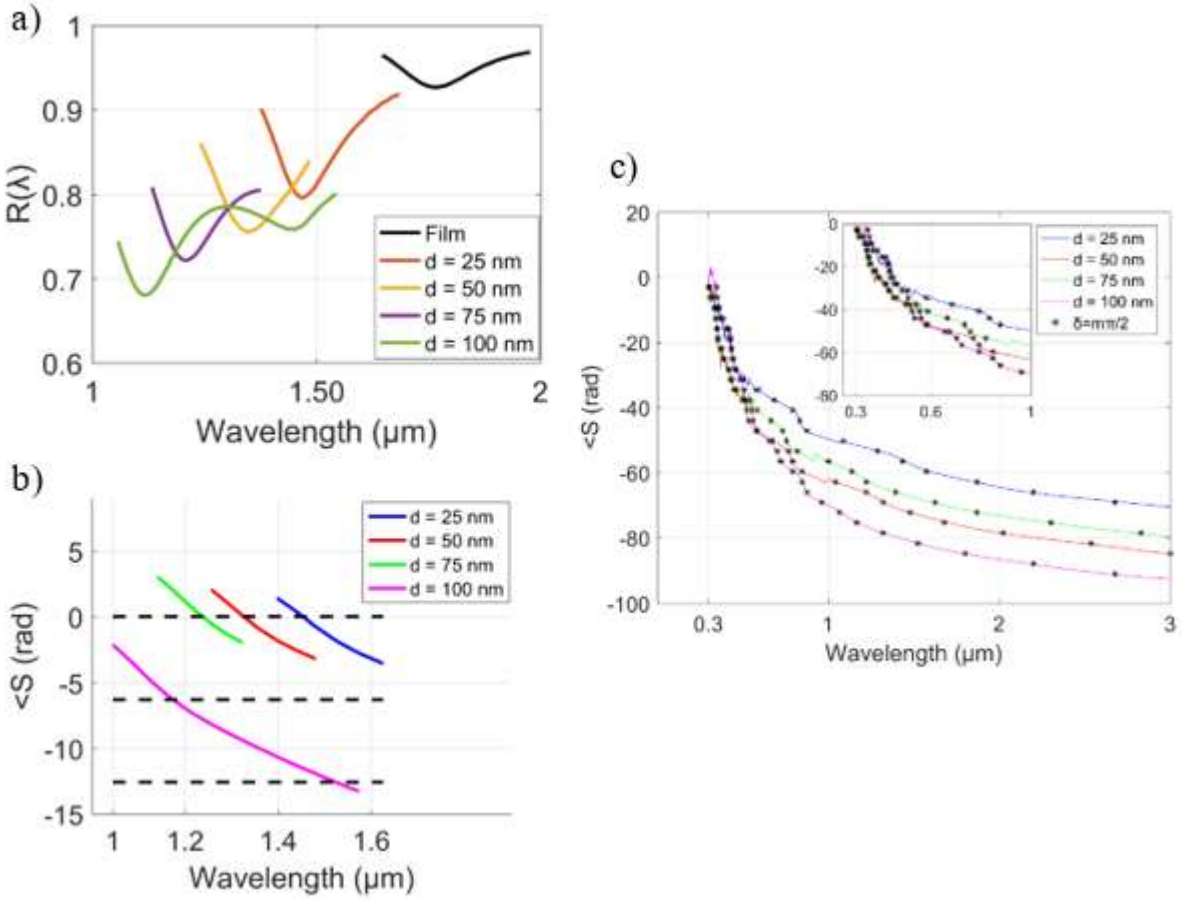

Figure 38: a) Distinct reflectance dips for the structures with different d. b) <S11 curves of the structures with different d for which reflectance dips are shown in Fig. 8(a). c) <S11 curves of the structures with different d in 0.3 – 3 µm interval with even multiples of π/2 are marked.

In the light of these results, it is expected that average reflectance will further decrease with increasing *d.* Therefore, to have more efficient thermal management, one should consider the increasing radiative thermal load in the coating with increasing *d* [30,42].

Finally, in addition to the effect of the variation of the refractive index and dimensions of the lift-off materials on the broadband reflectance, the sensitivity of the final structure against possible fabrication imperfections is also studied. For this purpose, ±5 nm was selected, which is within the manufacturing tolerances of the current fabrication technologies, such as electron and ion beam deposition. These modifications are made to the geometric dimensions of the structure with 8 layers which is expressed by 24 geometrical parameters (3 for each layer in 3D) and calculated the reflectance of the structure. Reflection calculations are repeated 10 times. The means and standard deviations for both low and high reflectivity spectrum intervals are plotted in Fig. 39. As seen in Fig. 39, standard deviations are very low (0.2 % and 1 % for λ<1 µm and λ>1 µm intervals) with the added possible fabrication errors, which shows the robustness of the structure for possible fabrication error*s*.

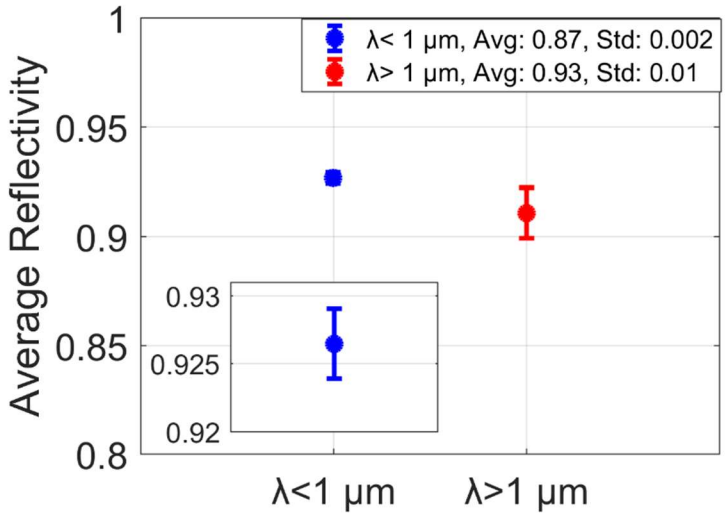

Figure 39: Mean and standard deviations of the average reflectivity of the 8-layered final structure with d = 25 nm both at wavelengths in 0.3 – 1 μm and 1 – 3 μm intervals.

4. Conclusions

In this project, the random surface roughness effects on the reflectivity of refractory metals and polar dielectrics is studied. SPM/SSA method enables the decomposition of surface roughness topography and material properties. Larger n shows higher roughness effect as well as broader length scale range which are illustrated as weighting functions. Transparent dielectrics with with low k values experiences two resonance locations on the weighting function, corresponding to the periodicity of roughness same as incident wavelength and the wavelength in material. Absorption increase (k increase) for materials will increase the weighting function in magnitude, but the secondary resonance peak weakens and disappears. Maximum roughness effect happens when k is similar in terms of magnitude as n, where epsilon is close to zero.

For refractory metal W, as n and k are relatively close in terms of magnitude at the visible to infrared range, surface roughnesses with the corresponding correlation lengths cause higher absorption change with same roughness height variance. At far-infrared region, where flat W surface experience high reflectivity, reflection change due to surface roughness is also limited. For SiC, as the magnitude k is smaller compared to n at infrared, surface roughness caused reflection change is limited, however, polar resonance at λ around $12\mu m$ causes one resonance peak at this location for the surface roughness effect. Our results indicate that maximum impact on the reflection from a rough material surface is observed when the correlation length of the random surface roughness satisfies $l = 2.22\lambda_0$ condition and the operation frequency matches the internal absorption frequencies (plasma frequency and phonon frequency).

Moreover, in this project, broadband absorption mechanism of the black silicon is investigated. Field distributions inside the random and deterministic textures show that high field intensities which are confined near the edges of the textures occur. Detailed analysis shows that high coupling in transverse direction occurs and coupling conditions are estimated with effective wavelength matching phenomenon in optical antennas. Further analysis reveals that, TM modes are also supported in the textures and affects the absorption distribution over the geometry. Due to the trapezoidal geometry of the textures, TM modes start to form with increasing width (*d*). It is found out that effective wavelength matching occurs in smaller widths ($d<0.3$ μm) and are dominant in terms of contribution to absorption. On the other hand, TM modes start to dominate at higher widths ($d>0.3$ μm) in broadband for which cut-off wavelengths are obtained by waveguide theory. Destructive interference of the fields induced by these two different phenomena lead to slightly reduced spectral absorption. Our findings regarding to driving mechanisms of elevated absorption in black silicon provide a good understanding of those mechanisms which was not discussed in such a detailed manner before.

Furthermore, we demonstrated spectrally selective absorber surface made of Tungsten using an anisotropic Gaussian random rough surface for high-temperature applications. It is shown that the rough surface enhances the absorption spectra both in the visible and near infrared spectral regions. For isotropic random rough surfaces, it is shown that at correlation length higher than 200 nm, a dip started to appear in the absorption curve around the wavelength of 1000 nm. Increasing RMS height leads to broadening the bandwidth of near-unity absorption for the 1000-1600 nm region due to more optical interference. Our investigation shows that using anisotropic random rough surface design yields even more interesting results in terms of the absorption spectrum. More than 90% absorption is obtained for the optimized anisotropic random rough surface for the spectral range from 300-1700 nm, suggesting a perfect absorption bandwidth up to 1700 nm in the ultraviolet- visible-near infrared region. These random nanostructures provide multiple resonant modes, which introduce strong optical coupling and result in a broadening of the high absorption spectrum region. The proposed spectrally selective absorber in this study eliminates the need for adding extra layers or nanoparticles to act as spectral selective emitters. Moreover, this technique avoids inserting additional surface thickness by adding coatings of different materials. These findings can be used in tailoring broadband spectrum for different applications in which the surfaces are exposed to high temperatures, such as solar and aerospace applications.

Finally, optimized multilayer coatings inspired from morpho butterfly structures are proposed in this project to increase the reflectivity of Tungsten in the broadband spectrum of 0.3-3μm. The impedance mismatch method results indicate that stacking eight number of TiO_2-Air (As high index-low index) layers on the tungsten substrate with the optimized thicknesses increases the average reflectivity of Tungsten up to 95% in the broadband spectrum. It is shown that lift-off dimensions and optical properties do not significantly impact the selected values. While the inhomogeneities in the transverse direction do not cause a significant reduction in the reflectance, a slight decrease in magnitudes is observed due to an increased number of sharp reflection dips over the spectrum. Calculated -S parameters of the final inhomogeneous structures show that reflection dips occur when <S become multiples of π, and the number of crossings increases at shorter wavelengths. Spectral analysis of different distances between the ridges, *d*, indicates that reflectance of the coating is reduced with increasing *d.* The highest reduction rate is observed for *d~100 nm*, for which average reflectance drops to 86 % levels at most. Robustness of the final

structure against possible fabrication imperfections described by adding ±5 nm tolerance in dimensions indicate the means of the average reflectance changes by % 1 at most at longer wavelengths.

5. References

[1] S.Y. Jeong, C.Y. Tso, J. Ha, Y.M. Wong, C.Y.H. Chao, B. Huang, H. Qiu, Field investigation of a photonic multi-layered TiO2 passive radiative cooler in sub-tropical climate, Renew. Energy. 146 (2020) 44–55.

[2] M.A. Kecebas, M.P. Menguc, A. Kosar, K. Sendur, Spectrally selective filter design for passive radiative cooling, JOSA B. 37 (2020) 1173–1182.

[3] H. Ma, K. Yao, S. Dou, M. Xiao, M. Dai, L. Wang, H. Zhao, J. Zhao, Y. Li, Y. Zhan, Multilayered SiO2/Si3N4 photonic emitter to achieve high-performance all-day radiative cooling, Sol. Energy Mater. Sol. Cells. 212 (2020) 110584.

[4] N. Pirouzfam, K. Sendur, Tungsten Based Spectrally Selective Absorbers with Anisotropic Rough Surface Texture, Nanomaterials. 11 (2021) 2018.

[5] B. Wu, Z. Liu, G. Liu, X. Liu, P. Tang, G. Du, W. Yuan, M. Liu, An ultra-broadband, polarization and angle-insensitive metamaterial light absorber, J. Phys. D. Appl. Phys. 53 (2019) 95106.

[6] S. Mehrabi, M.H. Rezaei, A. Zarifkar, Ultra-broadband solar absorber based on multi-layer TiN/TiO 2 structure with near-unity absorption, JOSA B. 36 (2019) 2602–2609.

[7] L. Chan, E.A. DeCuir, R. Fu, D.E. Morse, M.J. Gordon, Biomimetic nanostructures in ZnS and ZnSe provide broadband anti-reflectivity, J. Opt. 19 (2017) 114007.

[8] M. Rashid, N.M. Ahmed, N.A.M. Noor, M.Z. Pakhuruddin, Silicon quantum dot/black silicon hybrid nanostructure for broadband reflection reduction, Mater. Sci. Semicond. Process. 115 (2020) 105113.

[9] G. Christidis, U. Koch, E. Poloni, E. De Leo, B. Cheng, S.M. Koepfli, A. Dorodnyy, F. Bouville, Y. Fedoryshyn, V. Shklover, Broadband, high-temperature stable reflector for aerospace thermal radiation protection, ACS Appl. Mater. Interfaces. 12 (2020) 9925–9934.

[10] M. Schürmann, S. Schwinde, P.J. Jobst, O. Stenzel, S. Wilbrandt, A. Szeghalmi, A. Bingel, P. Munzert, N. Kaiser, High-reflective coatings for ground and space based applications, in: Int. Conf. Sp. Opt. 2014, International Society for Optics and Photonics, 2017: p. 105630M.

[11] M.C. Gupta, C. Ungaro, J.J. Foley IV, S.K. Gray, Optical nanostructures design, fabrication, and applications for solar/thermal energy conversion, Sol. Energy. 165 (2018) 100–114.

[12] T. Inoue, M. De Zoysa, T. Asano, S. Noda, Realization of narrowband thermal emission with optical nanostructures, Optica. 2 (2015) 27–35.

[13] Z. Zhou, E. Sakr, Y. Sun, P. Bermel, Solar thermophotovoltaics: reshaping the solar spectrum, Nanophotonics. 5 (2016) 1–21.

[14] I.E. Khodasevych, L. Wang, A. Mitchell, G. Rosengarten, Micro-and nanostructured surfaces for selective solar absorption, Adv. Opt. Mater. 3 (2015) 852–881.

[15] J. Oh, H.-C. Yuan, H.M. Branz, An 18.2%-efficient black-silicon solar cell achieved through control of carrier recombination in nanostructures, Nat. Nanotechnol. 7 (2012) 743–748.

[16] C. Ungaro, S.K. Gray, M.C. Gupta, Black tungsten for solar power generation, Appl. Phys. Lett. 103 (2013) 71105.

[17] S.J. Zhang, S. To, S.J. Wang, Z.W. Zhu, A review of surface roughness generation in ultra-precision machining, Int. J. Mach. Tools Manuf. 91 (2015) 76–95.

[18] J.Q. Bagley, L. Tsang, K.H. Ding, A. Ishimaru, Optical transmission through a plasmon film lens with small roughness: Enhanced spatial resolution of images of single source and multiple sources, JOSA B. 28 (2011) 1766–1777.

[19] S. Huang, H. Wang, K.-H. Ding, L. Tsang, Subwavelength imaging enhancement through a three-dimensional plasmon superlens with rough surface, Opt. Lett. 37 (2012) 1295–1297.

[20] S.K. Mishra, V. Kumar, S.K. Tiwari, T. Mishra, G. Angula, S. Adhikari, Development and degradation behavior of protective multilayer coatings for aluminum reflectors for solar thermal applications, Thin Solid Films. 619 (2016) 202–207.

[21] D.M. Fryauf, A.C. Phillips, N.P. Kobayashi, Corrosion barriers for silver-based telescope mirrors:

comparative study of plasma-enhanced atomic layer deposition and reactive evaporation of aluminum oxide, J. Astron. Telesc. Instruments, Syst. 1 (2015) 44002.
[22] X. Han, K. He, Z. He, Z. Zhang, Tungsten-based highly selective solar absorber using simple nanodisk array, Opt. Express. 25 (2017) A1072–A1078.
[23] K.P. Sibin, S. John, H.C. Barshilia, Control of thermal emittance of stainless steel using sputtered tungsten thin films for solar thermal power applications, Sol. Energy Mater. Sol. Cells. 133 (2015) 1–7.
[24] F. Cao, D. Kraemer, T. Sun, Y. Lan, G. Chen, Z. Ren, Enhanced Thermal Stability of W-Ni-Al2O3 Cermet-Based Spectrally Selective Solar Absorbers with Tungsten Infrared Reflectors, Adv. Energy Mater. 5 (2015) 1401042.
[25] G. Silva-Oelker, C. Jerez-Hanckes, P. Fay, High-temperature tungsten-hafnia optimized selective thermal emitters for thermophotovoltaic applications, J. Quant. Spectrosc. Radiat. Transf. 231 (2019) 61–68.
[26] A. Khan, R. Elliman, C. Corr, J.J.H. Lim, A. Forrest, P. Mummery, L.M. Evans, Effect of rhenium irradiations on the mechanical properties of tungsten for nuclear fusion applications, J. Nucl. Mater. 477 (2016) 42–49.
[27] M. Rieth, S.L. Dudarev, S.M.G. De Vicente, J. Aktaa, T. Ahlgren, S. Antusch, D.E.J. Armstrong, M. Balden, N. Baluc, M.-F. Barthe, Recent progress in research on tungsten materials for nuclear fusion applications in Europe, J. Nucl. Mater. 432 (2013) 482–500.
[28] G. Marinelli, F. Martina, H. Lewtas, D. Hancock, S. Mehraban, N. Lavery, S. Ganguly, S. Williams, Microstructure and thermal properties of unalloyed tungsten deposited by Wire+ Arc Additive Manufacture, J. Nucl. Mater. 522 (2019) 45–53.
[29] R. Liu, Z. Wang, T. Sparks, F. Liou, J. Newkirk, Aerospace applications of laser additive manufacturing, in: Laser Addit. Manuf., Elsevier, 2017: pp. 351–371.
[30] H. Wang, L. Wang, Perfect selective metamaterial solar absorbers, Opt. Express. 21 (2013) A1078–A1093.
[31] J. Song, M. Si, Q. Cheng, Z. Luo, Two-dimensional trilayer grating with a metal/insulator/metal structure as a thermophotovoltaic emitter, Appl. Opt. 55 (2016) 1284–1290.
[32] H. Zhang, M. Luo, Y. Zhou, Y. Ji, L. Chen, Ultra-broadband, polarization-independent, wide-angle near-perfect absorber incorporating a one-dimensional meta-surface with refractory materials from UV to the near-infrared region, Opt. Mater. Express. 10 (2020) 484–491.
[33] A.D. Rakić, A.B. Djurišić, J.M. Elazar, M.L. Majewski, Optical properties of metallic films for vertical-cavity optoelectronic devices, Appl. Opt. 37 (1998) 5271–5283.
[34] E. Rephaeli, S. Fan, Tungsten black absorber for solar light with wide angular operation range, Appl. Phys. Lett. 92 (2008) 211107.
[35] M.A. Keçebaş, K. Şendur, Enhancing the spectral reflectance of refractory metals by multilayer optical thin-film coatings, JOSA B. 35 (2018) 1845–1853.
[36] C. Hu, J. Liu, J. Wang, Z. Gu, C. Li, Q. Li, Y. Li, S. Zhang, C. Bi, X. Fan, New design for highly durable infrared-reflective coatings, Light Sci. Appl. 7 (2018) 17175.
[37] H.-J. Jeong, Y.-C. Kim, S.K. Lee, J.-H. Yun, J.-H. Jang, Enhanced spectral response of CIGS solar cells with anti-reflective subwavelength structures and quantum dots, Sol. Energy Mater. Sol. Cells. 194 (2019) 177–183.
[38] A. Benamira, S. Pattanaik, Application of the Transfer Matrix Method to Anti-reflective Coating Rendering, in: Comput. Graph. Int. Conf., Springer, 2020: pp. 83–95.
[39] D.S. Hobbs, Random texture anti-reflection optical surface treatment, (2012).
[40] C. Cho, H. Kim, S. Jeong, S.-W. Baek, J.-W. Seo, D. Han, K. Kim, Y. Park, S. Yoo, J.-Y. Lee, Random and V-groove texturing for efficient light trapping in organic photovoltaic cells, Sol. Energy Mater. Sol. Cells. 115 (2013) 36–41.
[41] A. Goulas, S. Zhang, J.R. McGhee, D.A. Cadman, W.G. Whittow, J.C. Vardaxoglou, D.S. Engstrøm, Fused filament fabrication of functionally graded polymer composites with variable relative permittivity for microwave devices, Mater. Des. (2020) 108871.
[42] Y.-B. Chen, Z.M. Zhang, Design of tungsten complex gratings for thermophotovoltaic radiators, Opt. Commun. 269 (2007) 411–417.
[43] H. Savin, P. Repo, G. Von Gastrow, P. Ortega, E. Calle, M. Garín, R. Alcubilla, Black silicon solar cells with interdigitated back-contacts achieve 22.1% efficiency, Nat. Nanotechnol. 10 (2015) 624–628.
[44] H. Raether, Surface plasmons on smooth surfaces, in: Surf. Plasmons Smooth Rough Surfaces Gratings, Springer, 1988: pp. 4–39.
[45] A. Hoffmann, Z. Lenkefi, Z. Szentirmay, Effect of roughness on surface plasmon scattering in gold films, J. Phys. Condens. Matter. 10 (1998) 5503.
[46] G.A. Farias, A.A. Maradudin, Surface plasmons on a randomly rough surface, Phys. Rev. B. 28 (1983) 5675.

[47] S. Ma, S. Liu, Q. Xu, J. Xu, R. Lu, Y. Liu, Z. Zhong, A theoretical study on the optical properties of black silicon, AIP Adv. 8 (2018) 35010.
[48] K. Gorgulu, A. Gok, M. Yilmaz, K. Topalli, N. Bıyıklı, A.K. Okyay, All-silicon ultra-broadband infrared light absorbers, Sci. Rep. 6 (2016) 1–7.
[49] Y.-B. Chen, Z.M. Zhang, Heavily doped silicon complex gratings as wavelength-selective absorbing surfaces, J. Phys. D. Appl. Phys. 41 (2008) 95406.
[50] A.G. Voronovich, Wave scattering from rough surfaces, Springer Science & Business Media, 2013.
[51] K.E. Torrance, E.M. Sparrow, Theory for off-specular reflection from roughened surfaces, Josa. 57 (1967) 1105–1114.
[52] G. Videen, J.-Y. Hsu, W.S. Bickel, W.L. Wolfe, Polarized light scattered from rough surfaces, JOSA A. 9 (1992) 1111–1118.
[53] S.K. Sinha, E.B. Sirota, and S. Garoff, H.B. Stanley, X-ray and neutron scattering from rough surfaces, Phys. Rev. B. 38 (1988) 2297.
[54] L. Zheng, Y. Ma, S. Chu, S. Wang, B. Qu, L. Xiao, Z. Chen, Q. Gong, Z. Wu, X. Hou, Improved light absorption and charge transport for perovskite solar cells with rough interfaces by sequential deposition, Nanoscale. 6 (2014) 8171–8176.
[55] S. Faÿ, L. Feitknecht, R. Schlüchter, U. Kroll, E. Vallat-Sauvain, A. Shah, Rough ZnO layers by LP-CVD process and their effect in improving performances of amorphous and microcrystalline silicon solar cells, Sol. Energy Mater. Sol. Cells. 90 (2006) 2960–2967.
[56] H. Raether, Surface plasmons on gratings, in: Surf. Plasmons Smooth Rough Surfaces Gratings, Springer, 1988: pp. 91–116.
[57] M. Kanso, S. Cuenot, G. Louarn, Roughness effect on the SPR measurements for an optical fibre configuration: Experimental and numerical approaches, J. Opt. A Pure Appl. Opt. 9 (2007) 586.
[58] I. Simonsen, A.A. Maradudin, Numerical simulation of electromagnetic wave scattering from planar dielectric films deposited on rough perfectly conducting substrates, Opt. Commun. 162 (1999) 99–111.
[59] L. Cao, K. Sendur, Surface Roughness Effects on the Broadband Reflection for Refractory Metals and Polar Dielectrics, Materials (Basel). 12 (2019) 3090.
[60] J.T. Johnson, M. Zhang, Theoretical study of the small slope approximation for ocean polarimetric thermal emission, IEEE Trans. Geosci. Remote Sens. 37 (1999) 2305–2316.
[61] C. Wu, C.H. Crouch, L. Zhao, J.E. Carey, R. Younkin, J.A. Levinson, E. Mazur, R.M. Farrell, P. Gothoskar, A. Karger, Near-unity below-band-gap absorption by microstructured silicon, Appl. Phys. Lett. 78 (2001) 1850–1852.
[62] H. Jansen, M. de Boer, J. Burger, R. Legtenberg, M. Elwenspoek, The black silicon method II: The effect of mask material and loading on the reactive ion etching of deep silicon trenches, Microelectron. Eng. 27 (1995) 475–480.
[63] T. Gimpel, I. Höger, F. Falk, W. Schade, S. Kontermann, Electron backscatter diffraction on femtosecond laser sulfur hyperdoped silicon, Appl. Phys. Lett. 101 (2012) 111911.
[64] B. Franta, E. Mazur, S.K. Sundaram, Ultrafast laser processing of silicon for photovoltaics, Int. Mater. Rev. 63 (2018) 227–240.
[65] M.A. Kecebas, N. Pirouzfam, K. Sendur, Origins of the enhanced broadband absorption in black silicon, J. Appl. Phys. 129 (2021) 163103.
[66] P. Bouchon, C. Koechlin, F. Pardo, R. Haïdar, J.-L. Pelouard, Wideband omnidirectional infrared absorber with a patchwork of plasmonic nanoantennas, Opt. Lett. 37 (2012) 1038–1040.
[67] Y. Cui, K.H. Fung, J. Xu, H. Ma, Y. Jin, S. He, N.X. Fang, Ultrabroadband light absorption by a sawtooth anisotropic metamaterial slab, Nano Lett. 12 (2012) 1443–1447.
[68] Y. Tian, A. Ghanekar, M. Ricci, M. Hyde, O. Gregory, Y. Zheng, A review of tunable wavelength selectivity of metamaterials in near-field and far-field radiative thermal transport, Materials (Basel). 11 (2018) 862.
[69] Z. Wu, W. Xue, Y. Liu, D. Wei, J. Wang, L. Yin, Y. Wang, X. Liu, Q. Zhang, F. Cao, Toward versatile applications via tuning transition wavelength of the WTa-SiO2 based spectrally selective absorber, Sol. Energy. 202 (2020) 115–122.
[70] S.D. Calisgan, V. Villanueva-Lopez, V. Rajaram, Z. Qian, S. Kang, S.P. Hernandez-Rivera, M. Rinaldi, Spectroscopic chemical sensing based on narrowband MEMS resonant infrared detectors, in: 2018 IEEE SENSORS, IEEE, 2018: pp. 1–4.
[71] B. Zhao, M. Hu, X. Ao, Q. Xuan, G. Pei, Spectrally selective approaches for passive cooling of solar cells: A review, Appl. Energy. 262 (2020) 114548.
[72] F.K. Khosroshahi, H. Ertürk, M.P. Mengüç, Optimization of spectrally selective Si/SiO2 based filters for

thermophotovoltaic devices, J. Quant. Spectrosc. Radiat. Transf. 197 (2017) 123–131.
[73] A. Dan, J. Jyothi, K. Chattopadhyay, H.C. Barshilia, B. Basu, Spectrally selective absorber coating of WAlN/WAlON/Al2O3 for solar thermal applications, Sol. Energy Mater. Sol. Cells. 157 (2016) 716–726.
[74] S. Chattopadhyay, Y.F. Huang, Y.J. Jen, a. Ganguly, KH Chen and LC Chen, Mater. Sci. Eng., R. 69 (2010) 1–35.
[75] H. Tan, R. Santbergen, A.H.M. Smets, M. Zeman, Plasmonic light trapping in thin-film silicon solar cells with improved self-assembled silver nanoparticles, Nano Lett. 12 (2012) 4070–4076.
[76] S. Niu, B. Li, Z. Mu, M. Yang, J. Zhang, Z. Han, L. Ren, Excellent structure-based multifunction of morpho butterfly wings: A review, J. Bionic Eng. 12 (2015) 170–189.
[77] Y. Zhu, W. Zhang, D. Zhang, Fabrication of sensor materials inspired by butterfly wings, Adv. Mater. Technol. 2 (2017) 1600209.
[78] Q. Li, Q. Zeng, L. Shi, X. Zhang, K.-Q. Zhang, Bio-inspired sensors based on photonic structures of Morpho butterfly wings: a review, J. Mater. Chem. C. 4 (2016) 1752–1763.
[79] R. Ahmed, X. Ji, R.M.H. Atta, A.A. Rifat, H. Butt, Morpho butterfly-inspired optical diffraction, diffusion, and bio-chemical sensing, RSC Adv. 8 (2018) 27111–27118.
[80] X. Yang, Z. Peng, H. Zuo, T. Shi, G. Liao, Using hierarchy architecture of Morpho butterfly scales for chemical sensing: Experiment and modeling, Sensors Actuators A Phys. 167 (2011) 367–373.
[81] J. He, N.S. Villa, Z. Luo, S. An, Q. Shen, P. Tao, C. Song, J. Wu, T. Deng, W. Shang, Integrating plasmonic nanostructures with natural photonic architectures in Pd-modified Morpho butterfly wings for sensitive hydrogen gas sensing, RSC Adv. 8 (2018) 32395–32400.
[82] Y. Zhu, J. Hao, W. Li, J. Yang, E. Dong, A new robotic tactile sensor with bio-mimetic structural colour inspired by Morpho butterflies, Bioinspir. Biomim. 14 (2019) 56010.
[83] L. Zhou, J. He, W. Li, P. He, Q. Ye, B. Fu, P. Tao, C. Song, J. Wu, T. Deng, Butterfly wing hears sound: acoustic detection using biophotonic nanostructure, Nano Lett. 19 (2019) 2627–2633.
[84] S. Han, Y. Xu, J. Sun, Y. Liu, Y. Zhao, W. Tao, R. Chai, Isolation and analysis of extracellular vesicles in a Morpho butterfly wing-integrated microvortex biochip, Biosens. Bioelectron. 154 (2020) 112073.
[85] Z. He, A. Elbaz, B. Gao, J. Zhang, E. Su, Z. Gu, Disposable Morpho menelaus based flexible microfluidic and electronic sensor for the diagnosis of neurodegenerative disease, Adv. Healthc. Mater. 7 (2018) 1701306.
[86] H. Yabu, Y. Matsuo, T. Yamada, H. Maeda, J. Matsui, Highly porous magnesium silicide honeycombs prepared by magnesium vapor annealing of silica-coated polymer honeycomb films toward ultralightweight thermoelectric materials, Chem. Mater. 32 (2020) 10176–10183.
[87] A. Krishna, J. Lee, Morpho butterfly-inspired spectral emissivity of metallic microstructures for radiative cooling, in: 2018 17th IEEE Intersoc. Conf. Therm. Thermomechanical Phenom. Electron. Syst., IEEE, 2018: pp. 78–85.
[88] Q. Shen, S. Ma, Z. Luo, S. An, J. He, R. Zhang, P. Tao, C. Song, J. Wu, R.A. Potyrailo, Butterfly wing inspired high performance infrared detection with spectral selectivity, Adv. Opt. Mater. 8 (2020) 1901647.
[89] G. Liao, H. Zuo, Y. Cao, T. Shi, Optical properties of the micro/nano structures of Morpho butterfly wing scales, Sci. China Ser. E Technol. Sci. 53 (2010) 175–181.
[90] T. Chen, T. Lu, Z. Chen, W. Wang, W. Zhang, H. Pan, X. Meng, X. Jiang, S. Zhu, Microstructures of responsive photonic crystals on the stimuli-responsive performance: Effects and simulation, Sensors Actuators B Chem. 305 (2020) 127421.
[91] W. Wu, G. Liao, T. Shi, R. Malik, C. Zeng, The relationship of selective surrounding response and the nanophotonic structures of Morpho butterfly scales, Microelectron. Eng. 95 (2012) 42–48.
[92] K. Chung, S. Yu, C. Heo, J.W. Shim, S. Yang, M.G. Han, H. Lee, Y. Jin, S.Y. Lee, N. Park, Flexible, angle-independent, structural color reflectors inspired by Morpho butterfly wings, Adv. Mater. 24 (2012) 2375–2379.
[93] A. Krishna, X. Nie, A.D. Warren, J.E. Llorente-Bousquets, A.D. Briscoe, J. Lee, Infrared optical and thermal properties of microstructures in butterfly wings, Proc. Natl. Acad. Sci. 117 (2020) 1566–1572.
[94] W. Paszkowicz, Genetic algorithms, a nature-inspired tool: survey of applications in materials science and related fields, Mater. Manuf. Process. 24 (2009) 174–197.
[95] A. V Tikhonravov, M.K. Trubetskov, Development of the needle optimization technique and new features of OptiLayer design software, in: Opt. Interf. Coatings, International Society for Optics and Photonics, 1994: pp. 10–20.
[96] S. So, T. Badloe, J. Noh, J. Bravo-Abad, J. Rho, Deep learning enabled inverse design in nanophotonics, Nanophotonics. 9 (2020) 1041–1057.
[97] A. Jiang, Y. Osamu, L. Chen, Multilayer optical thin film design with deep Q learning, Sci. Rep. 10 (2020)

1–7.
[98] A.B. Koucheh, M.A. Kecebas, K. Sendur, Impedance mismatch-based enhancement of broadband reflectance of tungsten with bio-inspired multilayers, J. Quant. Spectrosc. Radiat. Transf. 276 (2021) 107899.
[99] C.A. Tippets, Y. Fu, A.-M. Jackson, E.U. Donev, R. Lopez, Reproduction and optical analysis of Morpho-inspired polymeric nanostructures, J. Opt. 18 (2016) 65105.
[100] T.D.B. Jacobs, T. Junge, L. Pastewka, Quantitative characterization of surface topography using spectral analysis, Surf. Topogr. Metrol. Prop. 5 (2017) 13001.
[101] J. Zhou, A.F. Kaplan, L. Chen, L.J. Guo, Experiment and theory of the broadband absorption by a tapered hyperbolic metamaterial array, ACS Photonics. 1 (2014) 618–624.
[102] J. Boroumand, S. Das, A. Vázquez-Guardado, D. Franklin, D. Chanda, Unified electromagnetic-electronic design of light trapping silicon solar cells, Sci. Rep. 6 (2016) 1–10.
[103] Z.-H. Chen, N. Qiao, Y. Yang, H. Ye, S. Liu, W. Wang, Y. Wang, Enhanced broadband electromagnetic absorption in silicon film with photonic crystal surface and random gold grooves reflector, Sci. Rep. 5 (2015) 1–8.
[104] K. Gorgulu, M. Yilmaz, K. Topalli, A.K. Okyay, Wideband 'black silicon'for mid-infrared applications, J. Opt. 19 (2017) 65101.
[105] F. Lumerical, Solutions, (2016).
[106] L. Tsang, K.-H. Ding, X. Li, P.N. Duvelle, J.H. Vella, J. Goldsmith, C.L.H. Devlin, N.I. Limberopoulos, Studies of the influence of deep subwavelength surface roughness on fields of plasmonic thin film based on Lippmann–Schwinger equation in the spectral domain, JOSA B. 32 (2015) 878–891.
[107] M.N.O. Sadiku, Numerical techniques in electromagnetics, CRC press, 2000.
[108] D. Canteli, J.M. López, S. Lauzurica, M. Lluscà, M.I. Sánchez-Aniorte, J. Bertomeu, M. Morales, C. Molpeceres, Analysis by finite element calculations of light scattering in laser-textured AZO films for PV thin-film solar cells, Energy Procedia. 84 (2015) 78–85.
[109] H. Wang, J.Q. Bagley, L. Tsang, S. Huang, K.-H. Ding, A. Ishimaru, Image enhancement for flat and rough film plasmon superlenses by adding loss, JOSA B. 28 (2011) 2499–2509.
[110] Y. Delacrétaz, O. Seydoux, S. Chamot, A. Ettemeyer, C. Depeursinge, Monte Carlo simulation of the field back-scattered from rough surfaces, JOSA A. 29 (2012) 270–277.
[111] T. Wang, L. Tsang, J. Johnson, S. Tan, Scattering and transmission of waves in multiple random rough surfaces: Energy conservation studies with the second order small perturbation method, Prog. Electromagn. Res. 157 (2016) 1–20.
[112] S.H. Yueh, R. Kwok, F.K. Li, S. V Nghiem, W.J. Wilson, J.A. Kong, Polarimetric passive remote sensing of ocean wind vectors, Radio Sci. 29 (1994) 799–814.
[113] L. Novotny, Effective wavelength scaling for optical antennas, Phys. Rev. Lett. 98 (2007) 266802.
[114] C. Niu, T. Zhu, Y. Lv, Influence of Surface Morphology on Absorptivity of Light-Absorbing Materials, Int. J. Photoenergy. 2019 (2019).
[115] H. Sai, Y. Kanamori, Spectrally selective thermal radiators and absorbers with periodic microstructured surface for high-temperature applications, Microscale Thermophys. Eng. 7 (2003) 101–115.
[116] E.D. Palik, Handbook of optical constants of solids, Academic press, 1998.
[117] B. Liu, X. Xia, C. Sun, Scattering properties of solid rough surface of nickel skeleton, Infrared Phys. Technol. 93 (2018) 25–33.
[118] Z. Liu, G. Liu, Z. Huang, X. Liu, G. Fu, Ultra-broadband perfect solar absorber by an ultra-thin refractory titanium nitride meta-surface, Sol. Energy Mater. Sol. Cells. 179 (2018) 346–352.
[119] M. Shimizu, H. Yugami, Thermal radiation control by surface gratings as an advanced cooling system for electronic devices, J. Therm. Sci. Technol. 6 (2011) 297–306.
[120] H. Sai, H. Yugami, Y. Kanamori, K. Hane, Solar selective absorbers based on two-dimensional W surface gratings with submicron periods for high-temperature photothermal conversion, Sol. Energy Mater. Sol. Cells. 79 (2003) 35–49.
[121] I.S. Amiri, V.J. Sorger, P. Yupapin, Zinc Oxide nanowire gratings for light absorption control through polarization manipulation, Phys. E Low-Dimensional Syst. Nanostructures. 108 (2019) 68–73.
[122] C.L. Briant, Refractory metals and alloys, Encycl. Mater. Sci. Technol. (2011) 8088–8095.
[123] K. Yu, T. Fan, S. Lou, D. Zhang, Biomimetic optical materials: Integration of nature's design for manipulation of light, Prog. Mater. Sci. 58 (2013) 825–873.
[124] D.R. Smith, D.C. Vier, T. Koschny, C.M. Soukoulis, Electromagnetic parameter retrieval from inhomogeneous metamaterials, Phys. Rev. E. 71 (2005) 36617.
[125] B. Razavi, Architectures and circuits for RF CMOS receivers, in: Proc. IEEE 1998 Cust. Integr. Circuits Conf.

(Cat. No. 98CH36143), IEEE, 1998: pp. 393–400.
[126] S. Zhang, Y. Chen, Nanofabrication and coloration study of artificial Morpho butterfly wings with aligned lamellae layers, Sci. Rep. 5 (2015) 1–10.
[127] J.D. Caldwell, L. Lindsay, V. Giannini, I. Vurgaftman, T.L. Reinecke, S.A. Maier, O.J. Glembocki, Low-loss, infrared and terahertz nanophotonics using surface phonon polaritons, Nanophotonics. 4 (2015) 44–68.
[128] S.W. Pang, D.D. Rathman, D.J. Silversmith, R.W. Mountain, P.D. DeGraff, Damage induced in Si by ion milling or reactive ion etching, J. Appl. Phys. 54 (1983) 3272–3277.
[129] T.H. Fung, T. Veeken, D. Payne, B. Veettil, A. Polman, M. Abbott, Application and validity of the effective medium approximation to the optical properties of nano-textured silicon coated with a dielectric layer, Opt. Express. 27 (2019) 38645–38660.
[130] F. Marquier, K. Joulain, J.-P. Mulet, R. Carminati, J.-J. Greffet, Engineering infrared emission properties of silicon in the near field and the far field, Opt. Commun. 237 (2004) 379–388.
[131] A.A. Elsayed, Y.M. Sabry, D. Khalil, F. Marty, T. Bourouina, Optical diffuse reflectance of black silicon and its isotropicity, in: 2016 URSI Asia-Pacific Radio Sci. Conf. (URSI AP-RASC), IEEE, 2016: pp. 1944–1946.
[132] A. Raza, A.S. Alketbi, R. Devarapalli, H. Li, T. Zhang, Refractory Ultrathin Nanocomposite Solar Absorber with Superior Spectral Selectivity and Thermal Stability, Adv. Opt. Mater. 8 (2020) 2000679.
[133] M.A. Keçebaş, K. Şendur, Enhancing the spectral reflectance of refractory metals by multilayer optical thin-film coatings, JOSA B. 35 (2018) 1845–1853.

6. List of Symbols, Abbreviations and Acronyms

l: is transverse correlation length

K: Wave vector

cl_x: Correlation length in x direction

cl_y: Correlation length in y direction

h: Standard deviation

Γ: Gamma function

R: Fresnel reflection coefficient

g: Weighting function

ε: Permittivity

μ: Permeability

e: Electron mass

f: Frequency

A: Absorption

E: Electric field

H: Magnetic field

δ: Optical thickness

Z: Intrinsic impedance

Ƶ: Surface impedance

N: Layer number

j: √-1

Z_0: Intrinsic impedance of free space

$Ƶ_1$: Surface impedance of the top layer

Γ: Reflection coefficient

Γ_{Norm}: Normalized reflection coefficient with respect to Z_0

r: Amplitude of the reflection coefficient

θ: Phase of the reflection coefficient

n: Refractive index

k: Extinction coefficient

t: Geometrical thickness

υ_r: Angle of refraction

λ: Free space wavelength

α: Weighting factor

p: Periodicity

I_{BB}: Blackbody radiation intensity

T: Temperature

h: Planck's constant

k_b: Boltzmann's constant

c: Speed of light

Re: Real part of a complex number

Im: Imaginary part of a complex number

7. Publications from this Project

- Cao, Lina, and Kursat Sendur. "Surface roughness effects on the broadband reflection for refractory metals and polar dielectrics." *Materials* 12.19 (2019): 3090.

- Kecebas, Muhammed Ali, Niloufar Pirouzfam, and Kursat Sendur. "Origins of the enhanced broadband absorption in black silicon." *Journal of Applied Physics* 129.16 (2021): 163103.

- Pirouzfam, Niloufar, and Kursat Sendur. "Tungsten based spectrally selective absorbers with anisotropic rough surface texture." *Nanomaterials* 11.8 (2021): 2018.

- Koucheh, Amin Balazadeh, Muhammed Ali Kecebas, and Kursat Sendur. "Impedance mismatch-based enhancement of broadband reflectance of tungsten with bio-inspired multilayers." *Journal of Quantitative Spectroscopy and Radiative Transfer* 276 (2021): 107899.

- N. Pirouzfam, M.P. Menguc, & K. Sendur, "Colorization of passive radiative cooling coatings using plasmonic effects". Solar Energy Materials and Solar Cells, 253, 112225 (2023).

8. Invited Talks

- Prof. Kürşat Şendur visited AFRL Dayton and presented “Broadband Plasmonic Surfaces and Cool Plasmonic Transducers”.
- Prof. Kürşat Şendur visited NASA Langley Research Center and presented “Tailoring the Spectral Reflectivity and Emissivity via Thin-Film Coatings and Nanostructured Surfaces”.
- Prof. Kürşat Şendur visited NASA Langley Research Center and presented “Suppressing Infrared Radiation through Fibrous Thermal Insulation Materials and Thin-Film Coatings”

9. AFOSR Program Review Attendance and Presentation

- 2016 Aerospace Materials for Extreme Environments Program Review at the Basic Research Innovation and Collaboration Center (BRICC) at Arlington, Virginia.
- 2017 Aerospace Materials for Extreme Environments Program Review at the Kirtland's Air Force Base at Albuquerque, New Mexico.
- 2018 Aerospace Materials for Extreme Environments Program Review at the Doolittle Institute, Niceville, Florida.
- 2019 Aerospace Materials for Extreme Environments Program Review at the Alexandria, Virginia.
- 2020 Aerospace Materials for Extreme Environments Program Review: Virtual Meeting.
- 2021 Aerospace Materials for Extreme Environments Program Review: Virtual Meeting.
- 2022 Aerospace Materials for Extreme Environments Program Review: Virtual Meeting.